

GGR Cutting-Edge Review

Atom Probe Tomography: Development and Application to the Geosciences

Steven M. Reddy ^{(1, 2)*} , David W. Saxe ⁽¹⁾ , William D. A. Rickard ⁽¹⁾ ,
 Denis Fougerousse ^(1, 2) , Stephanie D. Montalvo ^(1, 2) , Rick Verberne ^(1, 2)  and
 Arie van Riessen ⁽¹⁾ 

(1) Geoscience Atom Probe, Advanced Resource Characterisation Facility, John de Laeter Centre, Curtin University, GPO Box U1987, Perth, 6845, Australia

(2) School of Earth and Planetary Sciences, Curtin University, GPO Box U1987, Perth, 6845, Australia

* Corresponding author. e-mail: s.reddy@curtin.edu.au

Atom probe tomography (APT) is an analytical technique that provides quantitative three-dimensional elemental and isotopic analyses at sub-nanometre resolution across the whole periodic table. Although developed and mostly used in the materials science and semiconductor fields, recent years have seen increasing development and application in the geoscience and planetary science disciplines. Atom probe studies demonstrate compositional complexity at the nanoscale and provide fundamental new insights into the atom-scale mechanisms taking place in minerals over geological time. Here, we provide an overview of APT, including the historical development and technical aspects of the instrumentation, and the fundamentals of data acquisition, data processing and data reconstruction. We also review previous studies and highlight the potential future applications of nanoscale geochemical studies of natural materials.

Keywords: atom probe, microscopy, mineral, geochemistry, isotope geochemistry, nanoscale.

Received 20 Sep 19 – Accepted 23 Dec 19

One of the major trends in geochemical and geochronological research over the last few decades is the development and application of analytical instruments capable of quantifying the elemental and isotopic compositions of smaller and smaller volumes of material. This development is driven in the geosciences by the realisation that higher spatial resolution provides increased ability to characterise distinct elemental and isotopic reservoirs, which record the wide range of complex processes occurring during the growth and subsequent modification of geological materials. High-spatial-resolution data provide important complementary information to assist in the interpretation of lower spatial resolution, but higher precision, data sets. Hence, multi-scale and correlative analytical approaches to geological characterisation are becoming a routine workflow to understand a range of geological processes.

The pinnacle of high-spatial-resolution compositional analysis is the ability to analyse elemental and isotopic compositions in minerals at a sub-nanometre scale. All

geological processes are fundamentally controlled by element interactions at this scale, so the ability to quantify elemental and isotopic compositions with nanometre resolution has the potential to greatly increase our understanding of fundamental geological processes. However, few analytical techniques are capable of providing such resolution (Figure 1). One such technique is atom probe tomography (APT), a time-of-flight mass spectrometry system that characterises atomic species and position with sub-nanometre spatial resolution. A significant advantage of APT lies in the capability to provide quantitative, 3D compositional and spatial imaging across the whole periodic table of elements, without the need to specify which isotopic peaks will be measured prior to the analysis.

The technique that is now known as APT has been in development for more than five decades (Müller *et al.* 1968). Initially, APT analysis was restricted to conductive materials, but more recent hardware advances have relaxed this constraint. These hardware developments have enabled the application of APT to semiconductors (e.g., Larson *et al.*

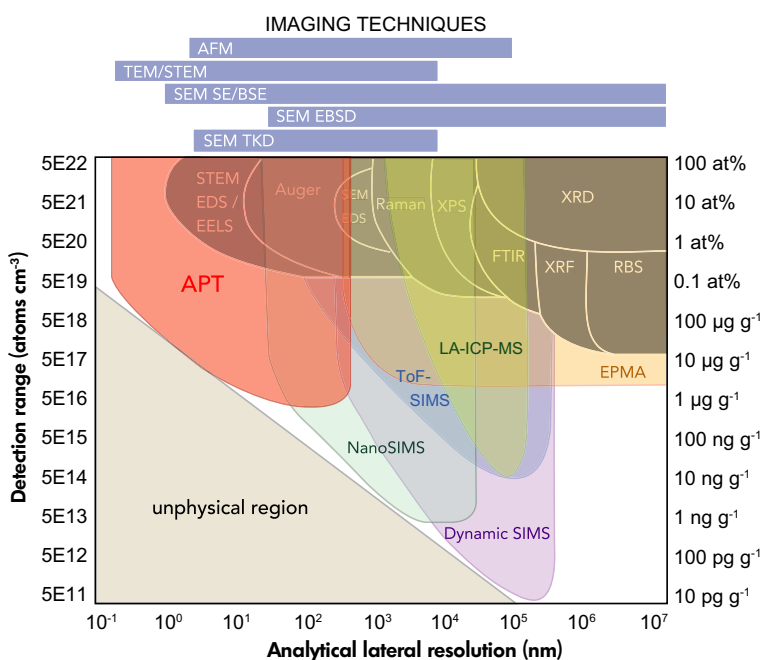


Figure 1. Analytical sensitivity versus analytical volume for APT compared with other commonly used geoscience characterisation techniques. Figure modified from an original version by Cameca.

2016) and, in the last few years, the analysis of minerals (Figure 2). The literature on atom probe studies of minerals has highlighted some of the potential applications of nanoscale geochemistry and geochronology to better understand significant geological problems. However, the development and application of APT in the geosciences is in its early stages. In this review, we provide a comprehensive introduction to APT for the geoscientist, building on a recent Viewpoint article (Saxey *et al.* 2018a). We first give an overview of atom probe fundamentals, and outline the historical development of the technique. We will then cover the basics of atom probe specimen preparation and discuss the correlative microscopy techniques that are essential to selecting and characterising the APT region of interest and interpreting atom probe data. We will review the published APT research on minerals before outlining in potential future applications in the geosciences. Finally, we will look at some of the issues that hinder APT and outline how these may be alleviated through future development of the instrumentation.

An introduction to atom probe tomography

Atom probe tomography is an analytical technique capable of three-dimensional nanoscale chemical mapping of individual atoms. Analysis of a sample by APT is a destructive process that produces a unique data set type, combining time-of-flight mass spectrometry with nanoscale

3D spatial coordinates for several million individual atoms to produce a large atomic point cloud (Figure 3). APT data sets may contain a rich complexity of chemical and isotopic information that very often cannot be obtained by other characterisation techniques.

Originally developed as an atomic-scale point-sampling method (Müller *et al.* 1968), over several decades the technology and methodology surrounding this field has gradually improved and matured to a more versatile analytical approach that can be applied to a range of materials across various research disciplines and industrial applications (Kelly and Panitz 2017). APT is used within materials science and semiconductor manufacturing to visualise and quantify chemical variations at sub-micrometre scales (Figure 4). Common features of interest include chemical segregation at defects such as dislocations and grain boundaries, subtle co-clustering behaviour observed between two or more trace elements, and nanoscale exsolution or heterogeneous inclusions.

The history of APT has its beginning in the early work of Müller (1936, 1951). In 1955, Müller used his field ion microscope (FIM), a predecessor to the atom probe microscope, to image individual atoms for the very first time. The FIM technique uses an ‘imaging gas’ as a medium to generate atomic-scale views of a specimen surface, with the gas atoms ionised and accelerated towards a phosphor screen by a locally enhanced electric field (Panitz 1982;

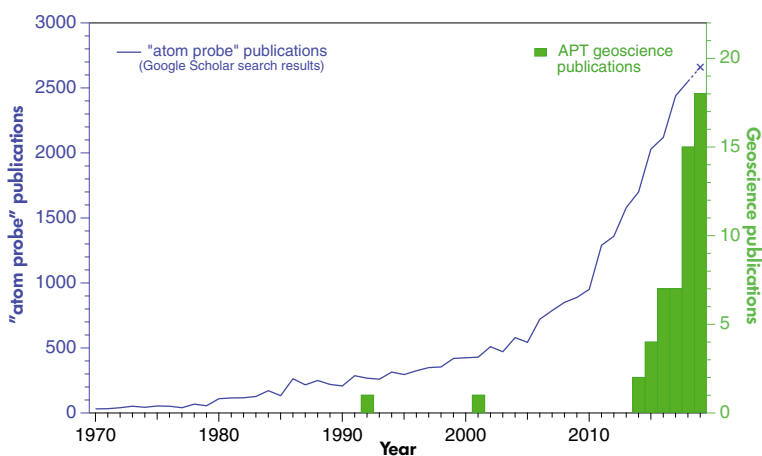


Figure 2. Growth of APT publications in the scientific literature (1970–2019). The line shows number of publications based on a Google Scholar search of the term ‘atom probe’ for each year since 1970. The histogram shows the recent growth of atom probe studies in the geosciences. For a list of geoscience articles published to December 2019, refer to Appendix S1.

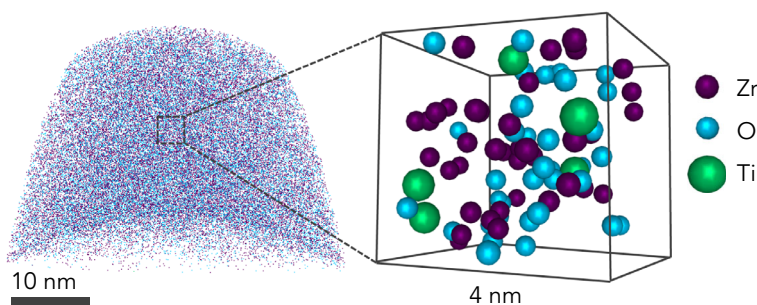


Figure 3. An example of an APT data set obtained from a sample of baddeleyite (ZrO_2). Each dot represents the position of different atomic species (Zr in purple, O in aqua and Ti in green). Expanded cube shows the position of atoms within a $4 \times 4 \times 4$ nm volume.

Figure 5). Further development led to the addition of a time-of-flight mass spectrometer to measure the mass of atoms that were removed from the sample itself by pulsing the electric field. The new instrument was described as an ‘atom probe field ion microscope’ (APFIM) in analogy with the electron microprobe, which came into use in the 1950s (Castaing 1960). The development of APFIM was a critical step towards the broad application of this technique for chemical analysis in material science and, eventually, the geosciences.

The APFIM provided essentially a one-dimensional series of atomic species as the sample was ‘eroded’ one atomic layer at a time. Continued improvements and new configurations of the hardware through to the mid-1990s resulted in position-sensitive ion detection, in combination with full-spectrum time-of-flight mass spectrometry (Cerezo *et al.* 1988, Bas *et al.* 1995, Miller *et al.* 1996). This produced the three-

dimensional atom probe (3DAP; Figure 5), recognisably similar to the systems used in modern atom probe facilities.

The latest important advances have come with the introduction of the local electrode atom probe (LEAP) in the early 2000s (Kelly *et al.* 2004, Larson *et al.* 2013b), which simultaneously increased the speed of acquisition, and the three-dimensional field-of-view, by several orders of magnitude. It also allowed ‘micro-tip’ specimens to be analysed, providing greater flexibility in the preparation of samples. Finally, since the late 2000s, the commercial availability of practical, laser-assisted atom probes, in which removal of atoms from the sample is aided by a fast laser pulse, has allowed the technique to be applied to non-conducting samples (Larson *et al.* 2008, Chen *et al.* 2009, Marquis *et al.* 2010, Chen *et al.* 2011). This has enabled the atom probe analysis of semiconductors and is a critical advance in

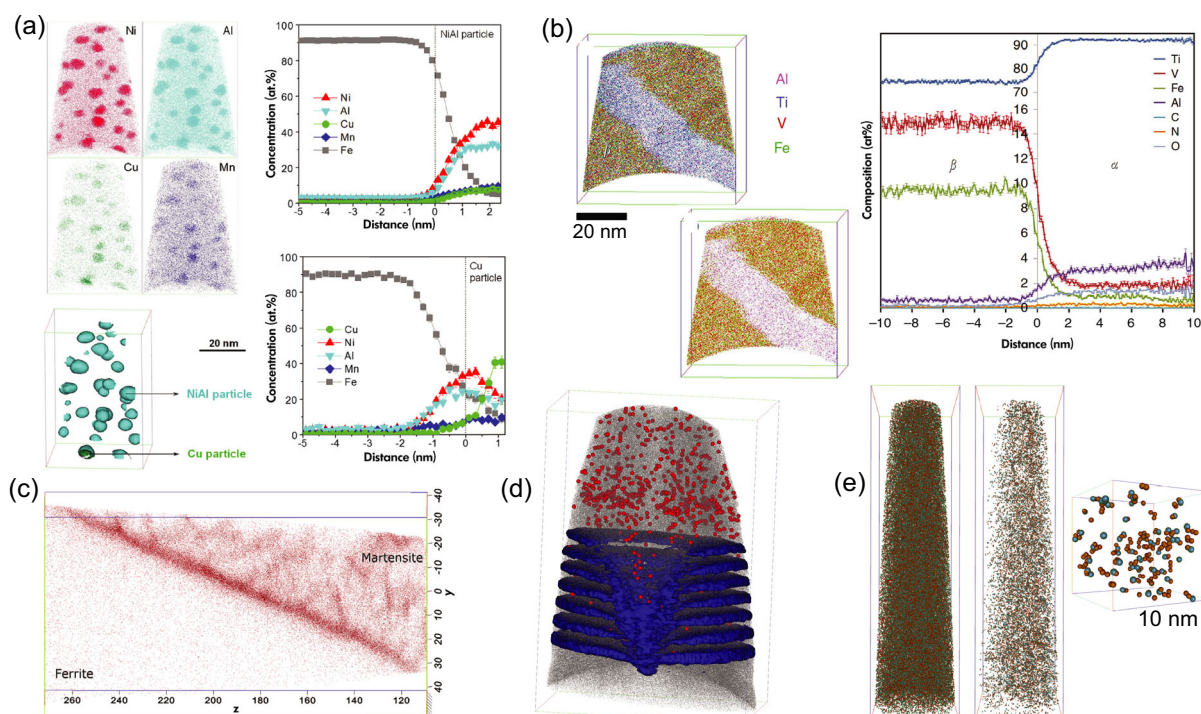


Figure 4. Material science examples of APT applications. (a) Coarsening of NiAl and Cu-rich particles within a steel weld (figure 11 of Jiao et al. 2016); (b) element partitioning between alpha and beta phases following heat treatment of a high-strength titanium alloy (Devaraj et al. 2016); (c) partitioning of carbon (red dots) between ferrite and martensite phases in a decarburised alloy (figure 3 of Van Landeghem et al. 2017); (d) V-pit defect distorting InGaN/GaN quantum well layers (grey dots are Ga atoms and In isoconcentration surfaces are in blue) showing Mg dopant (red spheres) distribution (figure courtesy of Rob Ulfig, Cameca); (e) fine-scale clustering in an Al-Cu-Mg alloy. Full data set (left), Al and Cu atoms forming clusters (middle), $10 \times 10 \times 10$ nm volume containing a single Cu-Mg cluster (right) (figure 7 of Marceau et al. 2010). (a) Reprinted from *Acta Materialia*, volume 120, 216–227, Jiao et al., Effects of welding and post-weld heat treatments on nanoscale precipitation and mechanical properties of an ultra-high strength steel hardened by NiAl and Cu nanoparticles © 2016, with permission from Elsevier. (c) Reprinted from *Acta Materialia*, volume 124, 536–543, Van Landeghem et al., Investigation of solute/interphase interaction during ferrite growth © 2017, with permission from Elsevier. (e) Reprinted from *Acta Materialia*, volume 58, 4923–4939, Marceau et al., Solute clustering in Al–Cu–Mg alloys during the early stages of elevated temperature ageing © 2010, with permission from Elsevier.

the development and application of APT in the geosciences. As a result, there is currently a rapidly growing community of researchers applying this technique to geoscience problems (Figure 2; Appendix S1).

The fundamentals of APT

Principle modes of APT

The application of a strong electric field to a small, needle-shaped specimen may cause atoms at the tip of the specimen to evaporate, a process referred to as field evaporation (Müller 1956). APT couples field evaporation with identification of the evaporated species by time-of-flight

mass spectrometry. In contrast with many other analytical mass-spectroscopic techniques, no primary or probe beam (e.g., electrons, ions or electromagnetic radiation) is used to localise the analysis. Instead the high-field region is concentrated and localised by the specimen geometry (Figure 6). The specimen is specifically prepared and shaped in order to allow the controlled removal of ions from the region of interest.

The needle-shaped specimen is prepared with a typical diameter at the apex of 50–100 nm, depending on the material, and with a shank half-angle usually less than 15° over a length of several micrometres. A positive voltage of several kilovolts is applied to the specimen in order to generate a very high electric field at the apex, where it is

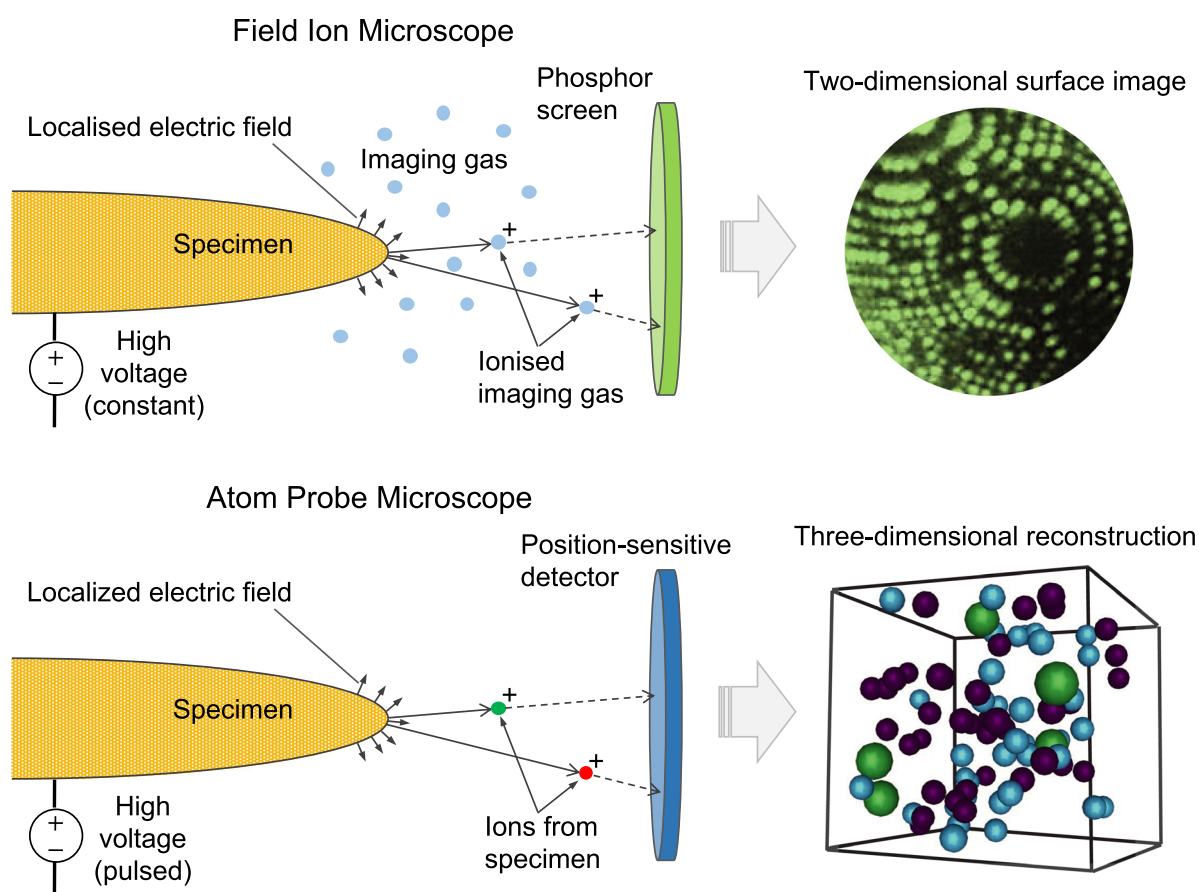


Figure 5. Simplified schematics illustrating the similarities and differences between field ion and atom probe microscopes. Field ion microscopy is an imaging method in which gas atoms are condensed on the surface of the needle-like specimen. They are then ionised by the intense local electric field and accelerated towards an imaging device such as a phosphor screen. Each dot on the image represents a single atom on the specimen surface. APT detects ions that have been removed from the material at the specimen surface and uses digital processing to infer the original 3D location of the atom. Time-of-flight mass spectrometry is used to determine the ion's identity.

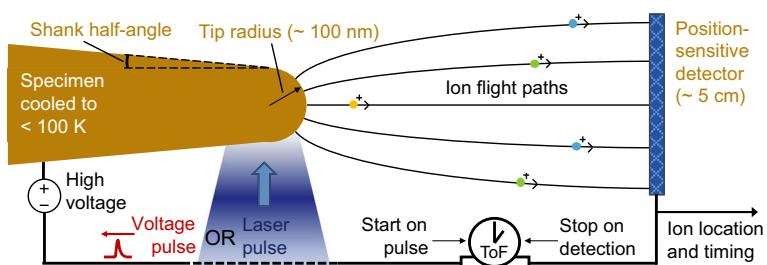


Figure 6. A schematic illustration of APT, including the alternative modes of voltage-pulsing and laser-pulsing operation. Location and timing information from the position-sensitive detector is used to reconstruct the original atomic structure in three dimensions.

enhanced by the small radius of curvature. The field required at the surface for atom probe analysis is typically 10–50 V nm⁻¹ and depends on the physical properties of the

material. For a perfectly conductive specimen the electric field in the material is zero and the surface field (E) may be calculated from electrostatics as

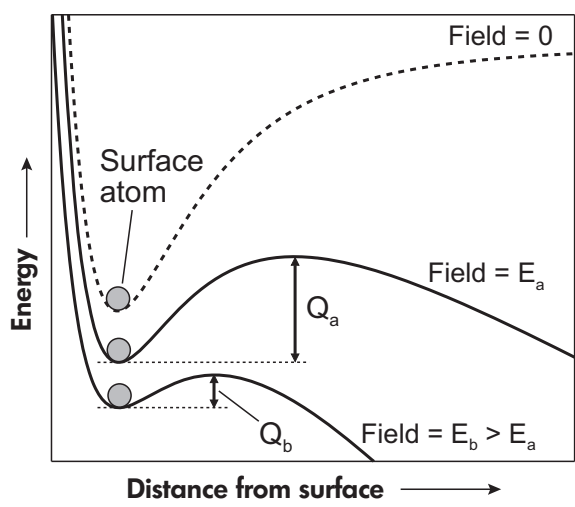


Figure 7. Potential energy curves for an ion close to the specimen surface. The zero-field profile is similar to the energy of a neutral atom under high-field conditions. The energy barrier, Q , must be overcome for field evaporation of a charged ion.

$$E = \frac{V}{kR} \quad (1)$$

where V is the specimen voltage and R is the radius at the end of the needle. In this equation, k is a dimensionless, geometrical field factor that accommodates the shape of the specimen and the local ion-optic environment. The most commonly used configuration is the LEAP, in which an extraction electrode is positioned close to the specimen apex. In this case, k is usually estimated to be between 3 and 3.5 (Kelly *et al.* 1996, Loi *et al.* 2013).

For sufficiently conductive specimens, field evaporation can be achieved using a temporary enhancement of the local electric field by rapidly pulsing the voltage on the specimen or the local electrode. In this ‘voltage-pulsed’ mode, atoms are field-evaporated from the specimen apex at a well-defined time, with the voltage pulse providing the start time for the time-of-flight mass spectrometer. In the ‘laser-assisted’ mode of atom probe analysis, the specimen field is held constant during the evaporation process and the removal of atoms from the surface is stimulated by thermal energy delivered by a short (typically several picoseconds) laser pulse focussed at the specimen apex. The field evaporation of surface atoms, and its dependence on electric field and temperature, is critical to understanding atom probe data collection. These points are illustrated in Figures 7 and 8 and discussed in further detail below.

Following field evaporation and ionisation, ions are accelerated away from the specimen surface and guided

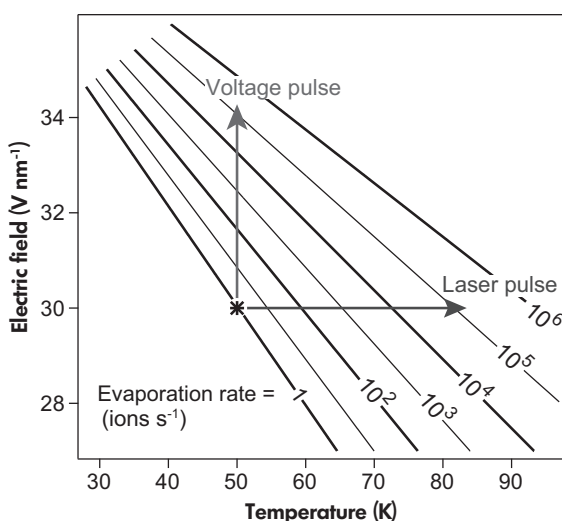


Figure 8. The rate of field evaporation depends on both the electric field and temperature at the specimen surface – plotted here based on a simple thermal-activation model (Vurpillot *et al.* 2009). Both voltage and laser pulsing have the effect of momentarily increasing the evaporation rate, by raising the field and temperature, respectively.

by ion-optics towards the position-sensitive detector. The ‘radial projection’ of the ion flight paths from the specimen tip magnifies spatial differences between the evaporated atoms as they move along the flight path, resulting in a highly magnified and, ideally, uniform ‘mapping’ of the tip surface to the position-sensitive detector. However, the specimen itself is a key element in this mapping, defining the electrostatic environment close to the tip surface, and therefore the initial ion trajectories. As discussed in the following section, this has significant implications for the spatial accuracy of the reconstructed data. Mass spectrometry of the evaporated atoms is achieved by measurement of the time-of-flight, between the pulsed evaporation event and the detector impact.

Field evaporation and its consequences

The process of field evaporation is distinct from ablation or sputtering phenomena and is more analogous to the cold field emission of electrons from sources such as the field-emission gun commonly used in electron microscopes. In the presence of a sufficiently high field, a surface atom can move to a lower energy state by becoming ionised and moving a short distance away from surface (Figure 7). The details of the transition, and how it may be described quantum mechanically are still the subject of debate and research, particularly in the case of semiconducting and insulating materials (Miller and Forbes 2014, Silaeva *et al.* 2014, Karahka and

Kreuzer 2015). However, the essential controls on the process are clear from this simple model: an increase in the field reduces the energy barrier to evaporation, and an increase in the temperature provides more thermal energy for atoms to move over the energy barrier. In this way, field evaporation at the specimen apex may be controlled by changing the voltage or temperature of the specimen (Figure 8).

Current models of field evaporation involve removal of an atom, or molecular complex, from the surface in a positively charged state known as the ‘escape charge-state’. Subsequently, the evaporated ion may undergo further ionisation into a multiply charged state while accelerating through the high-field region near the specimen surface. In contrast to the large variations typically observed for ionisation coefficients of sputtered or ablated ions, the intense electric field required for field evaporation results in ionisation yields close to 100% across all species, providing good counting statistics and reasonable quantitative precision. The strong field conditions also produce a ‘hard’ ionisation that tends to break apart complex molecules into smaller ionised fragments, generally preventing the *in situ* analysis of large molecules but simplifying the mass spectrum and reducing molecular ion mass interferences. Any information on the ionic charge or valence state of the atom in the sample prior to removal is also erased in the field evaporation and ionisation processes, which always produce positive ions.

Atom probe instrumentation

Several variations of atom probe hardware exist that may be used to analyse geological materials. Most recently, however, the overwhelming majority of geological APT work has been conducted in laser-assisted mode using a LEAP. In this context, the following descriptions will include some specifics of contemporary practice where appropriate, while emphasising general principles of APT that are likely to remain relevant with future developments in technology and methods. A comprehensive overview of APT workflow and analysis using a local electrode instrument can be found elsewhere (Larson *et al.* 2013b).

Current APT analyses of geological samples use picosecond-duration laser pulses, almost always in the near ultraviolet (UV), at a wavelength of 355 nm, sometimes referred to as a ‘blue’ laser. Alternatively, some analyses have used a green laser at 532 nm, though comparative studies have shown UV laser pulses to give superior results (Marquis *et al.* 2010, Chen *et al.* 2011, Hono *et al.* 2011, Kelly *et al.* 2014, Santhanagopalan *et al.* 2015).

The ion flight path in a LEAP consists of a short distance from the specimen tip to the electrode, followed by longer ‘drift tube’ section that establishes time-of-flight differences between different ions before they impact the detector. The local electrode (not shown in Figure 6) has a conical shape with a circular aperture at its apex. A typical aperture diameter may be several tens of micrometres (μm), with the specimen tip located a similar distance away. Flight path lengths for atom probe are typically shorter than for other mass spectrometry techniques. The simplest flight path for conventional atom probes is a ‘straight flight path’ similar to that illustrated in Figure 6. Ions travel about 10 cm from the tip to the detector, spreading out along the flight path to give a magnification close to 10^6 . Alternatively, an electrostatic mirror, or reflectron (Mamyrin *et al.* 1973), may be included in the drift tube section of the flight path to improve the intrinsic time-of-flight resolution of the mass spectrometer (Cerezo *et al.* 1998).

Detecting and accurately locating single ions is an essential capability of 3D atom probes. Currently the most common format used for such position-sensitive detectors consists of a multi-channel plate (MCP) front-end, with a delay-line detector that records the secondary electron (SE) signal (Da Costa *et al.* 2005, Lefebvre-Ulrikson *et al.* 2016). Such detectors are highly efficient for ion energies above 3 keV (Gao *et al.* 1984), so all ion types are detected equally, independent of their mass, provided the specimen voltage is greater than 3 kV. The detector efficiency is primarily limited by the open area of the MCP channels, and can be as high as 80% (Prosa *et al.* 2014). The overall ion detection efficiency, from specimen to reconstructed data, is similar to this, but reduces to around 50% when a reflectron is present in the ion flight path (Larson *et al.* 2013b).

A number of mechanisms in both the MCP and the delay-line detector can lead to dead time effects which prevent the detection of multiple-ion impacts that are too close together in space or time (Peng *et al.* 2018). Multiple-ion events are therefore a potential source of quantification error in APT and attempts are usually made to minimise their occurrence by optimisation of the acquisition conditions. This is one reason why a low-threshold electric field, where an average of only one ion is evaporated after a hundred or more pulses, is used (Figure 8). However, in practice multiple-ion events cannot be avoided entirely.

Environmental considerations are also important in atom probe analysis. Acquisitions are usually conducted under ultra-high vacuum conditions, as any residual gas molecules passing close to the specimen tip are likely to be ionised and accelerated to the detector, adding to the background noise. Likewise, molecules that adhere to the surface may be

desorbed by the laser pulse, generating spurious contributions to peaks in the mass spectrum. The specimen temperature is also lowered (20–100 K) as this reduces both the thermal diffusion of surface atoms prior to evaporation and other thermal aberrations that may affect the accuracy of the 3D reconstruction.

Data acquisition

The quality of atom probe data, as measured by various metrics such as the background noise, spatial resolution and mass resolving power, will generally vary with parameters of the atom probe analysis. In laser-assisted mode, the important parameters of an atom probe acquisition are laser pulse energy, pulse repetition frequency, ion detection rate and specimen temperature. The selection and optimisation of these acquisition parameters is critical in obtaining high-quality data, and will depend on the sample material and the specific properties of the specimens to be analysed. These issues are discussed later in ‘Results and Optimisations’. A description of the acquisition and reconstruction procedures is first given below. Of the four key parameters listed above, the temperature is usually held constant throughout the acquisition and is set a few minutes prior to analysis to allow the specimen to reach thermal equilibrium. The other parameters may be adjusted during the initial stages of the acquisition, but are then usually fixed for the bulk of the data collection.

The first stage of an atom probe analysis involves coarse alignment of the specimen to the ion flight path. In a local electrode configuration, the specimen is usually moved on a three-axis translational stage so that the needle axis is aligned with the electrode aperture, a few tens of micrometres away. In laser-assisted mode, the laser spot must also be coarsely aligned to the specimen apex, in the lateral directions (X and Y) and also in focus (Z). Fine alignments of the specimen and laser, as well as adjustment of acquisition parameters, are then conducted while evaporating the first layers of atoms from the specimen surface, with the ion detection signal providing the information required for alignment. In most cases, several nm of material will be evaporated during this phase, while the tip is formed to a near-hemispherical shape, before useful data can be acquired. This phase of the acquisition usually requires 10–30 min of manual operation. Once suitable acquisition parameters have been set and the field is near the appropriate threshold level, the acquisition may progress in a fully automated mode. The ion detection rate and laser alignment are then maintained by automatic adjustments of the specimen voltage and laser targeting, based upon ion signals from the detector.

For laser-assisted acquisitions, the continuous, controlled evaporation of the specimen can be understood with reference to Figure 8. In this case, the specimen temperature is set to 50 K and the surface electric field is held at a ‘threshold’ value of 30 V nm^{-1} , as determined by the specimen voltage (Equation 1). In this state the mean evaporation rate will be at a threshold level of around 1 ion s^{-1} . When the laser pulse energy is absorbed by the tip, the temperature increases locally, resulting in an exponential increase in the evaporation rate (blue arrow in Figure 8) for the duration of the heat pulse (typically $< 1 \text{ ns}$). Although the evaporation process is stochastic, for a given laser pulse energy the field can be adjusted (through the specimen voltage) to a suitable threshold value so that a desired mean rate of ion detection (Φ_D) is achieved (typically 0.002–0.02 ions/pulse). This leads to typical acquisitions progressing at several thousand ion s^{-1} depending on the selected pulse frequency of the laser.

To maintain a user-defined target value of Φ_D , the field at the surface must be kept at a suitable threshold level. However, due to the shank angle of a typical specimen needle (Figure 6), the tip radius will naturally increase throughout the acquisition as atomic layers are removed and the needle is shortened. This leads to a reduction in the surface field (Equation 1), and therefore a slowing of the ion evaporation and detection rates. The control software monitors the detection rate (Φ_D) and will respond to a decrease by raising the specimen voltage (Figure 9), thereby increasing the surface field and the field evaporation rate (Φ_E) until the detection rate meets the target value.

The voltage at which a specimen first begins to evaporate under controlled conditions, sometimes referred to as the ‘turn on’ voltage, is dependent on the evaporation field of the sample material, and the tip radius (Equation 1). Specimens must therefore be prepared with a suitable end-form to allow data acquisition within a practical voltage range: typically, above 3 kV to ensure efficient ion detection, and below 15 kV due to engineering constraints on the maximum voltage. Likewise, the specimen shank angle will affect how quickly the specimen radius, and hence the voltage, increases during the acquisition, and therefore how much data may be collected before a maximum voltage limit is reached (Figure 9). Changes in the material composition (Tsong 1978) or crystal orientation (Verberne *et al.* 2019) may also influence the evaporation field required to meet the target detection rate. Therefore, mixed-phase samples may produce fluctuations in the specimen voltage and may also disturb the ion flight paths.

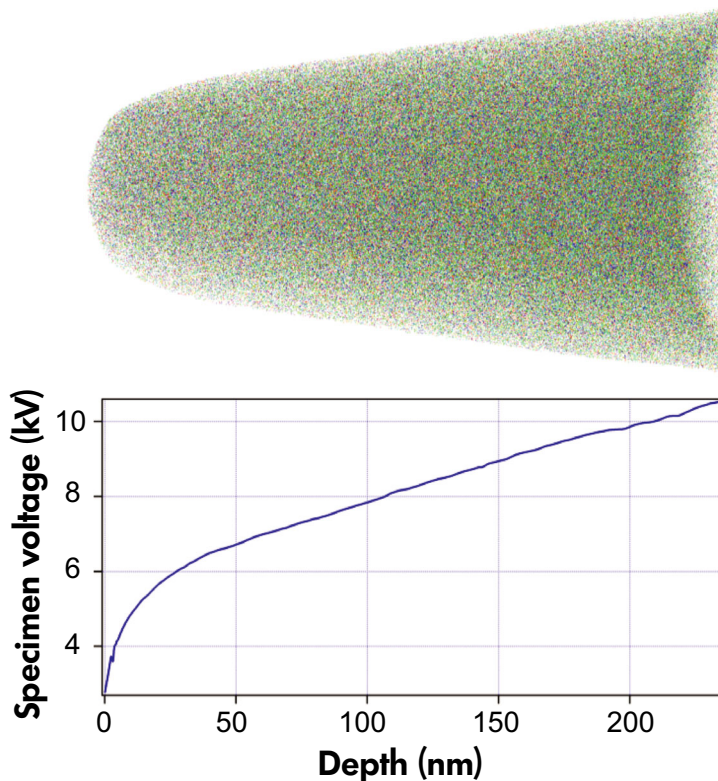


Figure 9. Atom map of a three-dimensional APT reconstruction containing over 100 million atoms (top). Graph shows the voltage at which ions were evaporated from the sample, versus their depth within the reconstruction (bottom). As the acquisition progresses, the voltage increases in order to counteract the increasing tip radius (Equation 1) and maintain a constant rate of ion detection.

Acquisitions may be programmed to stop automatically after a target number of ions or maximum specimen voltage is reached. However, due to the intense electric field required for field evaporation and the associated mechanical stress, it is common for analyses to end due to rupture of the specimen during the acquisition. In geological materials, the failure mechanism is usually catastrophic, involving material fracture and the melting of several micrometres of material from the tip (Kölling and Vandervorst 2009). However, minor fractures may be followed by a re-forming of the needle end and continuation of data collection.

Data reconstruction

Reconstruction of the atom probe data refers to the processing of ion detection events, including timing, spatial and ion-sequence information, to produce a model of the original 3D atomic arrangement of the sample volume. There are both spatial and chemical-isotopic components of the reconstruction.

The spatial reconstruction may be separated into the lateral (X- and Y-coordinates) directions and the depth (Z-coordinate) direction. The reconstructed lateral coordinates are derived from the detector impact location by using a reverse-projection model to trace the ion flight path back to the original point of evaporation from the specimen surface. To achieve this, many different models have been proposed and used, with most employing a point projection approximation or constant magnification model to map coordinates between the specimen and detector surfaces (Blavette *et al.* 1982, Bas *et al.* 1995). Modern reconstruction algorithms have been further developed for wide-angle, LEAPs (Geiser *et al.* 2009, Gault *et al.* 2011, Vurpillot *et al.* 2013). Knowledge of the specimen radius at each point throughout the acquisition is critical to the X, Y reconstruction, as this directly affects the lateral magnification between the specimen and detector surfaces.

The Z-coordinate, or depth location, of each detected ion is determined primarily by the sequence of evaporation. A volume quantity is assigned to each ion, based on the

assumed mean atomic density of the sample, or the sample volume expected to be occupied by the detected ion species. This density information is another critical input into the reconstruction of APT data, and may lead to artefacts in cases where the atomic density varies within a sample, or where atoms of a particular type occupy a different volume depending on their host phase. Knowledge of the specimen radius is also required to determine the reconstructed Z position when transforming ion impact coordinates at the detector to atomic locations on the curved surface of the specimen tip.

Further details of APT reconstruction algorithms are given in several recent reviews (Vurpillot *et al.* 2013, Larson *et al.* 2013a, De Geuser and Gault 2017). Each model contains limitations, even for homogenous materials and perfectly smooth and regular tip shapes. Further complications arise due to crystallography, grain boundaries and other crystal defects, changes in chemistry or mineral phases. These will generally lead to local surface distortions as some atoms are preferentially evaporated out of their normal sequence due to relatively weaker or stronger bonding (Larson *et al.* 2011, 2012). Currently such distortions cannot be completely rectified, and inevitably some spatial inaccuracies will be present in reconstructions containing multiple phases, crystal defects, or significant chemical inhomogeneities (see the section entitled *Technique limitations, analysis artefacts and potential solutions*).

The chemical component of data reconstruction involves identification of the detected ions, which may be evaporated as elemental or molecular ion species, and can be singly or multiply charged. The mass-to-charge ratio of each ion is calculated using standard time-of-flight spectrometry:

$$\frac{m}{q} = \left(\frac{2}{D^2} \right) \times V \times t^2 \quad (2)$$

where m and q are the mass and electrical charge of the detected ion, D is the distance that the ion travels to the detector in a time-of-flight, t , and V is the specimen voltage. Corrections must be made for each individual ion to allow for variations in D and V , which depend on the particular ion flight path (derived from the ion impact location) and the specimen voltage at the time of evaporation.

A histogram of the mass-to-charge values (measured in Daltons, Da) is generated as a ‘mass spectrum’, and the mass values are calibrated from known mass peaks. A typical spectrum collected from a feldspar sample indicates the presence of single and molecular ions at different multiple charge states and further illustrates the ability to distinguish between different isotopes (Figure 10). The

capacity to identify and separate mass peaks is dependent on the mass resolving power (MRP), defined as an inverse measure of the mass peak width (Δm) with respect to the mass-to-charge value (m):

$$MRP_{FWHM} = (m / \Delta m_{FWHM}) \quad (3)$$

where ‘FWHM’ refers to the full width of the mass peak at half of its maximum value (full-width at half-maximum). Current commercially available straight flight path atom probes have a mass resolving power of 500–600, but MRP values of 1000–1200 can be achieved when using a reflectron in the flight path to compensate for small differences in ion energies. This is sufficient to resolve isotopes having different atomic mass numbers, but does not allow full separation of isobaric interferences, such as between $^{24}\text{Mg}^{16}\text{O}^+$ and $^{40}\text{Ca}^+$.

Finally, ion identities are assigned by defining intervals or ‘ranges’ within the mass spectrum for each elemental or molecular ion type. Although peak identities are usually decipherable, the exact definition of range boundaries is decided by each user, and there is currently no universally adopted method for defining such ranges. Together with overlapping peaks and inconsistent peak shapes, this places limits on the repeatability and quantification of APT chemical and isotopic information. This is a current area of research interest, with several approaches put forward for improving peak identification and quantification (Hudson *et al.* 2011, Johnson *et al.* 2013, Haley *et al.* 2015, London *et al.* 2017, Blum *et al.* 2018, Vurpillot *et al.* 2019).

Performance and optimisations

Spatial resolution

A key strength of atom probe analysis is the spatial resolution that may be achieved for chemical and isotopic mapping in three dimensions. For samples consisting primarily of a single chemical element, such as dilute metal alloys or doped semiconductors, it is often possible to resolve atomic planes in the reconstructed atom maps. Such samples can be used to define reasonable metrics for the spatial resolution, which has been shown to be small as 0.02 nm in the z-direction, and 0.4 nm in the lateral dimensions (Gault *et al.* 2009, 2010, Moody *et al.* 2014, Wallace *et al.* 2018). Visualisation of atomic planes is reliant on ordered field evaporation of individual atoms from crystalline surfaces. However, such ordered evaporation is not typically observed for many geological materials such as oxides and silicates.

For complex materials, and inhomogeneous samples containing multiple phases, the spatial resolution is affected

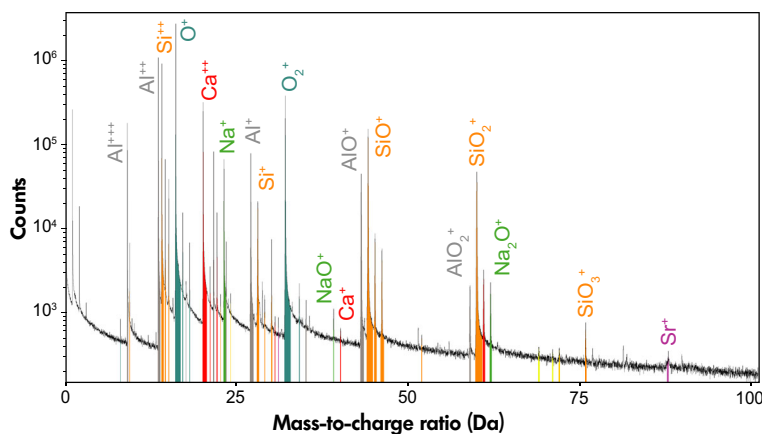


Figure 10. Example of a mass spectrum from a feldspar sample (figure 4 of Cao *et al.* 2019), illustrating some of the complexity typical for geological specimens. Mass-to-charge ratio is measured in Daltons (Da). High-order charge states, molecular ion complexes, and multiple isotopes are clearly visible. Colours indicate mass ranges associated with various ion species. Reprinted from *American Mineralogist*, volume 104, 391–402, Cao *et al.* © 2019 with permission from the Mineralogical Society of America.

by mechanisms that may alter the ion trajectories and therefore corrupt the detector-to-sample ion projection required for accurate reconstruction. At the smallest scale, the atomic structure of the tip surface will lead to local electric fields that do not simply reflect the global tip shape. Such effects, for example, due to local field distortions at atomic terrace step-edges in crystalline samples, are referred to as trajectory aberrations (Waugh *et al.* 1976, Vurpillot *et al.* 2000b). Larger-scale distortions can occur wherever there are differences in the field strength required to evaporate atoms from local regions on the surface (Figure 11). These effects, known as ‘local magnification’, illustrate an important limitation in obtaining an accurate spatial reconstruction. The atom probe specimen itself functions as the ion source, and its surface features have a primary influence on the local electric field and therefore on the ion flight trajectories. While methods have been developed to partially compensate for some surface-induced distortions (Vurpillot *et al.* 2004, De Geuser *et al.* 2007b), care should be taken when interpreting spatial reconstructions adjacent to phase boundaries or crystal defects as local magnification effects may be present (see Technique Limitations, Analysis Artefacts and Potential Solutions).

Spatial information may also be degraded or lost due to surface diffusion of atoms prior to field evaporation. Thermal energy provided by a high base temperature or high laser pulse energy may be sufficient to overcome surface diffusion barriers for certain atomic species, depending on the field and surface topography. Information is also compromised by the evaporation of molecular ions, which may contain

several atoms that register the same detector impact location, and therefore the same position within the reconstruction despite originating from different locations within the sample.

Quantitative capabilities

In most cases APT provides results that are quantitatively accurate at the 0.01 at.% level (Thompson *et al.* 2006, Thuvander 2016). While, in principle, quantification is limited only by counting statistics, in practice other uncertainties are usually present due to choices of mass peak ranging, peak overlaps, and differences between mass peak shapes, among other factors (Johnson *et al.* 2013, Larson *et al.* 2013b, London *et al.* 2017).

Several recent studies have compared APT compositional results from geological samples with those from other geoanalytical techniques (Pérez-Huerta *et al.* 2016, Daly *et al.* 2018, Exertier *et al.* 2018, Reinhard *et al.* 2018, Saxe *et al.* 2018b). Most comparisons provide excellent agreement, within the uncertainty arising from counting statistics in the atom probe data. Where there are significant discrepancies, they can often be reduced or eliminated by a suitable selection of acquisition parameters (Devaraj *et al.* 2013). Some results show a consistent deficiency in oxygen in oxide or silicate minerals, which cannot be removed by parameter optimisation. This appears related to compositional anomalies seen in some semiconductor materials, such as the loss of nitrogen in the APT analysis of GaN, or oxygen deficiency in acquisitions from ZnO and MgO (Riley

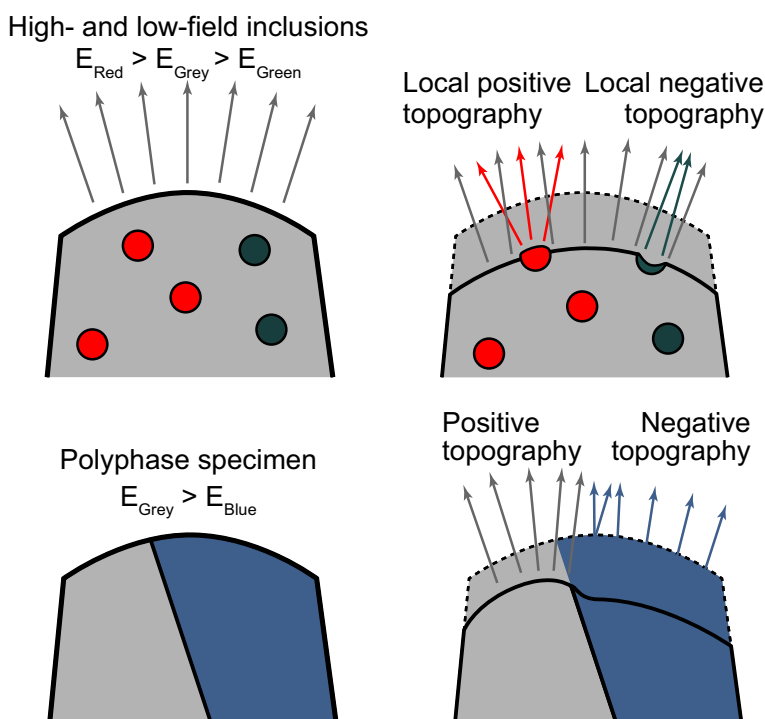


Figure 11. Local magnification effects associated with clusters and interfaces. Figures on the left show initial geometry. Figures on the right indicate trajectory aberrations associated with high- and low-field materials.

(*et al.* 2012, Mancini *et al.* 2014). The mechanisms underlying the loss of oxygen are not fully understood, though the fragmentation of evaporated molecular ions may play a role in producing neutral oxygen atoms or oxygen-containing molecules that go undetected (Saxey 2011, Karahka *et al.* 2015, Gault *et al.* 2016).

Unlike many other mass spectrometry techniques, and X-ray chemical analysis methods, atom probe data do not require correction by relative sensitivity factors that may vary by orders of magnitude, or large corrections due to matrix effects. The extremely high electric field local to the specimen surface ensures that atoms and molecules removed from the samples are ionised with near-100% efficiency. However, while gross differences between elemental sensitivities are avoided, more subtle effects can still be present and may result in chemical or isotopic compositional biases. The position-sensitive detector has some dead time associated with the impact of each ion, so that a high flux of multiple-ion events will lead to a loss of data, which may preference particular mass peaks (Thuvander *et al.* 2011, 2013, Meisenkothen *et al.* 2015, Thuvander *et al.* 2019). The precise nature of the dead time, which may include spatial proximity as well as coincidence limits, can be complex and will depend on the specific construction of the detector hardware (Peng *et al.* 2018). Due to the limitations imposed

by detector dead time, the occurrence of multiple-ion events is usually minimised by optimisation of the acquisition conditions. In general, a lower electric field will tend to reduce the frequency of multiple events (De Geuser *et al.* 2007a, Müller *et al.* 2011, Saxey *et al.* 2018b, Verberne *et al.* 2019), which can be achieved by increasing the laser pulse energy or reducing the evaporation rate.

Chemical and isotopic detection limits depend largely on the background noise in the mass spectrum local to the mass peaks of interest, and the presence and size of potential mass interference peaks. The background may be due to ‘white’ noise over the entire spectrum, which is always present, or may be dominated locally by the presence of a large tail from an adjacent peak. For good-quality data from geological specimens, most elements will be detectable at $\sim 10 \mu\text{mol mol}^{-1}$ if no significant interferences are present. Mass interferences can usually be reduced by increasing the electric field (lower laser pulse energy or higher evaporation rate).

Reference materials or ‘standards’ are not routinely used in atom probe analysis. The high ionisation efficiency across all evaporated species alleviates the need to compensate for large differences in elemental sensitivities. Furthermore, although some quantitative correction may improve results,

the usefulness of a reference materials-based approach to quantitative correction is unclear since it is difficult to control for all data acquisition variables between sample and reference specimens. In particular, variables such as the specimen geometry and other aspects of the specimen preparation (see *Sample selection and preparation*) are difficult to control when specimen needles are prepared from different samples. The central importance of the specimen in determining the behaviour of ions in the data collection process makes these variables critical in any attempt to calibrate the instrument using reference materials. The issues of quantitative accuracy and data correction are currently active areas of research.

In comparison with conventional geoanalytical techniques, APT can be regarded as having a limited field of view, excellent spatial resolution, with moderate chemical–isotopic sensitivity and mass resolving power (Table 1).

Atom probe tomography of geological materials

Geological samples have some general characteristics relevant to their analysis by APT. Since most geological materials have a low electrical conductivity, specimens are almost exclusively analysed in the laser mode of APT. However, in the case of metallic materials or semiconducting mineral phases (e.g., some sulfides and tellurides), it is possible to acquire data in the voltage-pulsed mode of operation.

The mechanisms underlying field evaporation are reasonably well understood for metals. However, for insulators, or materials with a wide electrical band gap, questions remain about how the laser pulse energy is absorbed by the specimen, leading to removal of surface atoms, and this limited understanding impacts on the ability to optimise APT data acquisitions (Karahka and Kreuzer 2015). Several factors appear to be important in understanding the

unexpected behaviour of non-conducting samples in APT. Due to the nanoscale specimen geometry, samples may exhibit behaviour very different from those observed in the bulk material. Surface physical and chemical properties may dominate over bulk effects, and the extremely high electric field can distort electrical states. In fact, it is widely understood that in the presence of the extremely high electric fields required for field evaporation, dielectric or insulating materials become electrically conductive at the surface (Miller and Forbes 2014, Silaeva *et al.* 2014), allowing field evaporation processes to continue as for semiconducting materials.

Poor thermal conductivity of some minerals, particularly oxides, can reduce the cooling rate of the specimen tip following a laser pulse. This leads to extended mass peak tails in some common minerals, such as apatite and rutile (Gordon *et al.* 2012, La Fontaine *et al.* 2016, Verberne *et al.* 2019) which may elevate the local background for other peaks of interest within the spectrum. Adjustments in the laser pulse energy and evaporation rate may make some improvements to peak tails and overall background (Verberne *et al.* 2019).

When analysing geological materials by APT it is common to observe many molecular ion species in the mass spectrum, as well as a high proportion of multiple-ion detection events. This has been interpreted as resulting from the evaporation of molecular complexes from the surface, some of which fragment to smaller ionic species during their flight to the detector (De Geuser *et al.* 2007a, Saxy 2011). In general, there is a trade-off between a desired simplification of the mass spectrum, which tends to occur under high-field running conditions, and a reduction of multiple-ion events, which is usually achieved by lowering the electric field.

Sample selection and preparation

Analytical workflow prior to APT characterisation

APT involves the detailed analysis of a very small volume of material (typically $< 0.02 \mu\text{m}^3$). Such small volumes of material may not be representative of the sample as a whole and APT is therefore not ideal as a bulk analysis technique. Where APT excels is in the targeted analysis of particular features within the material of interest. Such site-specific targeting requires integration of APT with other larger length-scale analytical techniques. However, it also requires that the analysed specimen is taken from a known scientific context and that there is a sound scientific rationale for targeting any particular feature. For natural geological samples, the

Table 1.
Typical analytical capabilities for atom probe analysis of geological materials using modern APT platforms

APT capabilities	
Mass resolving power ($m/\Delta m_{\text{FWHM}}$)	1000–1200
Detection limit	$10 \mu\text{mol mol}^{-1}$
Spatial resolution	$\sim 0.4 \text{ nm in } x-y \sim 0.02 \text{ nm in } z$
Field of view (x,y,z)	100, 100, 1000 nm

^a Quoted value for spatial resolution is based on analysis of pure metals and for geological materials may be expected to be $\sim 1 \text{ nm}$ due to more disordered evaporation.

process of sample selection is initially similar to other microanalysis techniques, with rock samples from well-characterised igneous, sedimentary or metamorphic terrains being collected during fieldwork, and progressively smaller regions of interest then being selected and sequentially characterised (Figure 12). Thin sections or grain mounts are commonly used, though unpolished fracture surfaces or powders can also be utilised. A similar approach of sequentially smaller volume characterisation can be used in experimental studies where specific scientific problems are being targeted.

Establishing the geological and geochemical context of the APT analytical volume can be achieved by a myriad of available characterisation techniques. The selection of which complementary analytical techniques are employed is dependent on the information being sought to address a specific scientific problem. The combination of these techniques with APT enables the correlation of trace element and isotopic signatures over a range of length scales.

In geological studies, scanning electron microscopy (SEM) is a readily available tool for sample characterisation and it commonly underpins the interpretation of atom probe data. Surface analyses by field-emission SEM (e.g., SE, backscattered atomic-number contrast electron (BSE) and forescatter orientation contrast electron imaging) is non-destructive and commonly has sufficient spatial resolution (≤ 10 nm) to identify regions of interest for APT targeting. Cathodoluminescence (CL) imaging provides micrometre-scale compositional constraints related to trace element distributions in minerals and these can be particularly useful

for identifying atom probe targets, for example, in zircon (e.g., Peterman *et al.* 2016). Electron backscatter diffraction (EBSD) data can be collected with a spatial resolution down to ~ 30 nm, has mapping capability, and can be used for both phase identification and microstructural characterisation. As such, EBSD maps can be used for APT targeting of phase boundaries and microstructural features such as low-angle boundaries (Miller and Russell 2007, Miller *et al.* 2007, Thompson *et al.* 2007b, Piazolo *et al.* 2016, Reddy *et al.* 2016, Fougerousse *et al.* 2019).

Energy-dispersive X-ray spectroscopy (EDS) enables the identification of compositional changes down to $\sim 0.5\%$ m/m, and can also be used to locate interphase boundaries in samples. Similarly, SEM-based wavelength-dispersive spectroscopy (WDS) and electron probe microanalyser (EPMA) can also be used to identify compositional targets for atom probe analysis. However, the coarse spatial resolution (> 1 μm) associated with X-ray analysis presents challenges when correlating the information with APT tips that are ~ 100 nm in diameter. The limited ability of these techniques to measure trace elements, often the aim of atom probe analyses, further limits the use of these approaches in APT specimen targeting.

Spot analyses using ion microprobes or laser ablation inductively coupled plasma-mass spectrometry (LA-ICP-MS) provide high-sensitivity quantitative information that can significantly aid the interpretation of atom probe data (e.g., Peterman *et al.* 2016). Despite, such techniques being considered as relatively high-resolution analytical techniques, the volume of material analysed is up to a million

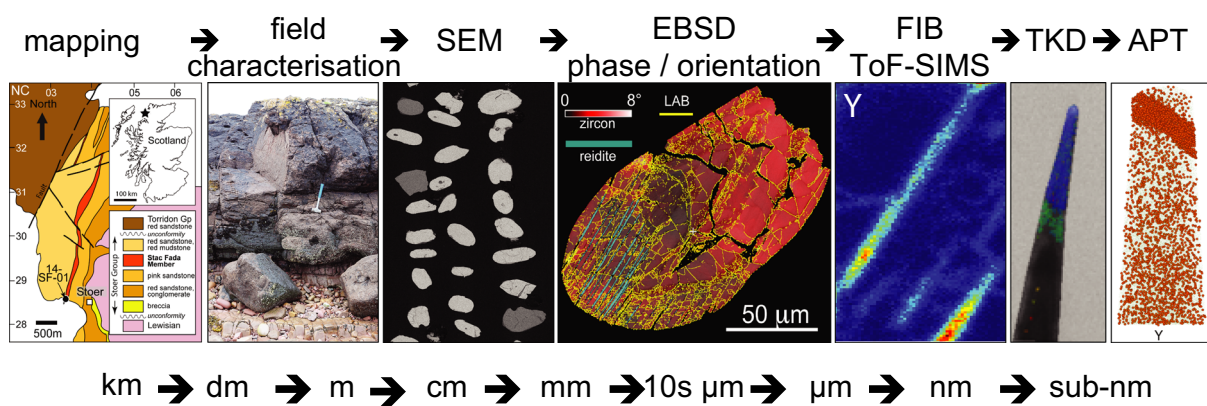


Figure 12. Example of a typical analytical workflow used for geological sample characterisation prior to APT analysis. Illustrated workflow starts with geological mapping and progresses through higher spatial resolution techniques. In this example, the approach provides context for the targeting and interpretation of nanoscale compositional heterogeneities reported by Reddy *et al.* (2016). Reprinted from *Geochimica et Cosmochimica Acta*, volume 195, 158–170, Reddy *et al.*, Mechanisms of deformation-induced trace element migration in zircon resolved by atom probe and correlative microscopy © 2016, with permission from Elsevier.

times greater than typical APT volumes. Such techniques are also destructive over relatively coarse sample sizes (typically > 10 µm diameter pits). These two features limit their ability to be used for site-specific APT targeting, but provide useful constraints on 'bulk' compositions of the host mineral. However, elemental and isotopic mapping can be done by ion imaging techniques, which provide micrometre-scale spatial resolution (e.g., Bellucci *et al.* 2016, Whitehouse *et al.* 2017) and such images have provided the context for the discovery of nanoscale Pb nanospheres in radiation damaged zircon (Kusiak *et al.* 2015), which have the potential to be targeted for atom probe analyses.

The recent developments in high-spatial-resolution analytical technologies enable several techniques to be employed for imaging of elemental and isotopic compositional variations at < 100 nm lateral resolution. The spatial resolution of SIMS analysis is related to the probe size of the primary ion source. Modern ion sources (commonly Cs and O) can achieve probe sizes down to 50 nm. Even smaller probe sizes (< 10 nm) are achievable with liquid metal ion guns (LMIG) with ions such as Ga which enable better than 50 nm lateral resolution ion imaging (Alberts *et al.* 2014). NanoSIMS is a high-spatial-resolution, multi-collector instrument that has high sensitivity across most of the periodic table (Hoppe *et al.* 2013). Several studies have integrated NanoSIMS with APT to assess element segregation from the micrometre to the nanometre scale during crystal growth and interface development (Wu *et al.* 2019).

Time-of-flight SIMS (ToF-SIMS) can provide similar spatial resolution to NanoSIMS, but in most high-resolution systems, the sensitivity of ToF-SIMS is significantly lower. An advantage of the ToF-SIMS techniques is that compositional information is collected across the whole periodic table and it is not necessary to preselect a limited number of masses. In addition, ToF-SIMS instruments provide mass-to-charge ratio spectra like those generated by APT, but the different acquisition conditions mean that some m/q peaks are found in different positions. This can help with identification of peaks and highlight potential interferences in the atom probe data (Figure 13). Furthermore, the incorporation of ToF-SIMS systems into focussed ion-beam scanning electron microscopes (FIB-SEM) used for atom probe specimen preparation enables compositional information to be used for targeting (Rickard *et al.* 2020). ToF mass spectrometry is also used in the recently developed Chicago Instrument for Laser Ionization, a resonance ionisation mass spectrometer that has similar sensitivity to APT, albeit at lower spatial resolution, but has the ability to reduce peak interferences by utilising different ionisation lasers (Stephan *et al.* 2016).

Transmission electron microscopy (TEM) has comparable spatial resolution to APT and has the unique ability to characterise specific microstructures such as individual dislocations. For these reasons, TEM and APT are extremely complementary and the integration of these two techniques has the potential to revolutionise our understanding of the role of defects in controlling the compositional modification of minerals. TEM can be conducted on a separate specimen taken from close to the site of atom probe specimen preparation (Krakauer and Seidman 1992, Gin *et al.* 2017, Montalvo *et al.* 2019, Seydoux-Guillaume *et al.* 2019). In such cases, care has to be taken with the extrapolation of observations by the individual techniques. A potentially better approach is to undertake TEM analysis on the atom probe needle specimen prior to APT analysis (Lefebvre *et al.* 2015). Additional details on the TEM characterisation of APT needles are provided in the *Specimen characterisation* section.

Specimen manufacture

Specimen preparation for APT can be challenging as the region of interest must be precisely located within the analysed volume (top ~1 µm of the needle) and the specimen must be carefully shaped such that the electric field can be concentrated at the end of a sharp tip (diameter < 100 nm). For conductive specimens, which is not normally the case for geological samples, APT needles can be prepared by electropolishing (Melmed and Carroll 1984), with a range of different electrolytes being used for different materials (see appendix B of Gault *et al.* 2012b). Generally, such techniques are not site-specific, although targeting of specific interfaces is possible (Krakauer *et al.* 1990).

In recent years, site-specific sample preparation of both conductive and non-conductive materials has increasingly utilised FIB-SEM (Waugh *et al.* 1984, Alexander *et al.* 1989, Larson *et al.* 1999), and a number of methods for FIB-based specimen preparation have been developed (e.g., see reviews by Miller *et al.* 2007, McKenzie *et al.* 2010, Blum *et al.* 2016, Prosa and Larson 2017). However, most facilities now use a similar methodology for site-specific atom probe specimens (Figure 14). This method involves the deposition of a small, rectangular, protective Pt capping layer over the region of interest followed by the removal of a 2.5 µm wide triangular prism, with a length dependent on the number of required APT tips. Segments of the prism (approximately 2 µm wide) are then mounted on pre-sharpened posts on a silicon coupon and ion beam milled with an annular mask to produce a needle shape with a final tip diameter < 100 nm (Figure 14). The mounting of regions of interest onto 'micro-tips' on a single coupon simplifies specimen preparation

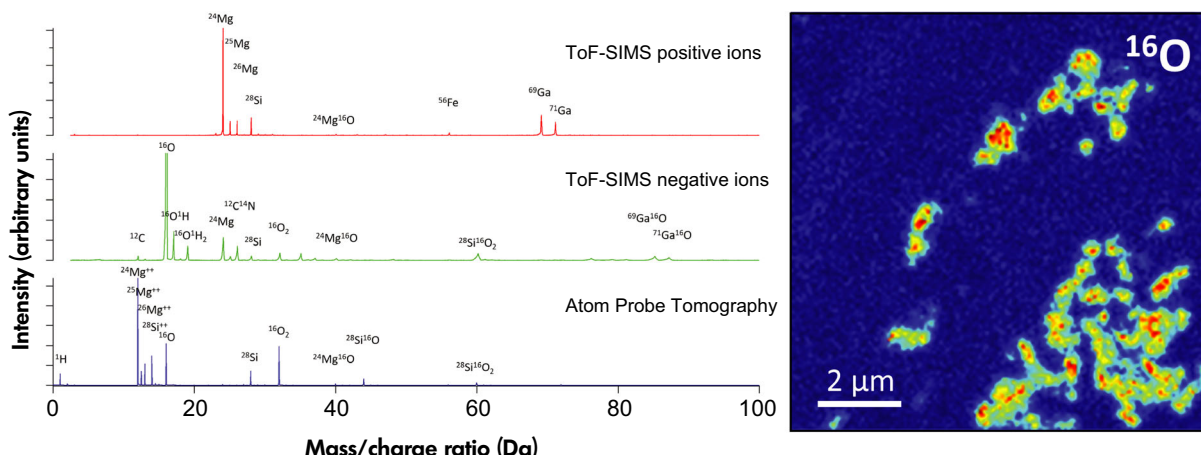


Figure 13. Left: Comparison between APT and ToF-SIMS mass spectra from an olivine ($(\text{Mg}, \text{Fe})_2\text{SiO}_4$) sample. Positive and negative ToF-SIMS spectra are displayed. Gallium peaks are from the FIB primary ion source. Right: FIB-ToF-SIMS map of oxygen in a coal sample containing kaolinite ($\text{Al}_2\text{Si}_2\text{O}_5[\text{OH}]_4$) particles.

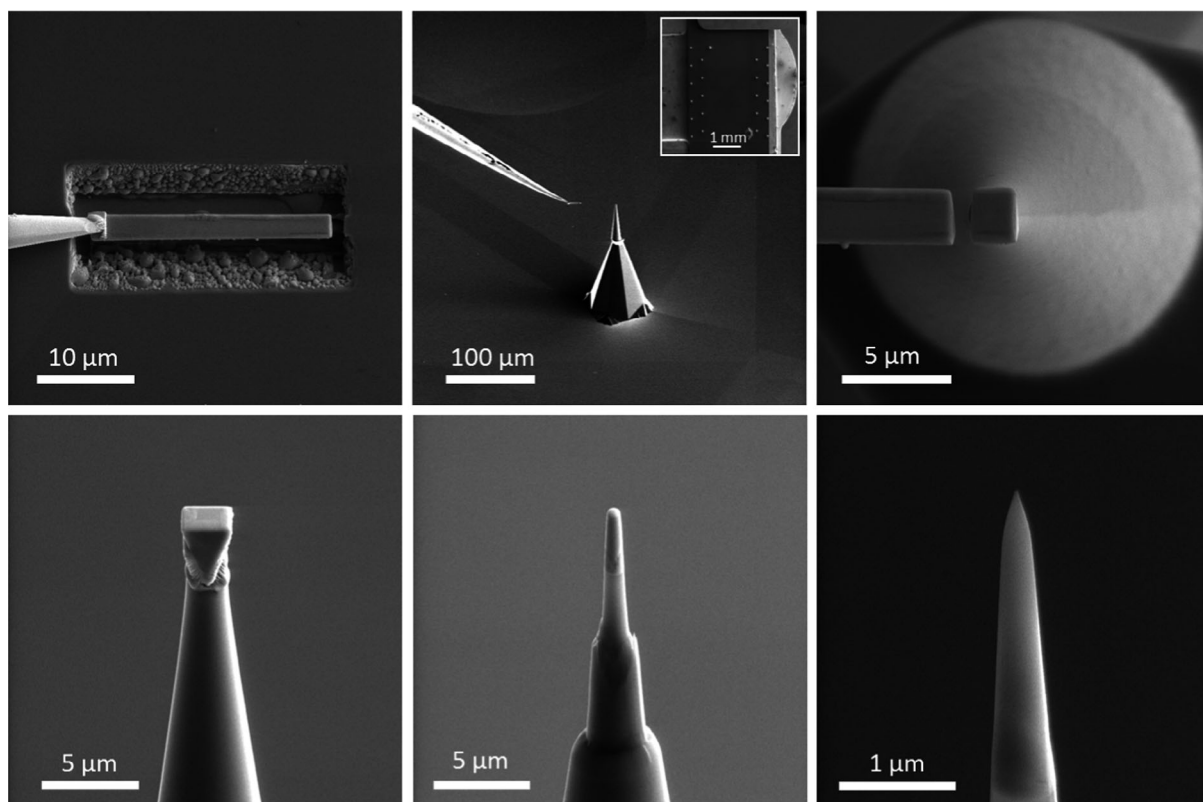


Figure 14. Series of secondary electron images demonstrating the sequential lift-out, sample mounting and tip-shaping stages of APT specimen preparation by FIB-SEM.

and handling (Thompson *et al.* 2005), while mounting onto a TEM grid enables correlative microscopy studies (Gorman *et al.* 2008). The most challenging aspect of the preparation is in positioning the specific region of interest centrally

(< 50 nm from the axis of the specimen) within the needle and close to the apex (<< 1000 nm, ideally ~ 250 nm). A misalignment of just a few tens of nm can cause the region of interest to be out of the analytical volume of the atom probe

specimen. Hence, approaches have been developed that enable regions of interest to be marked by electron deposition of Pt on the feature of interest, such that the feature is exactly located in the analytical volume of the specimen (Lotharukpong *et al.* 2017, Prosa and Larson 2017, Rickard *et al.* 2020).

Although the lift-out method has been largely successful, ion-beam milling rates vary with sample composition and grain orientation (Prentitzer *et al.* 2003) and this can make it difficult to have a standard preparation routine. Additional challenges come with multiphase materials and porous samples where milling rates vary within the lift-out. However, modern FIB-SEM instruments enable the milling processes to be carefully monitored, allowing the operator to make fine adjustments to optimise milling routines for a specific sample.

Beam damage and ion implantation (usually Ga) are potential drawbacks of FIB-SEM lift-out for APT analysis. During sample preparation high-energy ions from the FIB induce a collision cascade within the near surface of the sample, which can make it amorphous and leave primary ions implanted into the structure. The depth of Ga ion implantation in silicon has been shown to be related to the accelerating voltage of the FIB beam, with a 30 and a 5 kV beam causing Ga implantation to 50 and < 10 nm, respectively (Thompson *et al.* 2007b). In most cases, a low kV (\leq 5 kV) final annular milling step is applied to APT tips to ensure beam damage and ion implantation are minimised. In addition, the recent development of xenon plasma FIB systems, which remove the Ga contamination problem, has significant potential for atom probe sample preparation (Halpin *et al.* 2019).

One aspect of specimen preparation relates to the analysis of nanoparticles by APT. These materials are generally difficult to work with. However, a number of studies have successfully developed specimen preparation techniques based around electrophoresis (Tedsree *et al.* 2011), encapsulation (Heck *et al.* 2014, Larson *et al.* 2015, Yang *et al.* 2016) and agglomerated powder lift-out (Xiang *et al.* 2013). Each approach has benefits and disadvantages (see review by Felfer *et al.* 2015) depending on the nature of the nanoparticles being analysed. Further work is needed in this area for optimisation of nanoparticulate analysis of geological materials.

Correlative characterisation of geological atom probe specimens

Even when the geological context is well established and site-specific targeting has been employed, atom probe

compositional data still contain artefacts due to limitations in the ability to acquire, range and reconstruct all atoms and their positions within a specimen. The characterisation of atom probe specimens by complementary analytical techniques may alleviate some of the problems associated with these artefacts. As a result, it is widely recognised that non-destructive, correlative analyses of the needle-shaped specimen, prior to atom probe analysis, provides invaluable data for the correct interpretation of atom probe results.

Field-emission SEMs have sufficient resolution to accurately measure tip shapes and sizes and are thus used to ensure the specimen has suitable size and shape for APT. Since the electric field applied to specimens is inversely proportional to the tip radius (Equation 1), and different minerals have different evaporation fields, atom probe specimens can be milled precisely to optimise the acquisition conditions. This may prevent either the evaporation of atoms at very low voltages, which leads to poor quality data, or the requirement of very high voltages to cause evaporation, which tends to reduce specimen yield. Both secondary and backscattered electrons can be used for this purpose. BSE imaging can also be used to identify any significant variations in composition within the atom probe specimen and ensure the capping layer and coating has been removed during annular milling in the FIB-SEM.

In cases where atom probe acquisition is stopped prior to tip failure, reimaging of the specimen after the analysis, and comparison with images taken before the analysis allow the analysed volume to be precisely measured (Figure 15). This information can be used to establish, or refine, the correct reconstruction parameters for a particular mineral. This is a critical step in the atom probe reconstruction of geological materials but, so far, such an approach has only been undertaken for zircon (Saxey *et al.* 2019) and rutile (Verberne *et al.* 2019).

Atom probe specimens are extremely thin and the apex of the needle is electron transparent at moderate accelerating voltages ($>$ 20 keV). Hence, the microstructure of the needle can be characterised by transmission Kikuchi diffraction (TKD) in a SEM and TEM. TKD is a similar technique to EBSD as it uses diffraction patterns formed by the interaction of the electron beam with a crystal lattice to provide phase and lattice orientation information at resolution down to a few nanometres (Keller and Geiss 2012, Trimby 2012). TKD was originally applied to thin TEM foils to complement TEM data. However, it has since been applied to atom probe specimens to characterise the nature and location of grain and low-angle boundaries (Babinsky *et al.* 2014, Piazolo *et al.* 2016, Reddy *et al.* 2016, Rice *et al.*

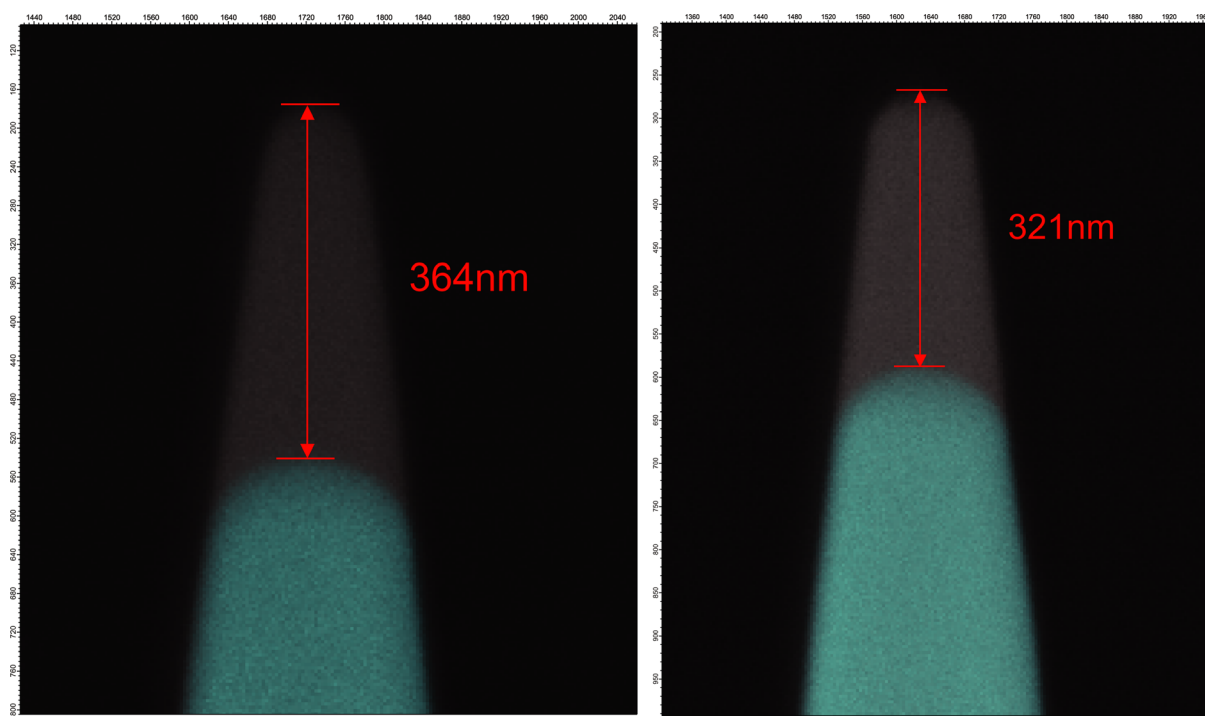


Figure 15. Electron images of two atom probe specimens of zircon showing tip shape before and after analysis and the amount of material removed during each analysis. The amount of removed material constrains the evaporation field and atomic volume for better zircon reconstructions (from Saxey et al. 2019).

2016), phase boundaries (Montalvo et al. 2019) and crystallographic information (Breen et al. 2017). An advantage of this approach is that once the region of interest has been located in the atom probe specimen, then the specimen can be re-milled to ensure that the feature is close to the tip of the specimen. This is particularly useful for materials that tend to rupture easily, where large data sets are difficult to obtain.

High-resolution imaging of the specimen can also be conducted using TEM. In addition to imaging the shape and internal microstructure of the needle, TEM can perform crystallographic analyses (via electron diffraction and lattice imaging) and 3D analysis by electron tomography. Compositional analyses can also be performed in the TEM. Transmission EDS with ≤ 10 nm lateral resolution can provide major element compositional information. Electron energy loss spectroscopy can be used to analyse low atomic number elements and chemical bonding states. These analytical techniques within a TEM can be used to assist in the recognition of potentially interfering peaks in the atom probe mass spectra, as well as providing some insight into the expected compositional variation in the needle, which can assist in the selection of appropriate acquisition parameters (Guo et al. 2016, Kelly 2017).

Electron tomography by TEM and STEM (Kübel et al. 2005) also provides new opportunities for better reconstruction parameters. Cross-correlating electron tomography results with atom probe analyses has been shown to ensure the better specimen radius, shank angle, and z-direction scaling of atom probe reconstructions (Arslan et al. 2008, Gorman et al. 2008, Schreiber et al. 2013) (Figure 16). In addition, and in a similar way to the SEM, TEM can be performed after APT analysis on analysed specimens to measure the amount of material that has been removed during the atom probe analysis and determine reconstruction parameters. Future developments in the integration of APT with (S)TEM within a single instrument (e.g., Gorman et al. 2011) has even greater potential to radically improve the reconstruction of atom probe data (Kelly 2017).

Geoscience applications

This section aims to provide an overview of the published APT literature in the geoscience field. Conference abstracts, due to their succinct nature and absence of peer review, were not included in this section. Although in its early stages in the geoscience discipline, the number of publications is rapidly increasing (Figure 2). The

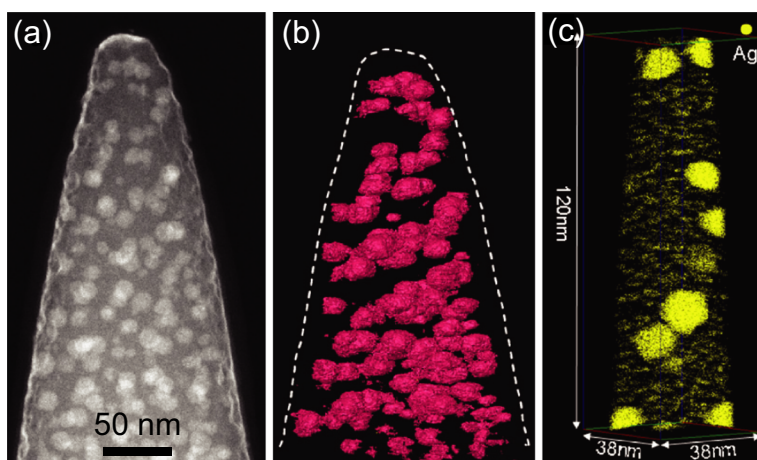


Figure 16. An example of correlative TEM and APT analysis. (a) 2D TEM micrograph of an APT needle containing Ag-rich clusters. (b) Tomographic TEM image of the same volume as (a). White box shows approximate location of APT analysis in (c). (c) APT reconstruction of the same specimen. Refer to Arslan *et al.* (2008) for details. Reprinted from *Ultramicroscopy*, volume 108(12), 1579–1585, Arslan *et al.*, Towards better 3-D reconstructions by combining electron tomography and atom-probe tomography © 2008, with permission from Elsevier.

contributions, as well as the material studied and acquisition variables, are compiled in Table 2 and Appendix S1.

Given the non-conductive nature of most minerals, there are few published studies of geological materials prior to the commercial development of laser-assisted APT around 2005 (Kelly *et al.* 2004). The earliest geoscience studies used voltage-pulsed atom probe field ion microscopy to analyse metallic meteoritic samples and discovered 20 nm diameter, Ni-rich precipitates in low-Ni taenite (Miller and Russell 1992). Early field ion microscopy and voltage-pulsed atom probe analysis of FIB-prepared granulite-facies magnetite (Kuhlman *et al.* 2001) suffered from repeated failures and low total ion counts (~ 2500 ions), but was still able to identify precipitates of Mn and Al in the magnetite. This study illustrated the future potential for atom probe analysis of geological materials, and biological magnetite containing nanoscale organic fibres and co-located Mg and Na, was one of the first minerals to be analysed by laser-assisted APT (Gordon and Joester 2011).

Despite the potential difficulties with the preparation of atom probe analysis of biomaterials (Grandfield and Engqvist 2012), some of the earliest uses of laser-assisted APT were on biogenic and hydroxyapatite, a common biomineral and a major constituent of bones and teeth (Gordon *et al.* 2012, 2015, La Fontaine *et al.* 2016, Langelier *et al.* 2016). These studies focussed on establishing the nanoscale compositional heterogeneity associated

with the growth and trace element segregation associated with organic–inorganic interfaces and provided new insights into biogenic growth mechanisms and the processes responsible for dental decay.

Since the development of laser-assisted APT, there has been growing interest in applying nanoscale geochemical characterisation to a broad range of geological materials including glass (Gin *et al.* 2013, Hellmann *et al.* 2015, Gin *et al.* 2017), diamond (Heck *et al.* 2014, Lewis *et al.* 2015, Schirhagl *et al.* 2015, Mukherjee *et al.* 2016), Fe–Ni metal alloys (Einsle *et al.* 2018) and silicides (Gopon *et al.* 2017), platinum-group alloys (Parman *et al.* 2015, Daly *et al.* 2017, 2018), oxides (Bachhav *et al.* 2011, 2013, Fahey *et al.* 2016, Taylor *et al.* 2018, Friedrich *et al.* 2019, Gamal El Dien *et al.* 2019, Genareau *et al.* 2019, Taylor *et al.* 2019), carbonates (Felmy *et al.* 2015, Branson *et al.* 2016, Pérez-Huerta *et al.* 2016, Pérez-Huerta and Laiginhas 2018), sulfides (Fougerouse *et al.* 2016, Dubosq *et al.* 2019, Fougerouse *et al.* 2019, Gopon *et al.* 2019, Wu *et al.* 2019), sulfates (Weber *et al.* 2016), zeolites (Schmidt *et al.* 2019) and rock-forming silicates, such as feldspars (White *et al.* 2018c, Cao *et al.* 2019) and olivine (Bloch *et al.* 2019, Cukjati *et al.* 2019, Figure 17). However, a high proportion of the published APT work to date has focussed on trace element mobility, particularly Pb, in accessory minerals.

The pioneering work in this area looked at one of the oldest zircons on Earth and showed that concordant U–Pb

Table 2.
Compilation of APT acquisition parameters for geological materials published to the end of 2019

Mineral group	Mineral	Laser energy (pJ)	Base T (K)	Detection rate (%)	Recommendation (LE (pJ); BT (K); DR (%))	Reference
Silicates and silicides	Zircon	25–700	30–60	0.5–2	[400; 60; –] ^a ; [100–300; 40–50; 0.5–1] ^b	Valley <i>et al.</i> (2014, 2015), Piazolo <i>et al.</i> (2016), Peterman <i>et al.</i> (2016), Reddy <i>et al.</i> (2016), La Fontaine <i>et al.</i> (2017) ^a , Piazolo <i>et al.</i> (2017), Blum <i>et al.</i> (2018), Saxe <i>et al.</i> (2018) ^b , Exertier <i>et al.</i> (2018) Kirkland <i>et al.</i> (2018)
	Titanite	300	60	0.8–1		
	Feldspar	100–500	55–60	1		White <i>et al.</i> (2018a), Cao <i>et al.</i> (2019)
	Olivine	5–200	40–55	1		Bloch <i>et al.</i> (2019), Cukjati <i>et al.</i> (2019)
	Pyroxene	5–50	40	1		Cukjati <i>et al.</i> (2019)
Oxides	Fe-Si grains	30–40	30	0.2–0.6		Gopon <i>et al.</i> (2017)
	Magnetite	20% (Voltage pulse); 40–75	40–60	0.25–0.5		Kuhlman <i>et al.</i> (2001), Gordon and Joester (2011)
	Baddeleyite	50–600	30–50	0.5–3		White <i>et al.</i> (2017, 2018a, 2019), Reinhard <i>et al.</i> (2018)
	Haematite	40	40	0.3–0.5		Taylor <i>et al.</i> (2018)
	Goethite	40–100	30–60	0.2–2		Taylor <i>et al.</i> (2019), Friedrich <i>et al.</i> (2019)
Phosphates	Rutile	30–90	50–60	0.6–4.5	30–50; 50; 0.8 ^c	Verberne <i>et al.</i> (2019) ^c
	Spinel	150	60	1		Gamal El Dien <i>et al.</i> (2019)
	Titanomagnetite	30–60	50	0.5		Genareau <i>et al.</i> (2019)
	Apatite	16–150	40–50	0.25–0.5		Gordon <i>et al.</i> (2012, 2015), La Fontaine <i>et al.</i> (2016), Langelier <i>et al.</i> (2017)
	Monazite	100	50	1		Fougerouse <i>et al.</i> (2018), Seydoux-Guillaume <i>et al.</i> (2019)
Carbonates	Magnesite	20	40	0.3		Felmy <i>et al.</i> (2015)
	Calcite	50–1300	40–50	0.2–2		Perez-Huerta <i>et al.</i> (2016), Branson <i>et al.</i> (2016), Perez-Huerta and Laigindas (2018)
	Dolomite	300	50	2		Perez-Huerta <i>et al.</i> (2016)
Sulfides and sulfates	Arsenopyrite	45–50	55	1		Fougerouse <i>et al.</i> (2016)
	Pyrite	30–50	50–60	0.8–1		Fougerouse <i>et al.</i> (2019), Wu <i>et al.</i> (2019), Dubosq <i>et al.</i> (2019), Gopon <i>et al.</i> (2019)
	Pyrrhotite	10	30	1		Fougerouse <i>et al.</i> (2019)
	Barite	40–55	50	0.5		Weber <i>et al.</i> (2016)
Native elements and metal alloys	Diamond	20–1000	80–110	0.5–3		Heck <i>et al.</i> (2014), Lewis <i>et al.</i> (2015), Schirhagl <i>et al.</i> (2015), Mukherjee <i>et al.</i> (2016)
	Isoferroplatinum	120–275	–	1–3.		Parman <i>et al.</i> (2015)
	Refractory metal nuggets	250–300	60–80	0.3–0.5		Daly <i>et al.</i> (2017)
	Tetrataenite	400 (532 nm laser)	55	–		Einsle <i>et al.</i> (2018)
	Kamacite – taenite	20–33	30–35	–		Rout <i>et al.</i> (2017)
Glasses	Os-Re alloys	40–200	60–70	0.5		Daly <i>et al.</i> (2018)
	Silicate glass	50–120; 10000 (340 nm laser)	70	0.02–0.5		Gin <i>et al.</i> (2013, 2017), Hellmann <i>et al.</i> (2015)

^a, ^b, ^c refer to references that give the marked specific recommendations for APT acquisition parameters.

analyses by SIMS were disturbed at the nanoscale, but the disturbance could be temporally constrained through the characterisation of isotopic ratios in different Pb domains (Valley *et al.* 2014, 2015; Figure 18a). A similar study on discrete Pb reservoirs in discordant zircon provided some insights into the mechanisms of Pb segregation and the role of defects in forming discrete Pb isotopic reservoirs (Peterman *et al.* 2016, 2019; Figure 18b). Trace element mobility has been studied in undeformed zircon (Piazolo *et al.* 2017, Peterman *et al.* 2019) and deformed zircon (Piazolo *et al.* 2016, Reddy *et al.* 2016), and similar studies have been undertaken on baddeleyite (White *et al.* 2017, Reinhard *et al.* 2018, White *et al.* 2018a, b), monazite (Fougerouse *et al.* 2018, Seydoux-Guillaume *et al.* 2019), titanite (Kirkland *et al.* 2018) and rutile (Verberne *et al.* 2019).

These above studies illustrated how APT could be applied to specific research problems. However, there is also an underlying need to better understand the systematics of atom probe data acquisition, ranging and reconstruction variables in geological materials and this has led to a number of papers dealing with APT optimisation in accessory phase analysis (La Fontaine *et al.* 2017, Blum *et al.* 2018, Exertier *et al.* 2018, Reinhard *et al.* 2018, Saxe *et al.* 2018b, Verberne *et al.* 2019).

Despite the currently limited number of published geoscience atom probe results, such studies, and the range of applications from the metals, semiconductor and ceramic literature, provide a useful insight into the future potential applications of atom probe studies in the geoscience field. In this section, we summarise the broad range of geoscience applications, and highlight some potential new areas of development related to primary compositional differences and subsequent modification by geological processes taking place at the nanoscale. The aim is to provide a context for what may be achievable and provide a stimulus for researchers to further develop these applications.

Assessment of mineral suitability to APT

There are currently ~5000 known minerals that have a range of different compositions, structure, symmetry and form, as well as different physical, optical (relevant to laser-assisted analyses) and chemical properties. This variability means there is inordinate potential for the development of APT applications in the geoscience field. However, these varying properties also have the potential to affect the ability of specific minerals to be analysed by APT due to difficulties in sample preparation and/or a propensity to rupture in the high electric fields required for field emission. To date,

published atom probe data exist for a limited number of minerals (Figure 17; Table 2) and, in most cases, analysed minerals have tended to have high crystal symmetry and reasonable Mohs' hardness. However, experiments on galena (Pb sulfide) and zinnwaldite (Li-bearing mica) show that APT can also be successfully applied to relatively soft minerals, which in the latter case are also strongly anisotropic, cleaved and has low crystal symmetry (Figure 19). Despite such success, assessment of the crystallographic orientation dependence on atom probe acquisition parameters and yield may be needed in minerals, such as micas, where there is a high degree of crystallographic anisotropy.

Compositional constraints at the nanoscale

In many geological situations, the time-consuming nature of sample preparation, analysis and data processing, plus the relatively low precision of APT with respect to more traditional, larger volume analytical techniques, means that APT is usually not the most suitable approach for bulk geochemical analyses. However, the ability of APT to provide sub-nanometre resolution of major and trace elements, and isotopic compositions, across the whole periodic table, without a priori mass selection, allows previously unobtainable information to be collected and analysed. APT is therefore ideal for determining the bulk composition of natural mineral and metallic grains that are too small to be quantitatively analysed by any other technique. In such cases, the bulk composition may provide some fundamental constraints on outstanding scientific problems.

A recent example of such an approach is the analysis of sub-micrometre meteoritic refractory metal nuggets from a carbonaceous chondrite, which demonstrated the presence of up to 1 at% S and provided direct evidence of metal nugget migration in the protoplanetary nebula (Figure 20; Daly *et al.* 2017). Nanoscale trace element variations in platinum-group alloys have also been identified by APT and this has allowed the discrimination of magmatic versus weathering origins for such particles (Parman *et al.* 2015). Similarly, fine-scale compositional variations formed during mineral growth, and the subsequent modification of such growth profiles at the nanoscale by diffusion (Bloch *et al.* 2019), interface-coupled dissolution–reprecipitation (Peterman *et al.* 2019) or exsolution (Genareau *et al.* 2019), could be measured by APT and have the potential to place valuable constraints on magmatic, metamorphic and ore-related petrogenetic processes (Cao *et al.* 2019, Gamal El Dien *et al.* 2019, Schipper *et al.* 2020).

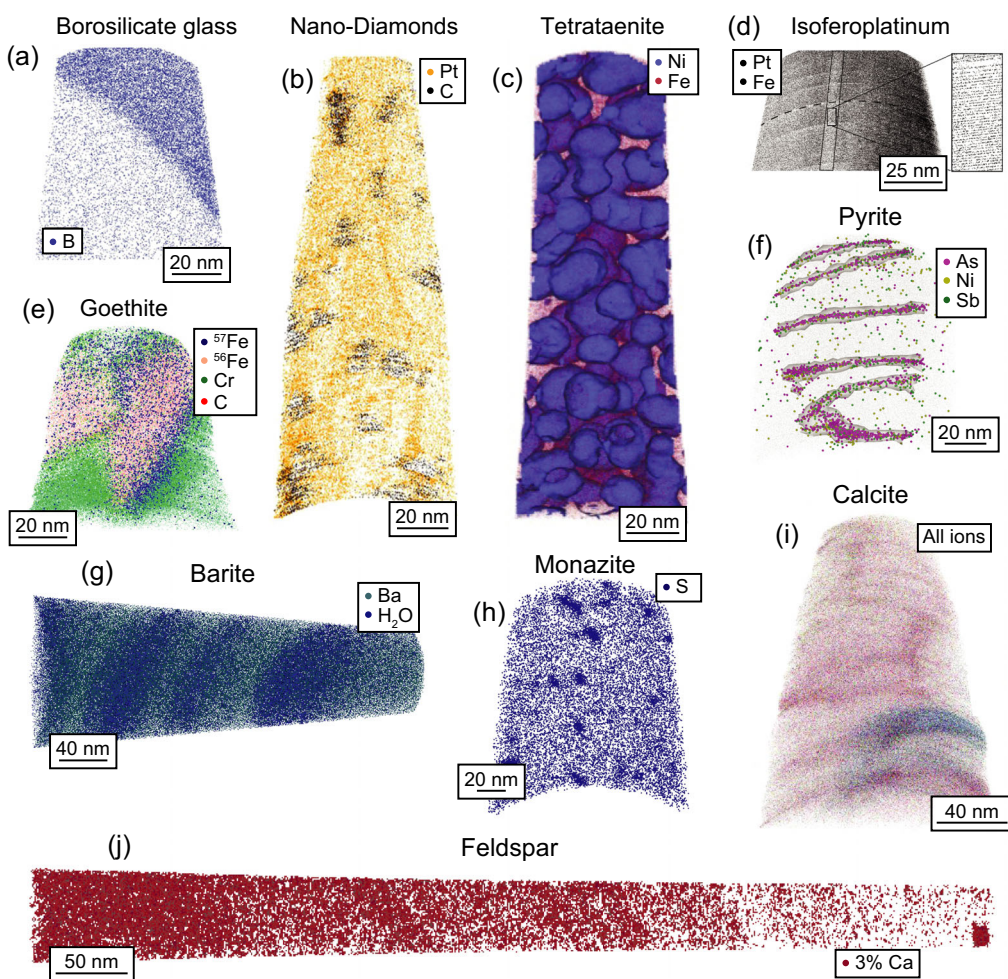


Figure 17. Examples of reconstructed APT data from a range of geological materials. (a) B (blue) distribution from the alteration front of a borosilicate glass (figure 2 of Gin *et al.* 2013); (b) nanodiamonds from the Allende meteorite embedded in platinum. C (black) and Pt (orange) distribution in a 5 nm wide slice through an atom probe specimen (figure 3 of Lewis *et al.* 2015); (c) isolated islands of tetrataenite (FeNi) embedded in Fe metal from the Tazewell IAB sLH iron meteorite. 32.5% Ni isosurface is displayed in blue and Fe atoms in red (Einsle *et al.* 2018); (d) Pt and Fe atoms in isoferroplatinum. The inset is a 5 nm thick and 50 nm tall slice (figure 3 of Parman *et al.* 2015); (e) nanoparticulate goethite encapsulated in Cr (green). The distribution of the isotopic label ^{57}Fe (blue) has been emphasised (Taylor *et al.* 2019); (f) pyrite specimen showing the distribution of As (Purple), Ni (Yellow) and Sb (Green). The trace elements are organised in an array of dislocations (unpublished data set from Fougerouse *et al.* 2019); (g) barite with layering of Ba and H_2O (figure 9C of Weber *et al.* 2016); (h) monazite specimen showing S (blue) exsolution in discrete clusters (Seydoux-Guillaume *et al.* 2019); (i) mineral–organic interface in calcite from mussel shells. The atom map shows all atoms ranged in the data set (Pérez-Huerta and Laiginhas 2018); (j) recrystallised feldspar from meteorite NWA6342. The 3% Ca isoconcentration surface (red) illustrates 10–60 nm thick parallel, compositional features (modified after White *et al.* 2018c). (a) Reprinted from *Chemical Geology*, volume 349, 99–109, Gin *et al.*, Contribution of atom-probe tomography to a better understanding of glass alteration mechanisms: Application to a nuclear glass specimen altered 25 years in a granitic environment © 2013, with permission from Elsevier. (b) Reprinted from *Ultramicroscopy*, volume 159, 248–254, Lewis *et al.*, C 12/C 13 – ratio determination in nanodiamonds by atomprobe tomography © 2015, with permission from Elsevier. (d) Reprinted from *American Mineralogist*, volume 100, 852–860, Parman *et al.* © 2015 with permission from the Mineralogical Society of America. (g) Reprinted from *Chemical Geology*, volume 424, 51–59, Weber *et al.*, Nano-structural features of barite crystals observed by electron microscopy and atom probe tomography © 2016, with permission from Elsevier.

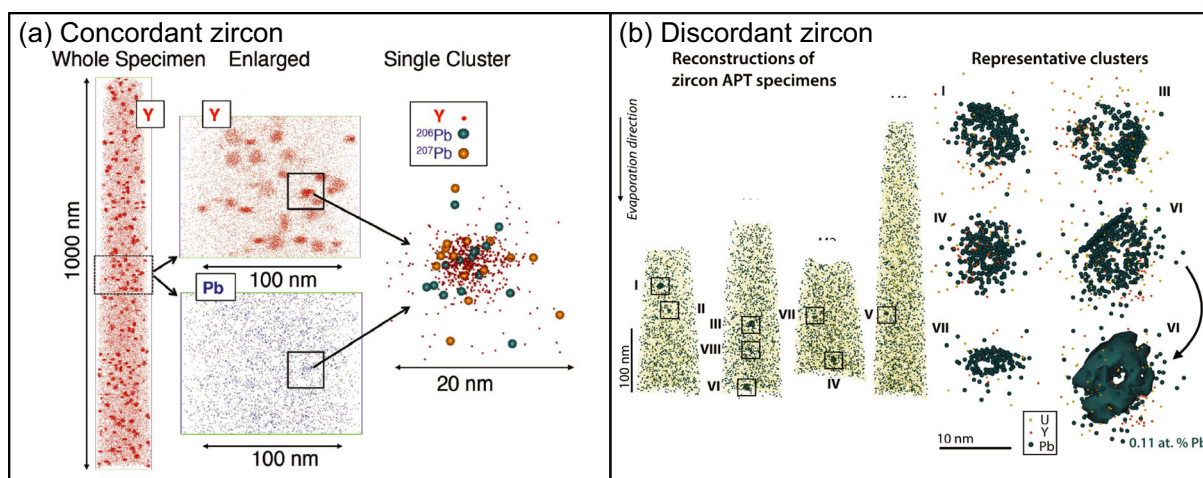


Figure 18. APT data from (a) ‘undisturbed’ Hadean zircon (no Pb loss) where cluster formation in Pb and Y is interpreted to represent the migration of Pb to un-annealed damaged domains (Valley *et al.* 2015) and (b) discordant zircon (Pb loss) where clusters (labelled I–VIII) represent Pb trapped in dislocation loops formed during annealing of radiation damaged zircon (Peterman *et al.* 2016). Coloured spheres represent the position of atoms as determined by APT. (a) Reprinted from *American Mineralogist*, volume 100, 1355–1377, Valley *et al.* © 2015 with permission from the Mineralogical Society of America.

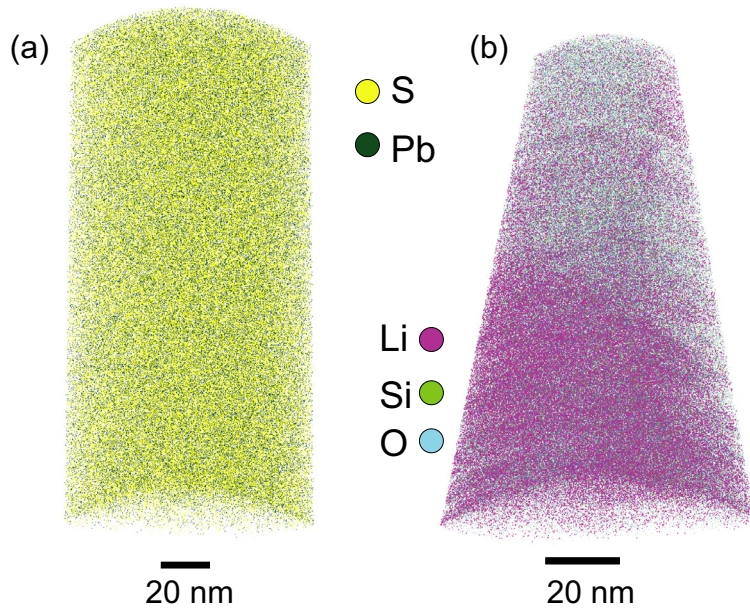


Figure 19. APT reconstructions of low Mohs' hardness scale (~ 2.5) material for (a) galena (PbS) and (b) Li-bearing mica (zinnwaldite; $\text{KLiFeAl}(\text{AlSi}_3)\text{O}_{10}(\text{OH},\text{F})_2$). In (b), the crystallographic *c*-axis lies parallel to the specimen long axis. These data demonstrate the ability for APT to be applied to both soft and anisotropic, low-symmetry minerals. Sample in (b) was provided by M. Aylemore.

Primary metal, mineral and fluid inclusions

APT can place compositional constraints on nanoscale domains, including distinct domains within a single atom

probe specimen. In a study of gold distribution in arsenopyrite, ~ 10 nm gold clusters were interpreted to have developed during growth and form as a function of growth rate and the ability of gold to migrate along the growing arsenopyrite

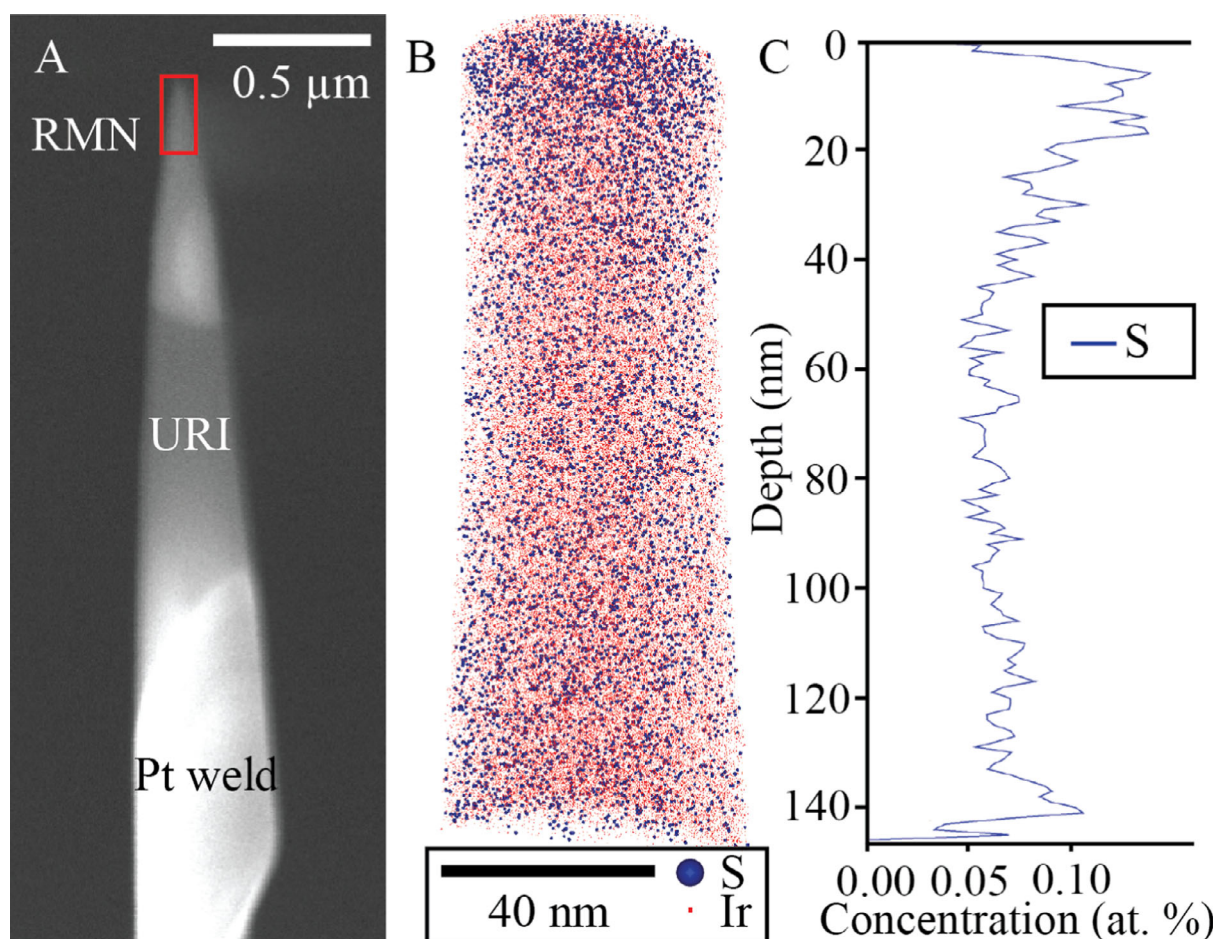


Figure 20. Sulfur analysis from an ~100 nm diameter refractory metal nugget from a chondritic meteorite. The nugget was targeted using backscatter electron imaging and site-specific FIB-SEM extraction. Refer to Daly *et al.* (2017) for details. Figure reprinted from *Geology*, volume 45, 847–850, © 2017 with permission from the Geological Society of America.

surface (Fougerouse *et al.* 2016; Figure 21a). In cases such as this, where compositionally distinct inclusions are present, the reconstruction of spatial relationships is critical. However, these data illustrated potential issues in the reconstruction of such small compositional features because the field required for evaporation differs markedly between the nanoscale inclusion (Figure 11), in this case gold, and the host arsenopyrite matrix (Figure 21a). Similar features have been seen in atom probe studies of synthetic specimens of spherical gold nanoparticles in MgO (Devaraj *et al.* 2014). The alternative scenario of nanoparticles requiring a lower field for evaporation than the host has also been reported for Pb clusters in zircon (Figure 18b; Peterman *et al.* 2016). Such studies serve to illustrate that care should be taken in interpreting reconstructed inclusion morphologies when the field required for evaporation is markedly different between host and inclusion.

The presence and identification of nanoscale inclusions in mineral hosts is known from TEM and other high-spatial-resolution techniques (Champness 1997, Dobrzhinetskaya *et al.* 2006, Lee 2010, Ferraris and Auchterlonie 2013). The advantage of APT is its ability to place compositional constraints on the trace element and isotope geochemistry of the included phase. For example, Ca-rich clusters in monazite (Figure 21b), interpreted to represent inclusions of nanoscale apatite (Fougerouse *et al.* 2018), also contain trace amounts of Si and Pb which is enriched when compared with the host monazite. The apatite inclusions have been interpreted to segregate shortly after monazite growth and they preferentially partition common Pb within the monazite lattice. In this specific example, the amount of common Pb is small. Nevertheless, APT is able to identify nanoscale segregated Pb domains of distinct isotopic

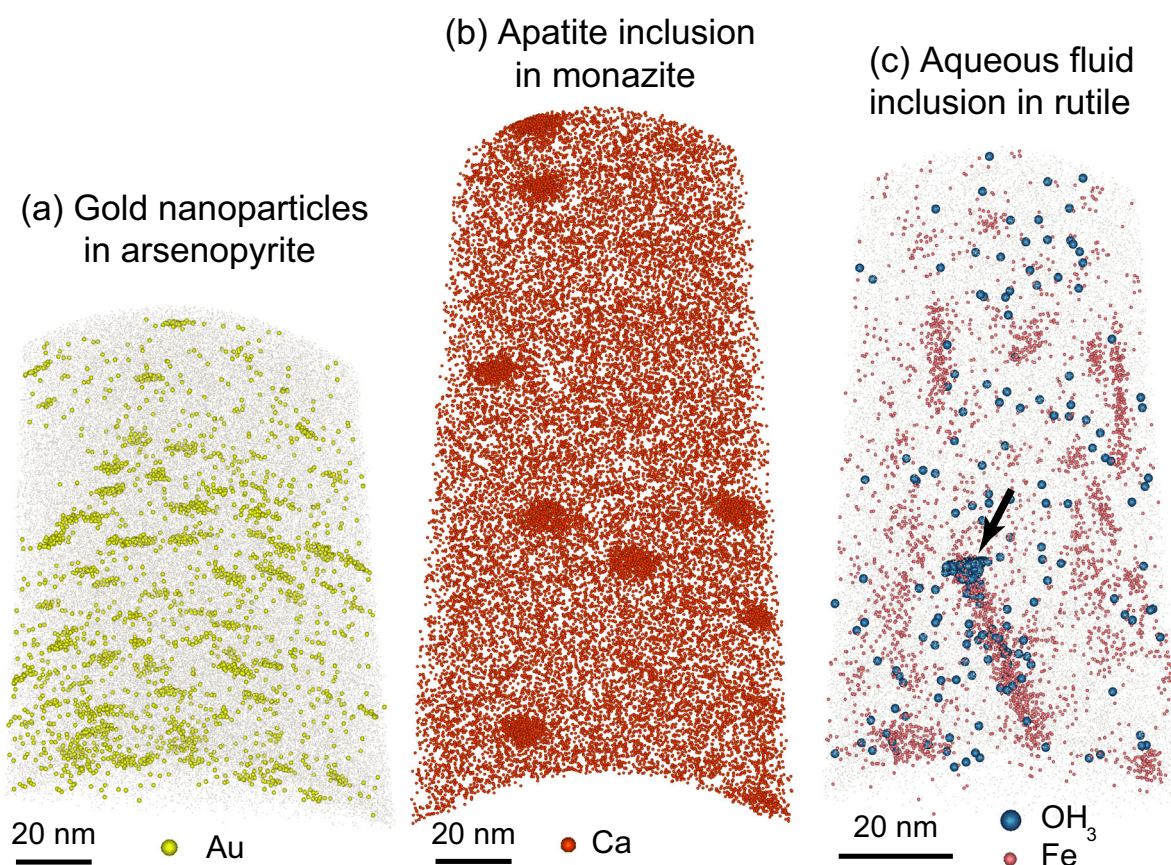


Figure 21. Atom probe reconstructions showing nanoscale compositional features interpreted to have formed during, or slightly after, initial growth of the host mineral. (a) Gold nanoparticles in arsenopyrite (after Fougerouse *et al.* 2016). (b) Exsolved apatite clusters in monazite (after Fougerouse *et al.* 2018). (c) OH₃ molecular species located at the tip of Fe exsolution features in rutile. The composition and evaporation characteristics are consistent with analysis of nanoscale fluid inclusions.

composition (Fougerouse *et al.* 2018, Seydoux-Guillaume *et al.* 2019).

One potential area of future research is in the analysis of nanoscale fluid inclusions within minerals. A likely example is the presence of OH₃ peaks associated with the tips of segregated Fe-rich lamellae in rutile (Figure 21c). In this case, the reconstruction of OH₃ distribution shows an unusual pattern of dispersion that likely represents trajectory aberrations associated with rapid evaporation of the inclusion contents once the inclusion has been breached. This will make the incidental analysis of such features difficult. In addition, the potential for overlapping contaminating peaks (see the section on *Nanoscale stable isotope analysis*) may complicate interpretations. However, specific targeting of such features by careful selection of acquisition parameters may be possible.

Secondary trace element clusters in minerals

Elemental nanoscale clusters in minerals, need not be distinct mineral phases, but may be defined by more subtle trace element compositional variations. In zircon, several studies have reported the presence of clusters of Y, Pb and Al (Valley *et al.* 2014, 2015, Peterman *et al.* 2016, Piazolo *et al.* 2016, Blum *et al.* 2018, Peterman *et al.* 2019). Isolation of these clusters, using 3D volumes defined by isoconcentration surfaces (Hellman *et al.* 2000) or cluster analysis routines (e.g., Stephenson *et al.* 2007, Dong *et al.* 2019), significantly reduces the analytical background and permits quantification of compositional and isotopic analysis of these clusters. $^{207}\text{Pb}/^{206}\text{Pb}$ measurements of clusters in both concordant and discordant zircon (Figure 18) have been shown to be distinct from bulk isotopic compositions outside the cluster and this has allowed the isotopic

compositions of the clusters to be used to constrain the timing of geological events (Valley *et al.* 2014, 2015, Peterman *et al.* 2016).

In the cases of Pb clusters in zircon highlighted above, the mechanisms of cluster formation are reportedly different. The toroidal morphology of some Pb clusters, combined with the $^{207}\text{Pb}/^{206}\text{Pb}$ ratio and timing of cluster formation, have been used to infer that clusters formed by Pb entrapment in dislocation loops generated during thermally driven annealing of radiation damage associated with U decay (Peterman *et al.* 2016, 2019). In contrast, cluster formation in Hadean zircon from Jack Hill's Western Australia, is interpreted to reflect volume diffusion of Pb into non-annealed radiation damaged domains during metamorphic heating (Valley *et al.* 2014, 2015).

Lead clusters have also been found in other minerals and again the mechanisms of cluster formation are notably different. As outlined earlier, Pb associated with nano-inclusions of apatite in monazite (Figure 21b) have been interpreted to reflect partitioning of Pb into apatite during unmixing of phosphate end-member compositions immediately after growth (Fougerouse *et al.* 2018). However, APT and TEM data from high-temperature monazite grains from

Rogaland, Norway, contain CaSO_4 nanoclusters that appear to be linked to Pb mobility associated with cluster formation during a younger, high-temperature metamorphic event (Laurent *et al.* 2016, Seydoux-Guillaume *et al.* 2019). Lead clusters in pyrite have also been reported to form at the intersection of deformation-related, non-parallel dislocations (Fougerouse *et al.* 2019).

These studies indicate that cluster formation is not indicative of a single mechanism and the presence of clusters may represent different processes that operate as a response to the intrinsic defect properties of the mineral combined with extrinsic geological conditions. As such, the mechanisms of nanoscale atom-cluster formation in minerals are likely to be complex and reflect a range of processes. However, such clusters represent the nanoscale manifestation of geological processes that may not be recorded at larger scales, and the examination of elemental and isotopic compositions of clusters has the potential to yield valuable information to constrain the nature and timing of poorly recorded geological events.

In the above examples of atom clustering, the recognition of the clusters is easily made by visual inspection of the different elemental species in the reconstructed atom probe

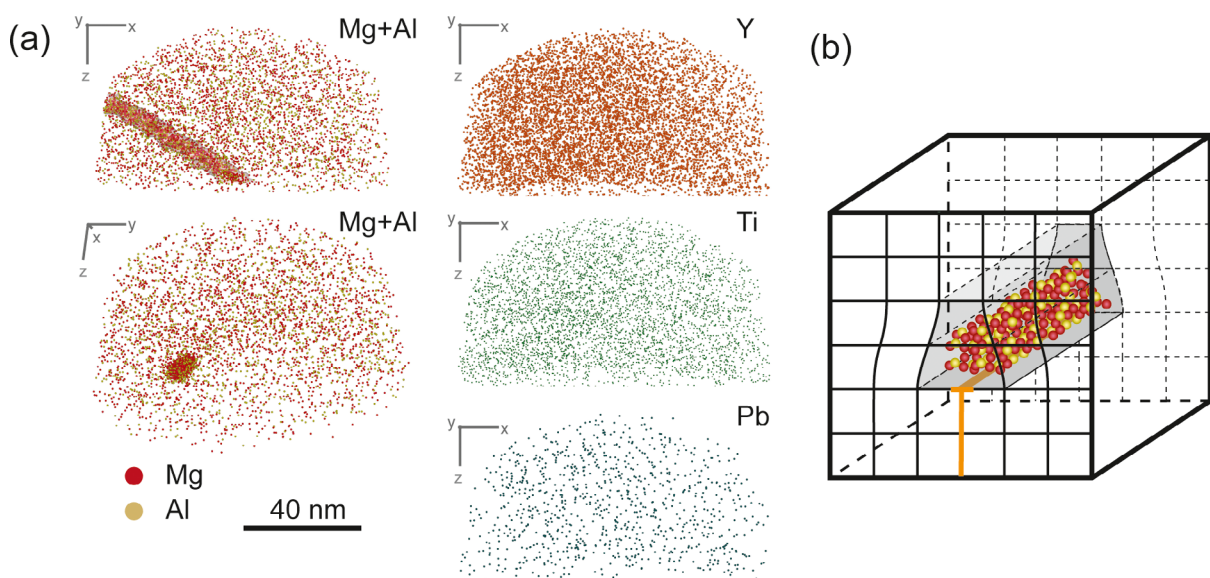


Figure 22. (a) 2D sections of atom probe data from a Palaeoproterozoic zircon showing a single dislocation defined by the segregation of interstitial Mg^{2+} and Al^{3+} ions. Yellow isoconcentration surface in upper left Mg + Al reconstruction represents 0.1 at% Al. No segregation of larger ionic radius trace elements is seen. (b) Schematic model to illustrate the Cottrell atmosphere nature of the segregation. Orange line shows edge dislocation, and black lines represent lattice planes (not to scale). Grey zone represents region of lattice distortion into which interstitial cations (Mg and Al) may segregate. Data collected at Cameca, Madison, USA.

data. Once identified, they can be readily analysed. However, in some examples, clusters may be subtle and difficult to resolve visually. It is therefore worth noting that there are a number of methods to establish the presence, composition and characteristics of atom clusters within atom probe data, even when such clusters are visually cryptic (Hyde and English 2001, Vaumousse *et al.* 2003, Stephenson *et al.* 2007, Hyde *et al.* 2009, Philippe *et al.* 2009, Marquis and Hyde 2010, Zelenty *et al.* 2017).

Mineral defects

The lattices of minerals contain a variety of defects associated with deviations from a periodic arrangement of atoms. These defects may develop both during crystal growth (Klapper 2010) and subsequent deformation and recrystallisation (e.g., Barber *et al.* 2010). They are important because such defects are critical in controlling mineral properties, behaviour, and the mechanisms of intracrystalline element mobility, and there is a clear and important link between incompatible trace element distribution and the formation and evolution of mineral defects (Buseck and Veblen 1978, Argunova *et al.* 2003, Zhang *et al.* 2010, Camacho *et al.* 2012, Zhang and Wright 2012, Wu and Buseck 2013). Their significance has meant that defects have been widely studied by high-resolution imaging and analytical techniques such as TEM (Champness 1977, Veblen *et al.* 1993, Lee 2010). Such studies provide valuable constraints on the interaction of mineral defects

and major element geochemistry. However, the link between defects and trace element geochemistry and the temporal evolution of defect–mineral interactions has been difficult to constrain by TEM. The materials science and semiconductor literature has shown that the detailed interaction of defects and trace element distributions can be successfully studied by APT (Miller 2006, Thompson *et al.* 2007a, Marquis and Hyde 2010, Smith *et al.* 2013), and a growing number of atom probe studies are providing valuable constraints on defect–geochemistry relationships within minerals.

Point defects: Atom probe tomography has been used to show that the stoichiometric change from Cu(In,Ge)Se₂ to an ordered vacancy compound phase represents the presence of ordered defect pairs, from which point defect distributions can be calculated (Stokes *et al.* 2016). In the field of minerals research, as yet there are no examples of atom probe data constraining the distribution of point defects at this scale. Individual vacancies are impossible to image because detector efficiencies mean that only 35–50% of all atoms are measured in reflectron-based atom probe systems. Point defects associated with interstitial solute ions generally have low concentrations in minerals so there is always uncertainty as to whether the position of individual ions represents a real part of the signal or a background component. Identifying individual point defects in minerals is therefore untenable with the currently available atom probe technology. However, point defect type and distribution have the potential to be imaged with future developments in

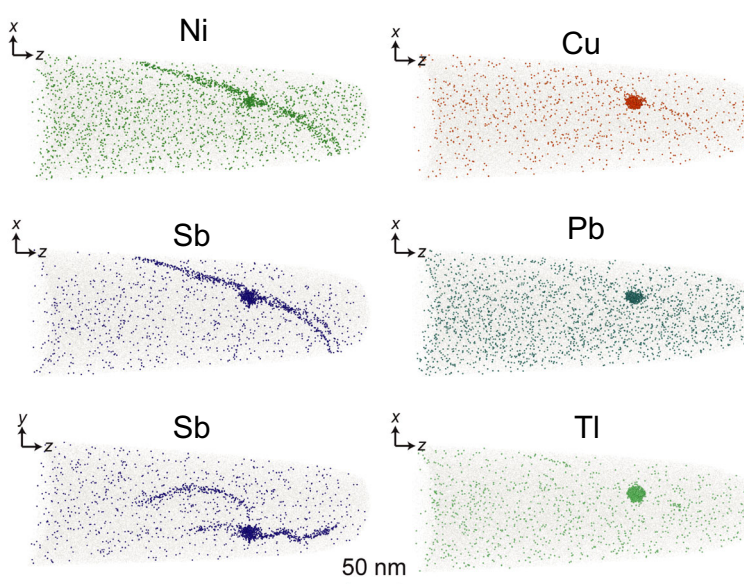


Figure 23. Atom probe reconstructions of specimen of Witwatersrand pyrite showing intersecting dislocations and clustering. Dislocations are clearly seen in Ni and Sb data, whereas Cu, Pb and Ti are more segregated at the point of dislocation intersection. Figure modified after Fougerouse *et al.* (2019).

detector efficiency and reconstruction methodologies (Beinke *et al.* 2016, Kelly 2017). Significantly, interstitial solute ions commonly segregate to areas of mineral lattice distortion to minimise free energy and the concentration and spatial distribution of these atoms in line defects and interfaces may then be detected.

Dislocations: There are several examples of dislocations and dislocation arrays being captured within mineralogical atom probe specimens. In zircon, individual dislocations record enrichment in small interstitial elements, for example, Al and Mg, which are localised around the dislocation but have a volume extending many unit cells away from the direct dislocation core (Figure 22). Such a distribution is consistent with the diffusion of interstitial ions into lower energy distorted lattice sites that surround the dislocation. For small, interstitial cations, the ‘Cottrell atmospheres’ around dislocations, theoretically predicted by Cottrell and Bilby (1949), were first imaged 50 years later by atom probe analysis of boron distribution in Fe-Al alloys (Blavette *et al.* 1999). Subsequent work has shown that elemental distributions along individual dislocations may be heterogeneous, with the formation of precipitates on the dislocation (e.g., Miller 2006). Such features may affect the properties of the host material, but have yet to be observed in minerals. For example, clouds of impurity atoms around line defects may pin the dislocation and reduce strain until a critical de-pinning stress is reached, the Portevin–Le Chatelier effect. Alternatively, dislocation pile-ups at sites of interstitial ion enrichment may rapidly migrate to grain boundaries. Both of these yield periodic stress–strain relationships but have yet to be studied in detail in geological materials.

Arrays of dislocations in tectonically deformed minerals also show co-location of small interstitial ions with substitutional ions such as Y and U (Piazolo *et al.* 2016, Kirkland *et al.* 2018). The cores of these dislocations may behave as fast pathways for element diffusion (e.g., Lee 1995). However, in the case of static dislocations, the bulk diffusion rate depends on the ability of elements to travel to the core region by volume diffusion through the pristine lattice. This dependency may limit the ability of the dislocation core to facilitate fast-path diffusion. However, in mobile dislocations the ability for dislocation cores to collect solute atoms during migration, and carry associated Cottrell atmospheres of interstitial ions, is increased and the efficiency of dislocation-accommodated trace element mobility may be significant. Such a model has been proposed for interstitial trace element enrichment in low-angle boundaries in shocked zircon (Reddy *et al.* 2016).

Atom probe studies on tectonically deformed pyrite have also captured orthogonally intersecting, Ni- and Sb-decorated dislocations that display Pb, Cu and Tl enrichment at the intersection of the dislocation cores (Figure 23; Fougerouze *et al.* 2019). Despite the dislocations being pathways for enhanced Pb mobility, Pb concentrations are still enriched, relative to the matrix, within these dislocations (Figure 23). Although Pb mobility in pyrite is enhanced by transport along dislocation cores, these data indicate that elemental transport in deformed minerals is dependent upon the mechanisms by which different defects interact during the microstructural evolution of the mineral. In this case, the intersection point of the dislocations provides an energetically favourable site for nanoscale segregation of large ions, thereby inhibiting trace element mobility.

Interfaces: The material properties of single crystals differ markedly from those of bulk materials due largely to the presence of interfaces in polycrystalline materials (Sutton and Balluffi 2006). Interfaces are an intrinsic component of all polycrystalline materials and can be considered in two basic forms: interphase boundaries across which there is a change in chemistry or structure, and grain boundaries where there are only orientation variations across the interface. Such interfaces are important because of their ability to interact with other defect types (Priester 2001, Beyerlein *et al.* 2015), provide rapid pathways for material diffusion and enable the localised segregation of solute atoms, which will affect the structure and energy of boundaries and thus their behaviour (Pang and Wynblatt 2006). Consequently, interfaces play a fundamental role in controlling material properties of polycrystalline aggregates, as well as deformation characteristics and the microstructural stability of the host material (Sutton and Balluffi 2006).

Research on interfaces has historically focussed on metals and ceramics (e.g., Sakuma *et al.* 1997, Lejček 2010), and although there are many aspects to interface research, a critical aspect deals with the interface segregation of solute atoms and how this may affect the properties of the bulk material. Fundamentally, elements that are less soluble in the mineral host will tend to segregate to boundary interfaces, leading to a general decrease in grain boundary energy. However, element solubility in minerals, and therefore segregation to interfaces, is temperature-dependent and a number of other factors can influence the degree of segregation. For example, a positive correlation between cross-boundary disorientation and the degree of segregation, except at specific coincident site lattice arrangements, supports a coupled relationship between segregation and boundary dislocation density (Watanabe

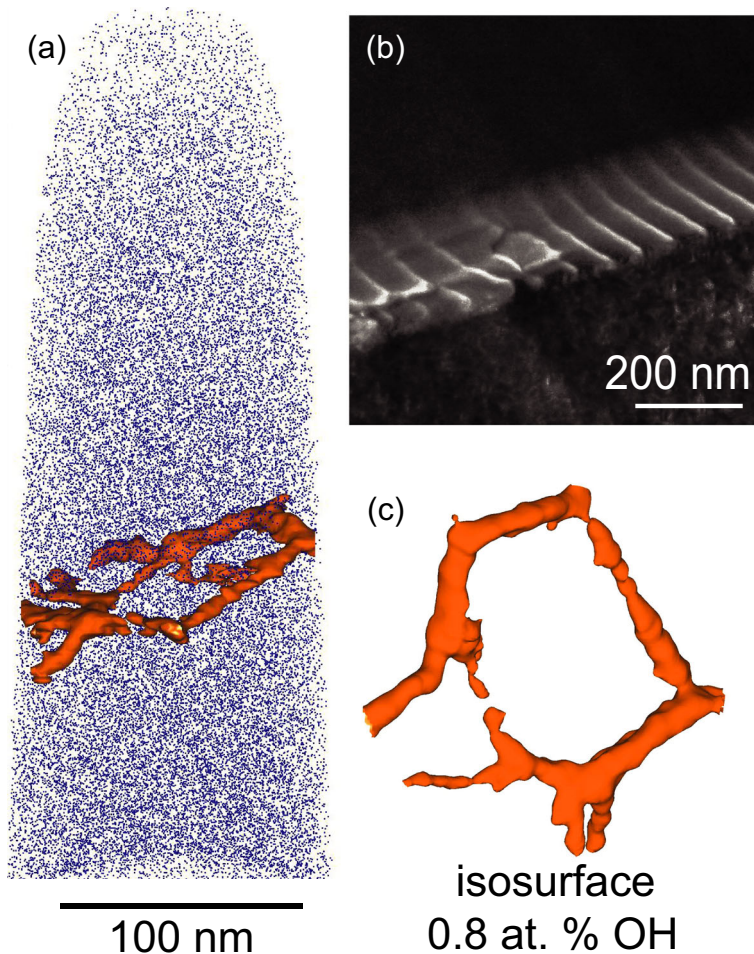


Figure 24. Correlative APT and TEM microscopy of a twin boundary in rutile. (a) APT reconstruction of rutile with a 0.8 at. % OH isoconcentration surface located at the twin interface. The isoconcentration surface shows the region enriched in trace elements. **(b)** TEM HAADF image of the twin boundary in rutile showing dislocations along the twin interface. **(c)** Isoconcentration surface viewed perpendicular to the twin plane. The shape of the polygon formed by dislocation in the top image is similar to that defined by the isoconcentration surface.

et al. 1978, Watanabe 1985). Such correlations indicate that the segregation of trace elements to mineral–mineral interfaces will be heterogeneous and dependent both on boundary geometry and on crystallographic relationships (Marquardt and Faul 2018).

In recent years, atom probe research into interfaces has focussed on simple metal and ceramic systems, with the aim of understanding the mechanisms of element segregation into interfaces and how this can be engineered to develop advanced materials (Raabe *et al.* 2014). Much of this work has been empirically driven through the use of auger imaging and high-resolution TEM. In contrast, the geoscience field has seen few nanoscale geochemical studies of interfaces, and therefore, our understanding of the role of

interface segregation in controlling the material properties of rocks is far less known.

The crystallographically simplest form of mineral interfaces is twin boundaries. Correlative APT and TEM analysis of a twin boundary in rutile has revealed coincidence of linear segregations of trace elements with systematically ordered dislocations (Figure 24). However, most studies that have taken place in geological systems have largely focussed on grain boundaries in olivine-dominated rocks (see recent review by Marquardt and Faul (2018)) and it has been known for some time that the interfaces between olivine grains can be enriched in incompatible trace elements (Hiraga *et al.* 2003, 2004). Similar results have been obtained by APT analyses. Yet in this case, there is a clear

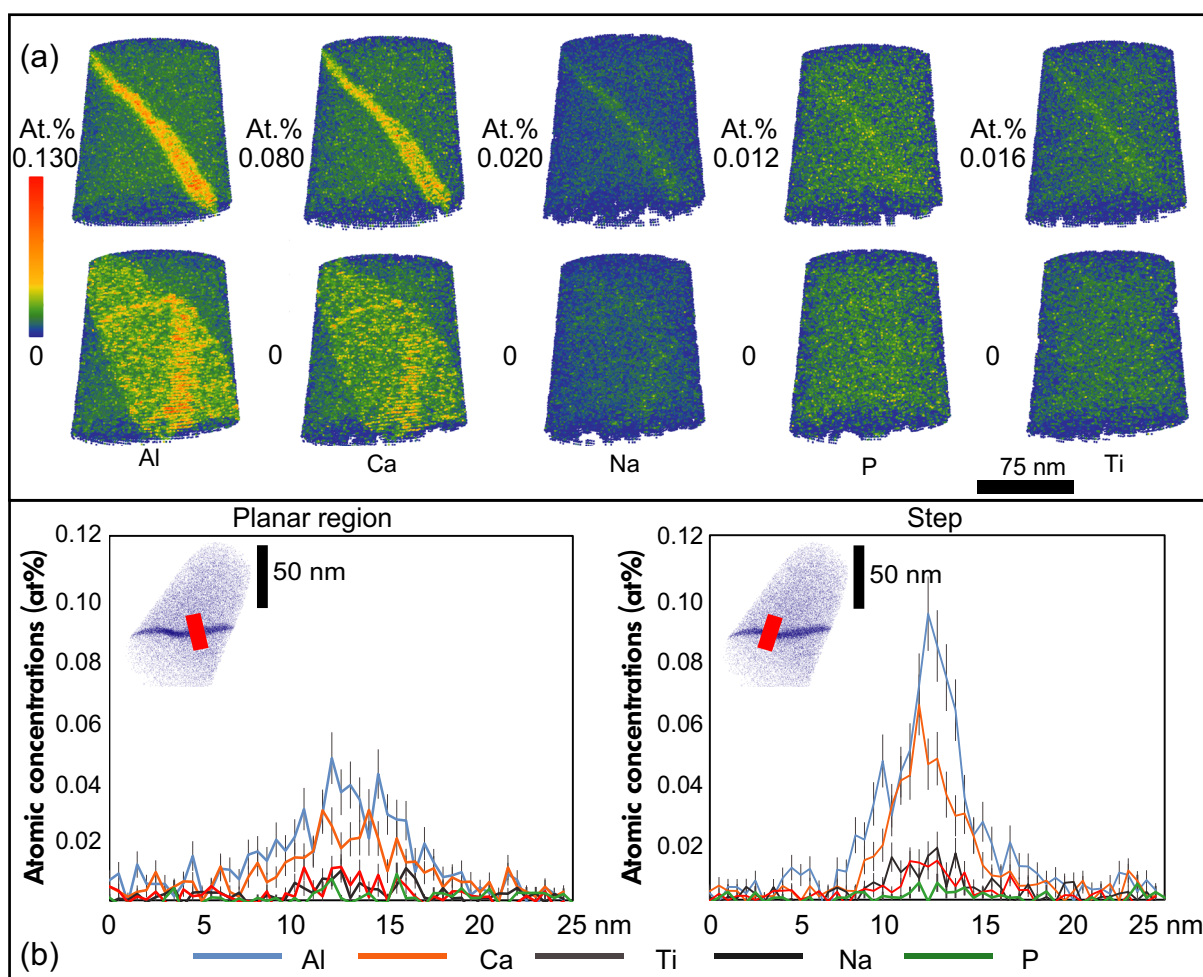


Figure 25. Atom probe data across a low-angle boundary in olivine. The boundary shows two different interface orientations (planar region and step). (a) Atom probe reconstructions showing at% concentration variations in trace elements. (b) 1D compositional profiles across the planar and stepped regions of the interface, showing trace element variations associated with boundary geometry. Figure courtesy of Sam Bain.

distinction in interface composition dependent on the orientation of the interface (Figure 25), a feature that is recognised in interface complexions in manufactured materials (e.g., Cantwell *et al.* 2014). Additional studies on low-angle boundaries in zircon (Piazolo *et al.* 2016, Reddy *et al.* 2016), titanite (Kirkland *et al.* 2018) and baddeleyite (White *et al.* 2017, 2018b) have all documented the interfacial segregation of incompatible trace elements.

Within polymimetic rocks, there are a range of possible interfaces and each of these have a dramatic effect on the properties of the rock or mineral in which they are found. There has been increasing interest in the nature of mineral–fluid interfaces, which are broadly responsible for weathering and mineral dissolution at Earth’s surface (e.g., Lütge and Arvidson 2008) and interface-coupled dissolution–precipitation and

metamorphic reaction under hydrothermal conditions (Borg *et al.* 2014). However, currently there are few atom probe studies of phase boundaries in geological materials. Two notable examples include the trace element analysis of experimentally produced olivine–clinopyroxene phase boundaries (Cukjati *et al.* 2019) and trace element segregation to the shock-induced, polymorphic interface between zircon and reidite (Montalvo *et al.* 2019). In the latter case, the observed trace element enrichment is interpreted to be related to interface formation and requires a modification of the existing martensitic transformation model for the shock metamorphic transformation of zircon to reidite (Figure 26; Montalvo *et al.* 2019).

Such studies show that atom probe analysis of mineral–mineral interfaces has the potential to yield fundamental new insights into both interphase and grain boundary types,

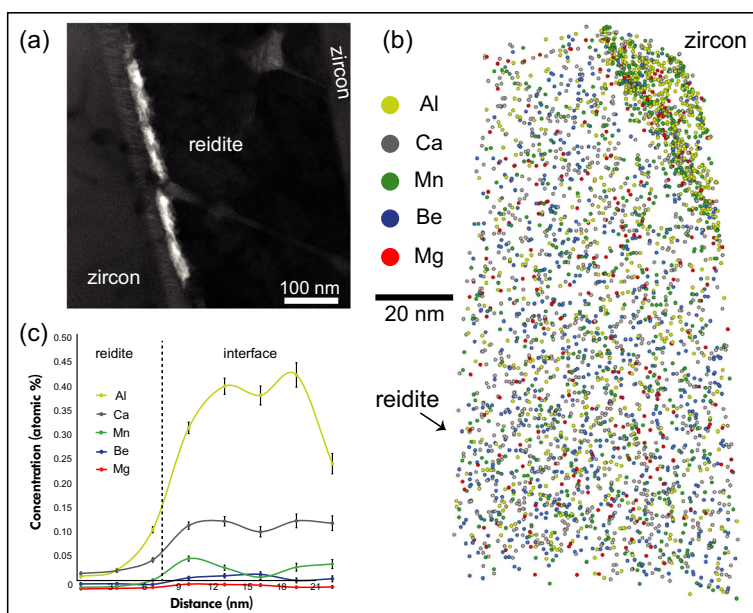


Figure 26. Example of trace element enrichment along the interface between zircon and its high-pressure polymorph, reidite. (a) TEM image of the interface region. (b) Atom probe reconstruction showing trace element enrichment at the zircon–reidite interface. (c) Isoconcentration profile to show the concentration of trace elements at the interface. For details, refer to Montalvo *et al.* (2019). Reprinted from *Chemical Geology*, volume 507, 85–95, Montalvo *et al.*, Nanoscale constraints on the shock-induced transformation of zircon to reidite © 2019, with permission from Elsevier.

and it is anticipated that this research area will be an important component of atom probe investigations in future years. The recent recognition of thermodynamically stable, interface-localised phases, referred to as complexions (Dillon *et al.* 2007, Cantwell *et al.* 2014), that can change discontinuously as thermodynamic conditions change provides further impetus for studying elemental segregation along geologic interfaces (e.g., Harmer 2011).

Nanoscale stable isotope analysis

The bulk trace element characterisation of atom probe specimens has the potential to yield valuable geochemical information. However, isotopic analysis by APT has arguably greater potential in investigating the geological processes responsible for the nanoscale variations that occur through natural and anthropogenic processes and which modify stable and radiogenic isotopic compositions. Isotopic analysis by atom probe is a relatively recent development, which has received only minor interest from the atom probe community, because isotopic ratios have not been particularly important in most material science applications. However, a small number of studies on experimentally perturbed isotopic compositions have demonstrated the potential for APT to be a valuable tool for nanoscale isotopic

measurements. These materials science studies include stable isotopic characterisation of both anions and cations and include C (Thuvander *et al.* 2011), O (Kinno *et al.* 2014), S (Gopon *et al.* 2019), N (Kinno *et al.* 2015), Si (Shimizu *et al.* 2009), Fe (Taylor *et al.* 2018, Frierdich *et al.* 2019), Zn (Ironside *et al.* 2017) and Ge (Shimizu *et al.* 2013). The sensitivity of isotopic analysis at nanometre scales is fundamentally limited by the number of atoms available within a small analytical volume (Figure 1). For spherical volumes around 100 nm in size, which can be accommodated within a typical APT reconstruction, isotopic sensitivities of 1 per mille may be achieved for elements present at 1–5% concentration.

The few published APT studies on the isotopic analysis of minerals have focussed on the stable isotope composition of $^{12}\text{C}/^{13}\text{C}$ ratios in synthetic (Nishikawa *et al.* 1998, Schirhagl *et al.* 2015) and meteoritic nanodiamonds (Heck *et al.* 2014, Lewis *et al.* 2015). However, there is considerable potential for atom probe analysis of stable isotopes, particularly at the low-mass end of the periodic table, for example, lithium and boron, where there are few interfering mass peaks and the isotopic fractionations caused by geological processes can be large. However, the APT analysis of many stable isotopes remains problematic. For

example, the atom probe can potentially discriminate between singly charged hydrogen and deuterium peaks, which opens up the possibility of deuterium-doped experiments to look at hydrogen distribution (e.g., Chen *et al.* 2017). However, the potential for D⁺ and H₂⁺ interferences, plus the current inability to completely remove H ions from the analysis chamber, makes the significance of any H data from geological materials difficult to unravel. Similarly, molecular species ¹⁶OH⁺ and ¹⁷OH⁺ potentially overlap with ¹⁷O⁺ and ¹⁸O⁺, respectively, while ³²O₂²⁺ dimers overlapping with ¹⁶O⁺ at 16 Daltons have the potential to compromise stoichiometric calculations of O-bearing minerals (Bachhav *et al.* 2013). A similar problem may also arise in the analysis of sulfur, though a recent study, modelling the deconvolution of S₂ peaks to eliminate the interference problem, appears promising (Gopon *et al.* 2019). Future developments in atom probe technology to increase detector efficiency, provide energy-sensitive detectors and improved mass resolution, and inhibit chamber-sourced H (Kelly 2017), will significantly improve stable isotope quantification.

Nanoscale geochronology

The decay of the radioactive elements (e.g., U and Th) stored in minerals to stable daughter isotopes provides the means of dating geological events. The current state-of-the-art methods for isotope analysis require minerals that are at least several micrometres in diameter. Some minerals of interest for geochronological dating may be smaller than this. In addition, features of interest within minerals, for example, deformation interfaces, may be below the spatial resolution of conventional methods. Hence, the development of APT to be able to quantify nanoscale isotopic compositions has the potential to provide new temporal constraints on materials that have eluded analysis by other techniques.

A fundamental assumption in radiometric dating is that the original parent isotope and the radiogenic daughter isotope remain captured, and coupled, within the analysed volume of material. Although this may be the case in some situations, it is often apparent, through isotopic discordance and techniques such as scanning ion imaging, that the isotopic parent and/or daughter have been disturbed (e.g., Mezger and Krogstad 1997, Bellucci *et al.* 2016). Understanding this disturbance and the mechanisms by which different elements may migrate in different minerals is critical to correctly interpreting the ages that are extracted from minerals.

The atom probe provides a unique tool for investigating the nanoscale isotopic composition of minerals.

Benchmarking of atom probe analysis of U isotopes in certified U₃O₈ reference materials has shown that major isotopic ratios agree with known compositional values (Fahey *et al.* 2016) and there are comparative thermal ion mass spectrometry (TIMS) and atom probe studies that show that Re-Os analysis by atom probe may yield similar, though less precise, ages to more traditional TIMS analyses (Daly *et al.* 2018). A number of studies have also investigated the mechanisms that can affect the distribution of radiogenic ²⁰⁷Pb/²⁰⁶Pb ratios in zircon (Figure 18; Valley *et al.* 2014, 2015, Peterman *et al.* 2016, Blum *et al.* 2018), baddeleyite (White *et al.* 2017, Moser *et al.* 2019) and monazite (Fougerouse *et al.* 2018, Seydoux-Guillaume *et al.* 2019). The nanoscale distribution of common Pb associated with deformation-related defects has also been studied in titanite (Kirkland *et al.* 2018) and pyrite (Fougerouse *et al.* 2019). Such data provide a means of placing temporal constraints on enigmatic thermal and fluid-flow events. Increased sensitivity and better isotope analysis protocols will increase the opportunity for robust nanogeochronology studies in the future.

Technique limitations, analysis artefacts and potential solutions

The recent application of APT to a broad range of geological materials (Appendix S1) clearly shows the immense potential of the technique to provide nanoscale elemental and isotopic information and yield constraints on a range of geochemical processes. However, the technique has some limitations that users should be aware of. From a practical point of view, site-specific targeting of atom probe specimens requires a comprehensive workflow of correlative analytical techniques that is both time-consuming and analytically expensive. The preparation of needle-shaped specimens with a FIB-SEM is also time-consuming. These workflow and specimen preparation requirements mean that access to a broad range of analytical techniques is a prerequisite for APT. Much of the characterisation workflow can be undertaken at remote sites and there is no need for co-location of the required characterisation equipment with the atom probe facility. However, once atom probe specimens have been manufactured, the transportation of delicate specimens should be minimised. It is therefore beneficial to have on-site FIB facilities, as well as in-house TEM and/or TKD capabilities for atom probe specimen characterisation.

Arguably the most significant limitation of APT is related to the low number of atoms that are analysed in APT relative to other analytical techniques, and the associated issues with precision related to counting statistics. Higher precision

necessitates the collection of large data sets, yet this is sometimes difficult due to specimen stability and/or laser interactions during evaporation. Detection limits are typically specimen and element specific because of the way in which different elements are distributed in the specimen. For example, trace element abundances of $10 \mu\text{mol mol}^{-1}$ may be undetectable if homogenously distributed through the specimen, but could be readily analysed if the trace element was segregated into clusters or interfaces. There is usually no way of knowing this *a priori*.

Molecular species in atom probe analyses are commonly observed in a range of covalently or ionically bonded materials, including minerals (Tsong 1984, Liddle *et al.* 1988, Saxe 2011, Schreiber *et al.* 2014, Gault *et al.* 2016). These molecular species can form by the bonding of adsorbed, mobile atoms and a surface atom, or by atoms collocated in the specimen (Gault *et al.* 2012a), and have been suggested to be related to a lower critical electric field at the specimen surface (Müller *et al.* 1965). Hence, the propensity for field evaporation of molecular species is influenced by the specimen base temperature, laser power energy and potential (voltage) applied to the specimen. In laser-pulsed systems, the laser pulse energy is the parameter which is thought to be the most important to reduce the formation of molecular species. However, a recent study on zircon has shown that other parameters can have an effect on molecule formation. For example, a detrimental peak overlap between $\text{Si}_2\text{O}_3^{2+}$ and $^{208}\text{Pb}^{2+}$ in zircon, is minimised at high voltages independently of the laser energy, indicating the importance of the electric field in controlling the formation of molecular species (Saxe *et al.* 2018b).

The field evaporation of molecular species can have a detrimental impact on the quality of the analysis, in particular when two, or more, species have the same mass, isobaric interferences may preclude the precise quantification of both compositions. When an isobaric interference occurs between two species, the mean terrestrial isotopic ratio is commonly used to calculate the proportion of each overlapping species to the total peak counts. Such an approach has been successfully applied to simple isobaric interferences to improve the compositional data of their analyses, for example, $^{27}\text{Al}^+$ and $^{54}\text{Fe}^{2+}$, and $^{56}\text{Fe}^{2+}$ and $^{14}\text{N}_2^+$ (Miller 2000, Dmitrieva *et al.* 2011, Takahashi *et al.* 2011, Gault *et al.* 2012b). With more complex data sets involving multiple peak interferences, peak deconvolution is more difficult, but commercial processing software does include algorithms that attempt to quantify peak counts. However, these do not generally work well with complex spectra acquired from natural geological materials.

Isobaric interferences of molecular species can have an influence on the major and trace element composition of the material analysed, however other artefacts have been suggested to cause stoichiometry issues. Molecular dissociation has been observed in atom probe data using correlation histograms when two species are detected near simultaneously (Saxe 2011). The dissociation of a molecule can create two charged species in the case when the original species is doubly charged, or one charged and one neutral species if the dissociating molecule was singly charged (Karahka and Kreuzer 2015, Gault *et al.* 2016). In the latter case, the neutral element cannot be accelerated by the potential difference and may not be detected. The phenomenon has been suggested to lead to underestimation of some element concentrations. For example, at high laser energy, N composition in GaN may be underestimated due to the formation of neutral N_2 (Saxe 2011). In geological materials, there is typically a lower O composition than would be predicted from mineral stoichiometry and it is notable that molecular dissociation in O-rich phases has been suggested to be related to the possible formation of neutral O_2 during dissociation (Karahka and Kreuzer 2013; 2015; Silaeva *et al.* 2013). It has also been suggested that the temperature increase associated with the interaction between the laser and the atom probe specimen can favour the thermal desorption of neutral gaseous molecules, such as N_2 and O_2 , from the specimen (Riley *et al.* 2012, Devaraj *et al.* 2013, Kirchhofer *et al.* 2014) and this will also potentially affect mineral stoichiometry.

A recurrent isobaric interference, often observed in atom probe data, is the formation of hydride species. Hydrogen can be an inherent component of the analysed specimens, but is also a residual component in the ultra-high vacuum analysis chamber. The gaseous H from the chamber can adsorb on the specimen surface due to the cryogenic temperature at which the specimens are kept during analysis (typically 30 to 70 K). As a result, most analyses have H species peaks in the mass spectra at 1 Dalton (H^+), 2 Daltons (H_2^+ and D^+), and 3 Daltons (H_3^+ and DH^+). One aspect of hydride formation that is important for geoscience applications are hydrides that cause mass interferences that hinder the measurement of isotopic ratios. For example, the measurement of the $^{12}\text{C}/^{13}\text{C}$ ratio in pre-solar diamond is made difficult by the potential overlap between $^{12}\text{CH}^+$ and $^{13}\text{C}^+$ (Heck *et al.* 2014, Lewis *et al.* 2015), while potential formation of $^{16}\text{OH}^+$ and $^{16}\text{OH}_2^+$ can be detrimental to the measurement of the $\delta^{18}\text{O}$ in zircon (Valley *et al.* 2015). Despite these limitations, some studies have successfully analysed the 3D distribution of hydrogen in steels to investigate its role in embrittlement (Takahashi *et al.* 2010, Chen *et al.* 2017). Further development in the reduction

of hydrogen within the analysis chamber, linked with cryogenic atom probe systems and/or barrier coatings on the instrument walls, will potentially allow hydrogen embrittlement to be studied in geological materials.

As already mentioned, another well documented analysis artefact observed in heterogeneous materials is the local magnification effect (Miller and Hetherington 1991, Vurpillot *et al.* 2000a). In a heterogeneous material, the different constituents of the material rarely have the same field evaporation properties. Differences in these properties will induce the preferential evaporation of the low-field constituent relative to the high-field component and create asperities (or topography) at the surface of the specimen (Figure 11). This nanoscale topography will create ion trajectory aberrations in comparison with a smooth surface. Such ion trajectory aberrations are difficult to correct for at the reconstruction stage (e.g., Devaraj *et al.* 2014, Fougerouse *et al.* 2016, Peterman *et al.* 2016) and the shape and chemistry of the feature can be affected by this artefact.

Conclusions and outlook

We have attempted to provide an overview of the APT technique and give the reader an idea of the ways in which it has been employed in the geoscience field. The applications to date have largely focussed on the nanoscale analysis of accessory minerals and these studies have provided a hitherto unimaginable nanoscale visualisation of heterogeneous elemental and isotopic distributions that reflect an aspect of the geological history of the analysed material. Almost every atom probe paper published to date in the geoscience field has provided a new and fundamental insight into the processes by which trace elements may become mobile in geological systems. Such studies underpin our understanding and interpretation of geochemical and geochronological data collected by larger analytical volume techniques. As such, the future development of APT and its application to an increasing number of minerals, from a range of different geological environments, will yield significant advances to major scientific questions.

There is no other technique that allows such high sensitivity at sub-nanometre resolutions and the atom probe is therefore unique in its ability to provide constraints on atomic-scale processes. However, the small analytical volume of the atom probe means that specimens are not representative of the bulk and a critical aspect of atom probe analysis is therefore a comprehensive, analytical workflow that enables site-specific targeting to address specific scientific questions. As such, APT

complements, rather than replaces, existing analytical approaches and it is clear that APT cannot be used in isolation. With this in mind, APT represents a powerful and unique analytical technique that will only develop further by collaboration with existing analytical facilities. We hope that this paper will inspire researchers without atom probe experience to develop these collaborations with the increasing number of atom probe facilities around the world.

Acknowledgements

The Geoscience Atom Probe forms part of the Australian Resource Characterisation Facility (ARCF) and was developed under the auspices of the National Resource Sciences Precinct (NRSP), a collaboration between Curtin University, CSIRO and the University of Western Australia, supported by the Science and Industry Endowment Fund (SIEF RI13-01). DF is supported by Australian Research Council Discovery Early Career Researcher Awards (DE190101307). We gratefully acknowledge the support of Curtin University's Research Office, Faculty of Science and Engineering and John de Laeter Centre. We are grateful for the positive feedback and helpful comments from two anonymous reviewers. We would also like to thank colleagues and friends in the atom probe community for their continued encouragement and support.

References

Alberts D., von Werra L., Oestlund F., Rohner U., Hohl M., Michler J. and Whitby J.A. (2014)

Design and performance of two orthogonal extraction time-of-flight secondary ion mass spectrometers for focused ion beam instruments. *Instrumentation Science and Technology*, 42, 432–445.

Alexander K., Angelini P. and Miller M. (1989)
Precision ion milling of field-ion specimens. *Journal de Physique Colloques*, 50, C8-549–C8-554.

Argunova T.S., Sorokin L.M., Pevzner B.Z., Balitskii V.S., Gannibal M.A., Je J.H., Hwu Y. and Tsai W.-L. (2003)
The influence of defects in the crystal structure on helium diffusion in quartz. *Physics of the Solid State*, 45, 1910–1917.

Arslan I., Marquis E.A., Homer M., Hekmaty M.A. and Bartelt N.C. (2008)
Towards better 3-D reconstructions by combining electron tomography and atom-probe tomography. *Ultramicroscopy*, 108, 1579–1585.

Babinsky K., De Kloe R., Clemens H. and Primig S. (2014)
A novel approach for site-specific atom probe specimen preparation by focused ion beam and transmission electron backscatter diffraction. *Ultramicroscopy*, 144, 9–18.

references

- Bachhav M., Danoix R., Danoix F., Hannoyer B., Ogale S. and Vurpillot F. (2011)**
Investigation of wüstite (Fe_{1-x}O) by femtosecond laser assisted atom probe tomography. *Ultramicroscopy*, 111, 584–588.
- Bachhav M., Danoix F., Hannoyer B., Bassat J.M. and Danoix R. (2013)**
Investigation of O-18 enriched hematite ($\alpha\text{-Fe}_2\text{O}_3$) by laser assisted atom probe tomography. *International Journal of Mass Spectrometry*, 335, 57–60.
- Barber D.J., Wenk H.-R., Hirth G. and Kohlstedt D.L. (2010)**
Dislocations in minerals. In: Hirth J.P. and Kubin L. (eds), *Dislocations in solids Volume 16*. Elsevier (Oxford, UK), 171–232.
- Bas P., Bostel A., Deconihout B. and Blavette D. (1995)**
A general protocol for the reconstruction of 3D atom probe data. *Applied Surface Science*, 87, 298–304.
- Beinke D., Oberdorfer C. and Schmitz G. (2016)**
Towards an accurate volume reconstruction in atom probe tomography. *Ultramicroscopy*, 165, 34–41.
- Bellucci J.J., Whitehouse M.J., Nemchin A.A., Snape J.F., Pidgeon R.T., Grange M., Reddy S.M. and Timms N. (2016)**
A scanning ion imaging investigation into the micron-scale U-Pb systematics in a complex lunar zircon. *Chemical Geology*, 438, 112–122.
- Beyerlein I.J., Demkowicz M.J., Misra A. and Überuaga B.P. (2015)**
Defect-interface interactions. *Progress in Materials Science*, 74, 125–210.
- Blavette D., Sarrau J.M., Bostel A. and Gallot J. (1982)**
Direction et distance d'analyse à la sonde atomique. *Revue de Physique Appliquée*, 17, 435–440.
- Blavette D., Cadel E., Fraczkiewicz A. and Menand A. (1999)**
Three-dimensional atomic-scale imaging of impurity segregation to line defects. *Science*, 286, 2317–2319.
- Bloch E.M., Jollands M.C., Gerstly S.S.A., Bouvier A.-S., Plane F. and Baumgartner L.P. (2019)**
Diffusion of calcium in forsterite and ultra-high resolution of experimental diffusion profiles in minerals using local electrode atom probe tomography. *Geochimica et Cosmochimica Acta*, 265, 1–30.
- Blum I., Cuvilly F. and Lefebvre-Ulrikson W. (2016)**
Atom probe sample preparation. In: Lefebvre-Ulrikson W., Vurpillot F. and Sauvage X. (eds), *Atom probe tomography: Put theory into practice*. Academic Press (London, UK), 97–121.
- Blum T.B., Reinhard D.A., Chen Y., Prosa T.J., Larson D.J. and Valley J.W. (2018)**
Uncertainty and sensitivity analysis for spatial and spectral processing of Pb isotopes in zircon by atom probe tomography. In: Moser D.E., Corfu F., Darling J.R., Reddy S.M. and Tait K. (eds), *Microstructural geochronology*: Planetary records down to atom scale. Wiley (Hoboken, NJ, USA), 327–350.
- Borg S., Liu W., Pearce M., Cleverley J. and MacRae C. (2014)**
Complex mineral zoning patterns caused by ultra-local equilibrium at reaction interfaces. *Geology*, 42, 415–418.
- Branson O., Bonnin E.A., Perea D.E., Spero H.J., Zhu Z., Winters M., Hönnisch B., Russell A.D., Fehrenbacher J.S. and Gagnon A.C. (2016)**
Nanometer-scale chemistry of a calcite biominerilization template: Implications for skeletal composition and nucleation. *Proceedings of the National Academy of Sciences*, 113, 12934–12939.
- Breen A.J., Babinsky K., Day A.C. and Eder K. (2017)**
Correlating atom probe crystallographic measurements with transmission Kikuchi diffraction data. *Microscopy and Microanalysis*, 23, 279–290.
- Buseck P.R. and Veblen D.R. (1978)**
Trace elements, crystal defects and high resolution electron microscopy. *Geochimica et Cosmochimica Acta*, 42, 669–678.
- Camacho A., Lee J.K.W., Gerald J.D.F., Zhao J., Abdu Y.A., Jenkins D.M., Hawthorne F.C., Kyser T.K., Creaser R.A., Armstrong R. and Heaman L. (2012)**
Planar defects as Ar traps in trioctahedral micas A mechanism for increased Ar retentivity in phlogopite. *Earth and Planetary Science Letters*, 341–344, 255–267.
- Cantwell P.R., Tang M., Dillon S.J., Luo J., Rohrer G.S. and Harmer M.P. (2014)**
Grain boundary complexions. *Acta Materialia*, 62, 1–48.
- Cao M., Evans N.J., Reddy S.M., Fougerouse D., Hollings P., Saxe D.W., McInnes B.I.A., Cooke D.R., McDonald B.J. and Qin K. (2019)**
Micro- and nano-scale textural and compositional zonation in plagioclase at the Black Mountain porphyry Cu deposit: Implications for magmatic processes. *American Mineralogist*, 104, 391–402.
- Castaing R. (1960)**
Electron probe microanalysis. In: Marton L. and Marton C. (eds), *Advances in electronics and electron physics* Volume 13. Academic Press (London, UK), 317–386.
- Cerezo A., Godfrey T.J. and Smith G.D.W. (1988)**
Application of a position-sensitive detector to atom probe microanalysis. *Review of Scientific Instruments*, 59, 862–866.
- Cerezo A., Godfrey T.J., Sijbrandij S.J., Smith G.D.W. and Warren P.J. (1998)**
Performance of an energy-compensated three-dimensional atom probe. *Review of Scientific Instruments*, 69, 49–58.



references

- Champness P.E. (1977)**
Transmission electron microscopy in Earth science. *Annual Reviews of Earth and Planetary Sciences*, 5, 203–226.
- Champness P.E. (1997)**
Applications of transmission electron microscopy in mineralogy. *Advances in Imaging and Electron Physics*, 101, 1–36.
- Chen Y.M., Ohkubo T., Kodzuka M., Morita K. and Hono K. (2009)**
Laser-assisted atom probe analysis of zirconia/spinel nanocomposite ceramics. *Scripta Materialia*, 61, 693–696.
- Chen Y.M., Ohkubo T. and Hono K. (2011)**
Laser assisted field evaporation of oxides in atom probe analysis. *Ultramicroscopy*, 111, 562–566.
- Chen Y.S., Haley D., Gerstly S.S.A., London A.J., Sweeney F., Wepf R.A., Rainforth W.M., Bagot P.A.J. and Moody M.P. (2017)**
Direct observation of individual hydrogen atoms at trapping sites in a ferritic steel. *Science*, 355, 1196–1199.
- Cottrell A.H. and Bilby B.A. (1949)**
Dislocation theory of yielding and strain ageing of iron. *Proceedings of the Physical Society*, 62, 49–62.
- Cukjati J.T., Cooper R.F., Parman S.W., Zhao N., Akey A.J. and Lainghas F.A.T.P. (2019)**
Differences in chemical thickness of grain and phase boundaries: An atom probe tomography study of experimentally deformed wehrlite. *Physics and Chemistry of Minerals*, 46, 845–859.
- Da Costa G., Vurpillot F., Bostel A., Bouet M. and Deconihout B. (2005)**
Design of a delay-line position-sensitive detector with improved performance. *Review of Scientific Instruments*, 76, 013304.
- Daly L., Bland P.A., Saxe D.W., Reddy S.M., Fougerouse D., Rickard W.D.A. and Forman L.V. (2017)**
Nebula sulfidation and evidence for migration of “free-floating” refractory metal nuggets revealed by atom probe microscopy. *Geology*, 45, 847–850.
- Daly L., Bland P.A., Tessalina S., Saxe D.W., Reddy S.M., Fougerouse D., Rickard W.D.A., Forman L.V., La Fontaine A., Caimey J.M., Ringer S.P., Schaefer B.F. and Schwander D. (2018)**
Defining the potential of nanoscale Re-Os isotope systematics using atom probe microscopy. *Geostandards and Geoanalytical Research*, 42, 279–299.
- De Geuser F. and Gault B. (2017)**
Reflections on the projection of ions in atom probe tomography. *Microscopy and Microanalysis*, 23, 238–246.
- De Geuser F., Gault B., Bostel A. and Vurpillot F. (2007a)**
Correlated field evaporation as seen by atom probe tomography. *Surface Science*, 601, 536–543.
- De Geuser F., Lefebvre W., Danoix F., Vurpillot F., Forbord B. and Blavette D. (2007b)**
An improved reconstruction procedure for the correction of local magnification effects in three-dimensional atom-probe. *Surface and Interface Analysis*, 39, 268–272.
- Devaraj A., Colby R., Hess W.P., Perea D.E. and Thevuthasan S. (2013)**
Role of photoexcitation and field ionization in the measurement of accurate oxide stoichiometry by laser-assisted atom probe tomography. *The Journal of Physical Chemistry Letters*, 4, 993–998.
- Devaraj A., Colby R., Vurpillot F. and Thevuthasan S. (2014)**
Understanding atom probe tomography of oxide-supported metal nanoparticles by correlation with atomic-resolution electron microscopy and field evaporation simulation. *The Journal of Physical Chemistry Letters*, 5, 1361–1367.
- Devaraj A., Joshi V.V., Srivastava A., Manandhar S., Moxson V., Duz V.A. and Lavender C. (2016)**
A low-cost hierarchical nanostructured beta-titanium alloy with high strength. *Nature Communications*, 7, 18866.
- Dillon S.J., Tang M., Carter W.C. and Harmer M.P. (2007)**
Complexion: A new concept for kinetic engineering in materials science. *Acta Materialia*, 55, 6208–6218.
- Dmitrieva O., Ponge D., Inden G., Millán J., Choi P., Sietsma J. and Raabe D. (2011)**
Chemical gradients across phase boundaries between martensite and austenite in steel studied by atom probe tomography and simulation. *Acta Materialia*, 59, 364–374.
- Dobrzhinetskaya L., Wirth R. and Green H. (2006)**
Nanometric inclusions of carbonates in Kokchetav diamonds from Kazakhstan: A new constraint for the depth of metamorphic diamond crystallization. *Earth and Planetary Science Letters*, 243, 85–93.
- Dong Y., Etienne A., Frolov A., Fedotova S., Fujii K., Fukuya K., Hatzoglou C., Kuleshova E., Lindgren K., London A., Lopez A., Lozano-Perez S., Miyahara Y., Nagai Y., Nishida K., Radiguet B., Schreiber D.K., Soneda N., Thuvander M., Toyama T., Wang J., Sefta F., Chou P. and Marquis E.A. (2019)**
Atom probe tomography interlaboratory study on clustering analysis in experimental data using the maximum separation distance approach. *Microscopy and Microanalysis*, 25, 356–366.
- Dubosq R., Rogowitz A., Schweinar K., Gault B. and Schneider D.A. (2019)**
A 2D and 3D nanostructural study of naturally deformed pyrite: Assessing the links between trace element mobility and defect structures. *Contributions to Mineralogy and Petrology*, 174, 72.
- Einsle J.F., Eggeman A.S., Martineau B.H., Saghi Z., Collins S.M., Blukis R., Bagot P.A.J., Midgley P.A. and Harrison R.J. (2018)**
Nanomagnetic properties of the meteorite cloudy zone. *Proceedings of the National Academy of Sciences*, 115, E11436–E11445.

references

- Exertier F., La Fontaine A., Corcoran C., Piazolo S., Belousova E., Peng Z., Gault B., Saxe D.W., Fougerouse D., Reddy S.M., Pedrazzini S., Bagot P., Moody M., Langelier B., Moser D., Botton G., Vogel F., Thompson G., Blanchard P., Chiaramonti A., Reinhard D., Rice K., Schreiber D., Kruska K., Wang J. and Cairney J. (2018)**
Atom probe tomography analysis of the reference zircon GJ-1: An interlaboratory study. *Chemical Geology*, 495, 27–35.
- Fahey A.J., Perea D.E., Bartrand J., Arey B.W. and Thevuthasan S. (2016)**
Uranium isotopic ratio measurements of U₃O₈ reference materials by atom probe tomography. *Journal of Environmental Radioactivity*, 153, 206–213.
- Felfer P., Li T., Eder K., Galinski H., Magyar A.P., Bell D.C., Smith G.D.W., Kruse N., Ringer S.P. and Cairney J.M. (2015)**
New approaches to nanoparticle sample fabrication for atom probe tomography. *Ultramicroscopy*, 159, 413–419.
- Felmy A.R., Qafoku O., Arey B.W., Kovarik L., Liu J., Perea D. and Ilton E.S. (2015)**
Enhancing magnesite formation at low temperature and high CO₂ pressure: The impact of seed crystals and minor components. *Chemical Geology*, 395, 119–125.
- Ferraris C. and Auchterlonie G. (2013)**
Inclusions and traces studied by TEM-AEM. In: Nieto F., Livi K.J.T. and Oberti R. (eds), *Minerals at the nanoscale*. Mineralogical Society of Great Britain and Ireland (Twickenham, UK), 1–48.
- Fougerouse D., Reddy S.M., Saxe D.W., Rickard W.D.A., van Riessen A. and Micklethwaite S. (2016)**
Nanoscale gold clusters in arsenopyrite controlled by growth rate not concentration: Evidence from atom probe microscopy. *American Mineralogist*, 101, 1916–1919.
- Fougerouse D., Reddy S.M., Saxe D.W., Erickson T.M., Kirkland C.L., Rickard W.D.A., Seydoux-Guillaume A.-M., Clark C. and Buick I.S. (2018)**
Nanoscale distribution of Pb in monazite revealed by atom probe microscopy. *Chemical Geology*, 479, 251–258.
- Fougerouse D., Reddy S.M., Kirkland C.L., Saxe D.W., Rickard W.D. and Hough R.M. (2019)**
Time-resolved, defect-hosted, trace element mobility in deformed Witwatersrand pyrite. *Geoscience Frontiers*, 10, 55–63.
- Friedrich A.J., Saxe D.W., Adineh V.R., Fougerouse D., Reddy S.M., Rickard W.D.A., Sadek A.Z. and Southall S.C. (2019)**
Direct observation of nanoparticulate goethite recrystallization by atom probe analysis of isotopic tracers. *Environmental Science and Technology*, 53, 13126–13135.
- Gamal El Dien H., Arai S., Doucet L.S., Li Z.-X., Kil Y., Fougerouse D., Reddy S.M., Saxe D.W. and Hamdy M. (2019)**
Cr-spinel records metasomatism not petrogenesis of mantle rocks. *Nature Communications*, 10, 5103.
- Gao R.S., Gibner P.S., Newman J.H., Smith K.A. and Stebbings R.F. (1984)**
Absolute and angular efficiencies of a microchannel-plate position-sensitive detector. *Review of Scientific Instruments*, 55, 1756–1759.
- Gault B., Moody M.P., De Geuser F., Tsafnat G., La Fontaine A., Stephenson LT., Haley D. and Ringer S.P. (2009)**
Advances in the calibration of atom probe tomographic reconstruction. *Journal of Applied Physics*, 105, 034913.
- Gault B., Moody M.P. and De Geuser F. (2010)**
Spatial resolution in atom probe tomography. *Microscopy and Microanalysis*, 16, 99–110.
- Gault B., Haley D., De Geuser F., Moody M.P., Marquis E.A., Larson D.J. and Geiser B.P. (2011)**
Advances in the reconstruction of atom probe tomography data. *Ultramicroscopy*, 111, 448–457.
- Gault B., Danoix F., Hoummada K., Mangelinck D. and Leitner H. (2012a)**
Impact of directional walk on atom probe microanalysis. *Ultramicroscopy*, 113, 182–191.
- Gault B., Moody M.P., Cairney J.M. and Ringer S.P. (2012b)**
Atom probe microscopy. Springer (New York, NY, USA), 396pp.
- Gault B., Saxe D.W., Ashton M.W., Sinnott S.B., Chiaramonti A.N., Moody M.P. and Schreiber D.K. (2016)**
Behavior of molecules and molecular ions near a field emitter. *New Journal of Physics*, 18, 033031.
- Geiser B.P., Larson D.J., Oltman E., Gersl S., Reinhard D., Kelly T.F. and Prosa T.J. (2009)**
Wide-field-of-view atom probe reconstruction. *Microscopy and Microanalysis*, 15, 292–293.
- Genareau K., Pérez-Huerta A. and Laigginhas F. (2019)**
Atom probe tomography analysis of exsolved mineral phases. *Journal of Visualized Experiments*, 152, e59863.
- Gin S., Ryan J.V., Schreiber D.K., Neeway J. and Cabré M. (2013)**
Contribution of atom-probe tomography to a better understanding of glass alteration mechanisms: Application to a nuclear glass specimen altered 25 years in a granitic environment. *Chemical Geology*, 349–350, 99–109.
- Gin S., Jollivet P., Rossa G.B., Tribet M., Mougnaud S., Collin M., Fournier M., Cadel E., Cabré M. and Dupuy L. (2017)**
Atom-probe tomography, TEM and ToF-SIMS study of borosilicate glass alteration rim: A multiscale approach to investigating rate-limiting mechanisms. *Geochimica et Cosmochimica Acta*, 202, 57–76.



references

- Gopon P., Spicuzza M.J., Kelly T.F., Reinhard D., Prosa T.J. and Fournelle J. (2017)**
Ultra-reduced phases in Apollo 16 regolith: Combined field emission electron probe microanalysis and atom probe tomography of submicron Fe-Si grains in Apollo 16 sample 61500. *Meteoritics and Planetary Science*, 52, 1941–1962.
- Gopon P., Douglas J.O., Auger M.A., Hansen L., Wade J., Cline J.S., Robb L.J. and Moody M.P. (2019)**
A nanoscale investigation of Carlin-type gold deposits: An atom-scale elemental and isotopic perspective. *Economic Geology*, 114, 1123–1133.
- Gordon L.M. and Joester D. (2011)**
Nanoscale chemical tomography of buried organic-inorganic interfaces in the chiton tooth. *Nature*, 469, 194–197.
- Gordon L.M., Tran L. and Joester D. (2012)**
Atom probe tomography of apatites and bone-type mineralized tissues. *ACS Nano*, 6, 10667–10675.
- Gordon L.M., Cohen M.J., MacRenaris K.W., Pasteris J.D., Seda T. and Joester D. (2015)**
Amorphous intergranular phases control the properties of rodent tooth enamel. *Science*, 347, 746–750.
- Gorman B.P., Diercks D.R. and Jaeger D. (2008)**
3-D cross-correlation of atom probe and STEM tomography. *Microscopy and Microanalysis*, 14, 1042–1043.
- Gorman B.P., Shepard J.D., Kirchhofer R., Olson J.D. and Kelly T.F. (2011)**
Development of atom probe tomography with *in-situ* STEM imaging and diffraction. *Microscopy and Microanalysis*, 17 (Suppl. 2), 710–711.
- Grandfield K. and Engqvist H. (2012)**
Focused ion beam in the study of biomaterials and biological matter. *Advances in Materials Science and Engineering*, 2012, 841961, 6pp.
- Guo W., Snead B.T., Zhou L., Tang W., Kramer M.J., Cullen D.A. and Poplawsky J.D. (2016)**
Correlative energy-dispersive X-ray spectroscopic tomography and atom probe tomography of the phase separation in an Alnico 8 alloy. *Microscopy and Microanalysis*, 22, 1251–1260.
- Haley D., Choi P. and Raabe D. (2015)**
Guided mass spectrum labelling in atom probe tomography. *Ultramicroscopy*, 159, 338–345.
- Halpin J.E., Webster R.W.H., Gardner H., Moody M.P., Bagot P.A.J. and McLaren D.A. (2019)**
An *in-situ* approach for preparing atom probe tomography specimens by xenon plasma-focussed ion beam. *Ultramicroscopy*, 202, 121–127.
- Harmer M.P. (2011)**
The phase behavior of interfaces. *Science*, 332, 182–183.
- Heck P.R., Stadermann F.J., Isheim D., Auciello O., Daulton T.L., Davis A.M., Elam J.W., Floss C., Hiller J., Larson D.J., Lewis J.B., Mane A., Pellin M.J., Savina M.R., Seidman D.N. and Stephan T. (2014)**
- Atom-probe analyses of nanodiamonds from Allende. *Meteoritics and Planetary Science*, 49, 453–467.
- Hellman O.C., Vandenbroucke J.A., Rusing J., Isheim D. and Seidman D.N. (2000)**
Analysis of three-dimensional atom-probe data by the proximity histogram. *Microscopy and Microanalysis*, 6, 437–444.
- Hellmann R., Cotte S., Cadet E., Malladi S., Karlsson L.S., Lozano-Perez S., Cabie M. and Seyeux A. (2015)**
Nanometre-scale evidence for interfacial dissolution–reprecipitation control of silicate glass corrosion. *Nature Materials*, 14, 307–311.
- Hiraga T., Anderson I.M. and Kohlstedt D.L. (2003)**
Chemistry of grain boundaries in mantle rocks. *American Mineralogist*, 88, 1015–1019.
- Hiraga T., Anderson I.M. and Kohlstedt D.L. (2004)**
Grain boundaries as reservoirs of incompatible elements in the Earth's mantle. *Nature*, 427, 699–703.
- Hono K., Ohkubo T., Chen Y.M., Kodzuka M., Ohishi K., Sepehri-Amin H., Li F., Kinno T., Tomiya S. and Kanitani Y. (2011)**
Broadening the applications of the atom probe technique by ultraviolet femtosecond laser. *Ultramicroscopy*, 111, 576–583.
- Hoppe P., Cohen S. and Meibom A. (2013)**
NanoSIMS: Technical aspects and applications in cosmochemistry and biological geochemistry. *Geostandards and Geoanalytical Research*, 37, 111–154.
- Hudson D., Smith G.D.W. and Gault B. (2011)**
Optimisation of mass ranging for atom probe microanalysis and application to the corrosion processes in Zr alloys. *Ultramicroscopy*, 111, 480–486.
- Hyde J.M. and English C.A. (2001)**
An analysis of the structure of irradiation induced Cu-enriched clusters in low and high nickel welds. Presented at the Materials Research Society Symposium, 650, R6.6.1–R6.6.12.
- Hyde J.M., Burke M.G., Boothby R.M. and English C.A. (2009)**
Characterisation of the early stages of solute clustering in 1Ni–1.3Mn welds containing Cu. *Ultramicroscopy*, 109, 510–517.
- Ironside C.N., Saxey D.W., Rickard W.D.A., Gray C., McGlynn E., Reddy S.M. and Marks N.A. (2017)**
Atom probe microscopy of zinc isotopic enrichment in ZnO nanorods. *AIP Advances*, 7, 025004.
- Jiao Z.B., Luan J.H., Guo W., Poplawsky J.D. and Liu C.T. (2016)**
Effects of welding and post-weld heat treatments on nanoscale precipitation and mechanical properties of an ultra-high strength steel hardened by NiAl and Cu nanoparticles. *Acta Materialia*, 120, 216–227.
- Johnson L.J.S., Thuvander M., Stiller K., Odén M. and Hultman L. (2013)**
Blind deconvolution of time-of-flight mass spectra from atom probe tomography. *Ultramicroscopy*, 132, 60–64.

references

- Karahka M. and Kreuzer H.J. (2013)**
Field evaporation of oxides: A theoretical study. *Ultramicroscopy*, 132, 54–59.
- Karahka M. and Kreuzer H.J. (2015)**
Field evaporation of insulators and semiconductors: Theoretical insights for ZnO. *Ultramicroscopy*, 159, 156–161.
- Karahka M., Xia Y. and Kreuzer H.J. (2015)**
The mystery of missing species in atom probe tomography of composite materials. *Applied Physics Letters*, 107, 062105–4.
- Keller R.R. and Geiss R.H. (2012)**
Transmission EBSD from 10 nm domains in a scanning electron microscope. *Journal of Microscopy*, 245, 245–251.
- Kelly T.F. (2017)**
Atomic-scale analytical tomography. *Microscopy and Microanalysis*, 23, 34–45.
- Kelly T.F. and Panitz J.A. (2017)**
The first fifty years of atom probe. *Microscopy Today*, 25, 12–17.
- Kelly T.F., Camus P.P., Larson D.J., Holzman L.M. and Bajikar S.S. (1996)**
On the many advantages of local-electrode atom probes. *Ultramicroscopy*, 62, 29–42.
- Kelly T.F., Gribb T.T., Olson J.D., Martens R.L., Shepard J.D., Wiener S.A., Kunicki T.C., Ulfig R.M., Lenz D.R., Strennen E.M., Oltman E., Bunton J.H. and Strait D.R. (2004)**
First data from a commercial local electrode atom probe (LEAP). *Microscopy and Microanalysis*, 10, 373–383.
- Kelly T.F., Vella A., Bunton J.H., Houard J., Silaeva E.P., Bogdanowicz J. and Vandervorst W. (2014)**
Laser pulsing of field evaporation in atom probe tomography. *Current Opinion in Solid State and Materials Science*, 18, 81–89.
- Kinno T., Tomita M., Ohkubo T., Takeno S. and Hono K. (2014)**
Laser-assisted atom probe tomography of ^{18}O -enriched oxide thin film for quantitative analysis of oxygen. *Applied Surface Science*, 290, 194–198.
- Kinno T., Kitamoto K., Takeno S. and Tomita M. (2015)**
Laser-assisted atom probe tomography of ^{15}N -enriched nitride thin films for analysis of nitrogen distribution in silicon-based structure. *Applied Surface Science*, 349, 89–92.
- Kirchhofer R., Diercks D.R., Gorman B.P., Ihlefeld J.F., Kotula P.G., Shelton C.T. and Brennecke G.L. (2014)**
Quantifying compositional homogeneity in $\text{Pb}(\text{Zr}, \text{Ti})\text{O}_3$ using atom probe tomography. *Journal of the American Ceramic Society*, 97, 2677–2697.
- Kirkland C.L., Fougerousse D., Reddy S.M., Hollis J. and Saxe D.W. (2018)**
Assessing the mechanisms of common Pb incorporation into titanite. *Chemical Geology*, 483, 558–566.
- Klapper H. (2010)**
Generation and propagation of defects during crystal growth. In: Dhanaraj G., Byrappa K., Prasad V. and Dudley M. (eds), *Springer handbook of crystal growth*. Volume 55. Springer (Berlin Heidelberg, Berlin), 93–132.
- Kölling S. and Vandervost W. (2009)**
Failure mechanisms of silicon-based atom-probe tips. *Ultramicroscopy*, 109, 486–491.
- Krakauer B.W. and Seidman D.N. (1992)**
Systematic procedures for atom-probe field-ion microscopy studies of grain boundary segregation. *Review of Scientific Instruments*, 63, 4071–4079.
- Krakauer B.W., Hu J.G., Kuo S.M., Mallick R.L., Seki A., Seidman D.N., Baker J.P. and Loyd R.J. (1990)**
A system for systematically preparing atom-probe field-ion-microscope specimens for the study of internal interfaces. *Review of Scientific Instruments*, 61, 3390–3398.
- Kübel C., Voigt A., Schoenmakers R., Otten M., Su D., Lee T.-C., Carlsson A. and Bradley J. (2005)**
Recent advances in electron tomography: TEM and HAADF-STEM tomography for materials science and semiconductor applications. *Microscopy and Microanalysis*, 11, 378–400.
- Kuhlman K.R., Martens R.L., Kelly T.F., Evans N.D. and Miller M.K. (2001)**
Fabrication of specimens of metamorphic magnetite crystals for field ion microscopy and atom probe microanalysis. *Ultramicroscopy*, 89, 169–176.
- Kusiak M.A., Dunkley D.J., Wirth R., Whitehouse M.J., Wilde S.A. and Marquardt K. (2015)**
Metallic lead nanospheres discovered in ancient zircons. *Proceedings of the National Academy of Sciences*, 112, 4958–4963.
- La Fontaine A., Zavgorodny A., Liu H., Zheng R., Swain M. and Cairney J. (2016)**
Atomic-scale compositional mapping reveals Mg-rich amorphous calcium phosphate in human dental enamel. *Science Advances*, 2, e1601145.
- La Fontaine A., Piazolo S., Trimby P., Yang L. and Cairney J.M. (2017)**
Laser-assisted atom probe tomography of deformed minerals: A zircon case study. *Microscopy and Microanalysis*, 23, 1–10.
- Langelier B., Wang X. and Grandfield K. (2016)**
Atomic scale chemical tomography of human bone. *Scientific Reports*, 7, 39958.
- Larson D.J., Foord D.T., Petford-Long A.K., Liew H., Blamire M.G., Cerezo A. and Smith G. (1999)**
Field-ion specimen preparation using focused ion-beam milling. *Ultramicroscopy*, 79, 287–283.



references

- Larson D.J., Alvis R.L., Lawrence D.F., Prosa T.J., Ulfig R.M., Reinhard D.A., Clifton P.H., Gerstl S., Bunton J.H., Lenz D.R., Kelly T. and Stiller K. (2008)**
Analysis of bulk dielectrics with atom probe tomography. *Microscopy and Microanalysis*, 14, 1254–1255.
- Larson D.J., Geiser B.P., Prosa T.J., Gerstl S.S.A., Reinhard D.A. and Kelly T.F. (2011)**
Improvements in planar feature reconstructions in atom probe tomography. *Journal of Microscopy*, 243, 15–30.
- Larson D.J., Geiser B.P., Prosa T.J. and Kelly T.F. (2012)**
On the use of simulated field-evaporated specimen apex shapes in atom probe tomography data reconstruction. *Microscopy and Microanalysis*, 18, 953–963.
- Larson D.J., Gault B., Geiser B.P., De Geuser F. and Vurpillot F. (2013a)**
Atom probe tomography spatial reconstruction: Status and directions. *Current Opinion in Solid State and Materials Science*, 17, 236–247.
- Larson D.J., Prosa T.J., Ulfig R.M., Geiser B.P. and Kelly T.F. (2013b)**
Local electrode atom probe tomography. Springer (New York, USA), 318pp.
- Larson D.J., Giddings A.D., Wu Y., Verheijen M.A., Prosa T.J., Rozzeboom F., Rice K.P., Kessels W.M.M., Geiser B.P. and Kelly T.F. (2015)**
Encapsulation method for atom probe tomography analysis of nanoparticles. *Ultramicroscopy*, 159, 420–426.
- Larson D.J., Prosa T.J., Perea D.E., Inoue K. and Mangelinck D. (2016)**
Atom probe tomography of nanoscale electronic materials. *MRS Bulletin*, 41, 30–34.
- Laurent A.T., Seydoux-Guillaume A.-M., Duchêne S., Bingen B., Bosse V. and Datias L. (2016)**
Sulphate incorporation in monazite lattice and dating the cycle of sulphur in metamorphic belts. *Contributions to Mineralogy and Petrology*, 171, 1–19.
- Lee J.K.W. (1995)**
Multipath diffusion in geochronology. *Contributions to Mineralogy and Petrology*, 120, 60–82.
- Lee M.R. (2010)**
Transmission electron microscopy (TEM) of Earth and planetary materials: A review. *Mineralogical Magazine*, 74, 1–27.
- Lefebvre W., Hernandez-Maldonado D., Moyon F., Cuvilly F., Vaudolon C., Shinde D. and Vurpillot F. (2015)**
HAADF-STEM atom counting in atom probe tomography specimens: Towards quantitative correlative microscopy. *Ultramicroscopy*, 159, 403–412.
- Lefebvre-Ulikson W., Vurpillot F. and Sauvage X. (Editors) (2016)**
Atom probe tomography: Put theory into practice. Academic Press (London, UK), 402pp.
- Lejček P. (2010)**
Grain boundary segregation in metals. Springer series in materials science, Volume 136. Springer (New York, USA), 239pp.
- Lewis J.B., Isheim D., Floss C. and Seidman D.N. (2015)**
 $^{12}\text{C}/^{13}\text{C}$ -ratio determination in nanodiamonds by atom-probe tomography. *Ultramicroscopy*, 159, 248–254.
- Liddle J.A., Norman A., Cerezo A. and Grovenor C. (1988)**
Pulsed laser atom probe analysis of ternary and quaternary III-V epitaxial layers. *Journal de Physique Colloques*, 49, 509–514.
- Loi S.T., Gault B., Ringer S.P., Larson D.J. and Geiser B.P. (2013)**
Electrostatic simulations of a local electrode atom probe: The dependence of tomographic reconstruction parameters on specimen and microscope geometry. *Ultramicroscopy*, 132, 107–113.
- London A.J., Haley D. and Moody M.P. (2017)**
Single-ion deconvolution of mass peak overlaps for atom probe microscopy. *Microscopy and Microanalysis*, 23, 300–306.
- Locharukpong C., Tweddle D., Martin T.L., Wu M., Grovenor C.R.M., Moody M.P. and Wilshaw P.R. (2017)**
Specimen preparation methods for elemental characterisation of grain boundaries and isolated dislocations in multicrystalline silicon using atom probe tomography. *Materials Characterization*, 131, 472–479.
- Lütge A. and Arvidson R.S. (2008)**
The mineral–water interface. In: Brantley S., Kubicki J.D. and White A. (eds), *Kinetics of water rock interaction*. Springer (New York), 73–107.
- Mamyrin B.A., Karataev V.I., Shmikk D.V. and Zagulin V.A. (1973)**
The mass-reflectron, a new nonmagnetic time-of-flight mass spectrometer with high resolution. *Journal of Experimental and Theoretical Physics*, 37, 45–48.
- Mancini L., Amirifar N., Shinde D., Blum I., Gilbert M., Vella A., Vurpillot F., Lefebvre W., Lardé R., Talbot E., Pareige P., Portier X., Ziani A., Davesne C., Durand C., Emery J., Butté R., Carlin J.-F., Grandjean N. and Rigutti L. (2014)**
Composition of wide bandgap semiconductor materials and nanostructures measured by atom probe tomography and its dependence on the surface electric field. *The Journal of Physical Chemistry C*, 118, 24136–24151.
- Marceau R.K.W., Sha G., Ferragut R., Dupasquier A. and Ringer S.P. (2010)**
Solute clustering in Al–Cu–Mg alloys during the early stages of elevated temperature ageing. *Acta Materialia*, 58, 4923–4939.
- Marquardt K. and Faul U.H. (2018)**
The structure and composition of olivine grain boundaries: 40 years of studies, status and current developments. *Physics and Chemistry of Minerals*, 45, 139–172.

references

- Marquis E.A. and Hyde J.M. (2010)**
 Applications of atom-probe tomography to the characterisation of solute behaviours. *Materials Science and Engineering R*, 69, 37–62.
- Marquis E.A., Yahya N.A., Larson D.J., Miller M.K. and Todd R.I. (2010)**
 Probing the improbable: Imaging C atoms in alumina. *Materials Today*, 13, 34–36.
- McKenzie W.R., Marquis E.A. and Munroe P.R. (2010)**
 Focused ion beam sample preparation for atom probe tomography. In: Mendez-Vilas A. and Diaz J. (eds), *Microscopy: Science, technology, applications and education, Volume 3*. Formatax Research Centre (Badajoz, Spain), 1800–1810.
- Meisenkothen F., Steel E.B., Prosa T.J., Henry K.T. and Kolly R.P. (2015)**
 Effects of detector dead-time on quantitative analyses involving boron and multi-hit detection events in atom probe tomography. *Ultramicroscopy*, 159, 101–111.
- Melmed A.J. and Carroll J.J. (1984)**
 An approach to realism in field ion microscopy via zone electropolishing. *Journal of Vacuum Science and Technology A*, 2, 1388–1388.
- Mezger K. and Krogstad E.J. (1997)**
 Interpretation of discordant U-Pb zircon ages: An evaluation. *Journal of Metamorphic Geology*, 15, 127–140.
- Miller M.K. (2000)**
 Atom probe tomography – Analysis at the atomic level. Kluwer Academic/Plenum Publications (New York), 247 pp.
- Miller M.K. (2006)**
 Atom probe tomography characterization of solute segregation to dislocations and interfaces. *Journal of Materials Science*, 41, 7808–7813.
- Miller M.K. and Forbes R.G. (2014)**
 Atom-probe tomography: The local electrode atom probe. Springer (New York, NY, USA), 423 pp.
- Miller M.K. and Hetherington M.G. (1991)**
 Local magnification effects in the atom probe. *Surface Science*, 246, 442–449.
- Miller M.K. and Russell K.F. (1992)**
 An APFIM investigation of a weathered region of the Santa Catharina meteorite. *Surface Science*, 226, 441–445.
- Miller M.K. and Russell K.F. (2007)**
 Atom probe specimen preparation with a dual beam SEM/FIB miller. *Ultramicroscopy*, 107, 761–766.
- Miller M.K., Cerezo A., Hetherington M.G. and Smith G.D. (1996)**
 Atom probe field ion microscopy. Oxford University Press (Oxford), 509 pp.
- Miller M.K., Russell K.F., Thompson K., Alvis R. and Larson D.J. (2007)**
 Review of atom probe FIB-based specimen preparation methods. *Microscopy and Microanalysis*, 13, 428–436.
- Montalvo S.D., Reddy S.M., Saxe D.W., Rickard W.D.A., Fougerouse D., Quadir Z. and Johnson T.E. (2019)**
 Nanoscale constraints on the shock-induced transformation of zircon to reidite. *Chemical Geology*, 507, 85–95.
- Moody M.P., Ceguerra A.V., Breen A.J., Cui X.Y., Gault B., Stephenson L.T., Marceau R.K.W., Powles R.C. and Ringer S.P. (2014)**
 Atomically resolved tomography to directly inform simulations for structure–property relationships. *Nature Communications*, 5, 5501.
- Moser D.E., Arcuri G.A., Reinhard D.A., White L.F., Darling J.R., Barker I.R., Larson D.J., Irving A.J., McCubbin F.M., Tait K.T., Roszjar J., Wittmann A. and Davis C. (2019)**
 Decline of giant impacts on Mars by 4.48 billion years ago and an early opportunity for habitability. *Nature Geoscience*, 12, 522–527.
- Mukherjee S., Watanabe H., Isheim D., Seidman D.N. and Moutanabbir O. (2016)**
 Laser-assisted field evaporation and three-dimensional atom-by-atom mapping of diamond isotopic homojunctions. *Nano Letters*, 16, 1335–1344.
- Müller E.W. (1936)**
 Experiments of the theory of electron emission under the influence of high field strength. *Physikalische Zeitschrift*, 37, 838–842.
- Müller E.W. (1951)**
 Das feldionenmikroskop. *Zeitschrift für Physik*, 131, 136–142.
- Müller E.W. (1956)**
 Field desorption. *Physical Review*, 102, 618–624.
- Müller E.W., Nakamura S., Nishikawa O. and McLane S.B. (1965)**
 Gas-surface interactions and field-ion microscopy of non-refractory metals. *Journal of Applied Physics*, 36, 2496–2503.
- Müller E.W., Panitz J.A. and McLane S.B. (1968)**
 The atom-probe field ion microscope. *Review of Scientific Instruments*, 39, 83–86.
- Müller M., Saxe D.W., Smith G.D.W. and Gault B. (2011)**
 Some aspects of the field evaporation behaviour of GaSb. *Ultramicroscopy*, 111, 487–492.
- Nishikawa O., Sekine T., Ohtani Y., Maeda K., Numada Y., Watanabe M., Iwatsuki M., Aoki S., Itoh J. and Yamanaka K. (1998)**
 Development of a scanning atom probe and atom-by-atom mass analysis of diamonds. *Applied Physics A: Materials Science and Processing*, 66, S11–S16.



references

- Pang Y. and Wynblatt P. (2006)**
Effects of Nb doping and segregation on the grain boundary plane distribution in TiO₂. *Journal of the American Ceramic Society*, 89, 666–671.
- Panitz J.A. (1982)**
Field-ion microscopy – A review of basic principles and selected applications. *Journal of Physics E-Scientific Instruments*, 15, 1281–1294.
- Parman S.W., Diercks D.R., Gorman B.P. and Cooper R.F. (2015)**
Atom probe tomography of isoferroplatinum. *American Mineralogist*, 100, 852–860.
- Peng Z., Vurpillot F., Choi P.-P., Li Y., Raabe D. and Gault B. (2018)**
On the detection of multiple events in atom probe tomography. *Ultramicroscopy*, 189, 54–60.
- Pérez-Huerta A. and Laigindas F. (2018)**
Preliminary data on the nanoscale chemical characterization of the inter-crystalline organic matrix of a calcium carbonate biomineral. *Minerals*, 8, 223–12.
- Pérez-Huerta A., Laigindas F., Reinhard D.A., Prosa T.J. and Martens R.L. (2016)**
Atom probe tomography (APT) of carbonate minerals. *Micron*, 80, 83–89.
- Peterman E.M., Reddy S.M., Saxe D.W., Snoeyenbos D.R., Rickard W.D.A., Fougerouse D. and Kylander-Clark A.R.C. (2016)**
Nanogeochronology of discordant zircon measured by atom probe microscopy of Pb-enriched dislocation loops. *Science Advances*, 2, e1601318.
- Peterman E.M., Reddy S.M., Saxe D.W., Fougerouse D., Snoeyenbos D.R. and Rickard W.D.A. (2019)**
Nanoscale processes of trace element mobility in metamorphosed zircon. *Contributions to Mineralogy and Petrology*, 174, 1–29.
- Philippe T., De Geuser F., Dugay S., Lefebvre W., Cojocaru-Mirédin O., Da Costa G. and Blavette D. (2009)**
Clustering and nearest neighbour distances in atom-probe tomography. *Ultramicroscopy*, 109, 1304–1309.
- Piazolo S., La Fontaine A., Trimby P., Harley S., Yang L., Armstrong R. and Caimey J.M. (2016)**
Deformation-induced trace element redistribution in zircon revealed using atom probe tomography. *Nature Communications*, 7, 1–7.
- Piazolo S., Belousova E., La Fontaine A., Corcoran C. and Caimey J.M. (2017)**
Trace element homogeneity from micron- to atomic scale: Implication for the suitability of the zircon GJ-1 as a trace element reference material. *Chemical Geology*, 456, 10–18.
- Prentzler B.I., Urbanik-Shannon C.A., Giannuzzi L.A., Brown S.R., Irwin R.B., Shofner T.L. and Stevie F.A. (2003)**
The correlation between ion beam/material interactions and practical FIB specimen preparation. *Microscopy and Microanalysis*, 9, 216–236.
- Priester L. (2001)**
“Dislocation-interface” interaction – Stress accommodation processes at interfaces. *Materials Science and Engineering A*, A309–310, 430–439.
- Prosa T.J. and Larson D.J. (2017)**
Modern focused-ion-beam-based site-specific specimen preparation for atom probe tomography. *Microscopy and Microanalysis*, 23, 194–209.
- Prosa T.J., Geiser B.P., Lawrence D., Olson D. and Larson D.J. (2014)**
Developing detection efficiency standards for atom probe tomography. In: Postek M.T. and Orji N.G. (eds), *Instrumentation, metrology, and standards for nanomanufacturing. Optics and Semiconductors VIII. Proceedings*. SPIE (Bellingham, WA, USA), Volume 9173, 917307.
- Raabe D., Herbig M., Sandlöbes S., Li Y., Tykko D., Kuzmina M., Ponge D. and Choi P.P. (2014)**
Grain boundary segregation engineering in metallic alloys: A pathway to the design of interfaces. *Current Opinion in Solid State and Materials Science*, 18, 253–261.
- Reddy S.M., van Riessen A., Saxe D.W., Johnson T.E., Rickard W.D.A., Fougerouse D., Fischer S., Prosa T.J., Rice K.P., Reinhard D.A., Chen Y. and Olson D. (2016)**
Mechanisms of deformation-induced trace element migration in zircon resolved by atom probe and correlative microscopy. *Geochimica et Cosmochimica Acta*, 195, 158–170.
- Reinhard D.A., Moser D.E., Martin I., Rice K.P., Chen Y., Olson D., Lawrence D., Prosa T.J. and Larson D.J. (2018)**
Atom probe tomography of Phalaborwa baddeleyite and reference zircon BR266. In: Moser D.E., Corfu F., Darling J.R., Reddy S.M. and Tait K. (eds), *Microstructural geochronology: Planetary records down to atom scale*. Wiley (Hoboken, NJ, USA), 315–326.
- Rice K.P., Chen Y., Prosa T.J. and Larson D.J. (2016)**
Implementing transmission electron backscatter diffraction for atom probe tomography. *Microscopy and Microanalysis*, 22, 583–588.
- Rickard W.D.A., Reddy S.M., Saxe D.W., Fougerouse D., Timms N.E., Daly L., Peterman E., Cavosie A. and Jourdan F. (2020)**
Novel applications of FIB-based ToF-SIMS in atom probe tomography workflows. *Microscopy and Microanalysis*, <https://doi.org/10.1017/S1431927620000136>.
- Riley J.R., Bernal R.A., Li Q., Espinosa H.D., Wang G.T. and Lauhon L.J. (2012)**
Atom probe tomography of α -axis GaN nanowires: Analysis of nonstoichiometric evaporation behavior. *ACS Nano*, 6, 3898–3906.
- Rout S.S., Heck P.R., Isheim D., Stephan T., Zaluzec N.J., Miller D.J., Davis A.M. and Seidman S.N. (2017)**
Atom-probe tomography and transmission electron microscopy of the kamacite-taenite interface in the fast-cooled Bristol IVa iron meteorite. *Meteoritics and Planetary Science*, 52, 2707–2729.

references

- Sakuma T., Ikuhara Y., Takigawa Y. and Thavorniti P. (1997)**
Importance of grain boundary chemistry on the high-temperature plastic flow in oxide ceramics. *Materials Science and Engineering A*, 234, 226–229.
- Santhanagopalan D., Schreiber D.K., Perea D.E., Martens R.L., Janssen Y., Khalifah P. and Meng Y.S. (2015)**
Effects of laser energy and wavelength on the analysis of LiFePO₄ using laser assisted atom probe tomography. *Ultramicroscopy*, 148, 57–66.
- Saxey D.W. (2011)**
Correlated ion analysis and the interpretation of atom probe mass spectra. *Ultramicroscopy*, 111, 473–479.
- Saxey D.W., Moser D.E., Piazolo S., Reddy S.M. and Valley J.W. (2018a)**
Atomic worlds: Current state and future of atom probe tomography in geoscience. *Scripta Materialia*, 148, 115–121.
- Saxey D.W., Reddy S.M., Fougerouse D. and Rickard W.D.A. (2018b)**
The optimization of zircon analyses by laser-assisted atom probe microscopy: Insights from the 91500 zircon standard. In: Moser D.E., Corfu F., Darling J.R., Reddy S.M. and Tait K. (eds), *Microstructural geochronology: Planetary records down to atom scale*. Wiley (Hoboken, NJ, USA), 293–313.
- Saxey D.W., Fougerouse D., Rickard W.D.A. and Reddy S.M. (2019)**
Spatial reconstruction of atom probe data from zircon. *Microscopy and Microanalysis*, 25 (Suppl. 2), 2536–2537.
- Schipper C.I., Rickard W.D.A., Reddy S.M., Saxey D.W., Castro J.M., Fougerouse D., Quadir Z., Conway C., Prior D.J. and Lilly K. (2020)**
Volcanic SiO₂-cristobalite: A natural product of chemical vapor deposition. *American Mineralogist*. <https://doi.org/10.2138/am-2020-7236>
- Schirhagl R., Raatz N., Meijer J., Markham M., Gerstel S.S.A. and Degen C.L. (2015)**
Nanometer-scale isotope analysis of bulk diamond by atom probe tomography. *Diamond and Related Materials*, 60, 60–65.
- Schmidt J.E., Ye X., van Ravenhorst I.K., Oord R., Shapiro D.A., Yu Y.S., Bare S.R., Meirer F., Poplawsky J.D. and Weckhuysen B.M. (2019)**
Probing the location and speciation of elements in zeolites with correlated atom probe tomography and scanning transmission X-ray microscopy. *ChemCatChem*, 11, 488–494.
- Schreiber D.K., Olszta M.J. and Bruemmer S.M. (2013)**
Directly correlated transmission electron microscopy and atom probe tomography of grain boundary oxidation in a Ni-Al binary alloy exposed to high-temperature water. *Scripta Materialia*, 69, 509–512.
- Schreiber D.K., Chiaramonti A.N., Gordon L.M. and Kruska K. (2014)**
Applicability of post-ionization theory to laser-assisted field evaporation of magnetite. *Applied Physics Letters*, 105, 244106–6.
- Seydoux-Guillaume A.-M., Fougerouse D., Laurent A.T., Gardés E., Reddy S.M. and Saxey D.W. (2019)**
Nanoscale resetting of the Th/Pb system in an isotopically-closed monazite grain: A combined atom probe and transmission electron microscopy study. *Geoscience Frontiers*, 10, 65–76.
- Shimizu Y., Kawamura Y., Uematsu M., Itoh K.M., Tomita M., Sasaki M., Uchida H. and Takahashi M. (2009)**
Atom probe microscopy of three-dimensional distribution of silicon isotopes in ²⁸Si/³⁰Si isotope superlattices with sub-nanometer spatial resolution. *Journal of Applied Physics*, 106, 076102–4.
- Shimizu Y., Takamizawa H., Kawamura Y., Uematsu M., Toyama T., Inoue K., Haller E.E., Itoh K.M. and Nagai Y. (2013)**
Atomic-scale characterization of germanium isotopic multilayers by atom probe tomography. *Journal of Applied Physics*, 113, 026101–4.
- Silaeva E.P., Karahka M. and Kreuzer H.J. (2013)**
Atom probe tomography and field evaporation of insulators and semiconductors: Theoretical issues. *Current Opinion in Solid State and Materials Science*, 17, 211–216.
- Silaeva E.P., Arnoldi L., Karahka M.L., Deconihout B., Menand A., Kreuzer H.J. and Vella A. (2014)**
Do dielectric nanostructures turn metallic in high-electric dc fields? *Nano Letters*, 14, 6066–6072.
- Smith G.D.W., Hudson D., Styman P.D. and Williams C.A. (2013)**
Studies of dislocations by field ion microscopy and atom probe tomography. *Philosophical Magazine*, 93, 3726–3740.
- Stephan T., Trappitsch R., Davis A.M., Pellin M.J., Rost D., Savina M.R., Yokochi R. and Liu N. (2016)**
CHILL – the Chicago Instrument for Laser Ionization – A new tool for isotope measurements in cosmochemistry. *International Journal of Mass Spectrometry*, 407, 1–15.
- Stephenson L.T., Moody M.P., Liddicoat P.V. and Ringer S.P. (2007)**
New techniques for the analysis of fine-scaled clustering phenomena within atom probe tomography (APT) data. *Microscopy and Microanalysis*, 13, 448–463.
- Stokes A., Al-Jassim M., Diercks D.R., Egaas B. and Gorman B. (2016)**
3-D point defect density distributions in thin film Cu(ln, Ga)Se₂ measured by atom probe tomography. *Acta Materialia*, 102, 32–37.



references

- Sutton A.P. and Balluffi R.W. (2006)**
Interfaces in crystalline materials. Oxford University Press (Oxford), 852pp.
- Takahashi J., Kawakami K., Kobayashi Y. and Tarui T. (2010)**
 The first direct observation of hydrogen trapping sites in TiC precipitation – Hardening steel through atom probe tomography. *Scripta Materialia*, 63, 261–264.
- Takahashi J., Kawakami K. and Kobayashi Y. (2011)**
 Quantitative analysis of carbon content in cementite in steel by atom probe tomography. *Ultramicroscopy*, 111, 1233–1238.
- Taylor S.D., Liu J., Arey B.W., Schreiber D.K., Perea D.E. and Rosso K.M. (2018)**
 Resolving iron(II) sorption and oxidative growth on hematite (001) using atom probe tomography. *The Journal of Physical Chemistry C*, 122, 3903–3914.
- Taylor S.D., Liu J., Zhang X., Arey B.W., Kovarik L., Schreiber D.K., Perea D.E. and Rosso K.M. (2019)**
 Visualizing the iron atom exchange front in the Fe(II)-catalyzed recrystallization of goethite by atom probe tomography. *Proceedings of the National Academy of Sciences*, 116, 2866–2874.
- Tedsree K., Li T., Jones S., Chan C.W.A., Yu K.M.K., Bagot P.A.J., Marquis E.A., Smith G.D.W. and Tsang S.C.E. (2011)**
 Hydrogen production from formic acid decomposition at room temperature using a Ag-Pd core-shell nanocatalyst. *Nature Nanotechnology*, 6, 302–307.
- Thompson K., Larson D.J. and Ulfig R.M. (2005)**
 Pre-sharpened and flat-top microtip coupons: A quantitative comparison for atom-probe analysis studies. *Microscopy and Microanalysis*, 11, 882–883.
- Thompson K., Bunton J.H., Kelly T.F. and Larson D.J. (2006)**
 Characterization of ultralow-energy implants and towards the analysis of three-dimensional dopant distributions using three-dimensional atom-probe tomography. *Journal of Vacuum Science and Technology B: Microelectronics and Nanometer Structures*, 24, 421–427.
- Thompson K., Flaitz P.L., Ronsheim P., Larson D.J. and Kelly T.F. (2007a)**
 Imaging of arsenic Cottrell atmospheres around silicon defects by three-dimensional atom probe tomography. *Science*, 317, 1370–1374.
- Thompson K., Lawrence D., Larson D.J., Olson J.D., Kelly T.F. and Gorman B.P. (2007b)**
In situ site-specific specimen preparation for atom probe tomography. *Ultramicroscopy*, 107, 131–139.
- Thuvander M. (2016)**
 On the accuracy of compositional quantification for atom probe tomography. *Microscopy and Microanalysis*, 22, 642–643.
- Thuvander M., Weidow J., Angseryd J., Falk L.K.L., Liu F., Sonestedt M., Stiller K. and Andrén H.O. (2011)**
 Quantitative atom probe analysis of carbides. *Ultramicroscopy*, 111, 604–608.
- Thuvander M., Kvist A., Johnson L.J.S., Weidow J. and Andrén H.-O. (2013)**
 Reduction of multiple hits in atom probe tomography. *Ultramicroscopy*, 132, 81–85.
- Thuvander M., Shinde D., Rehan A., Ejnermark S. and Stiller K. (2019)**
 Improving compositional accuracy in APT analysis of carbides using a decreased detection efficiency. *Microscopy and Microanalysis*, 25, 454–461.
- Trimby P.W. (2012)**
 Orientation mapping of nanostructured materials using transmission Kikuchi diffraction in the scanning electron microscope. *Ultramicroscopy*, 120, 16–24.
- Tsong T.T. (1978)**
 Measurement of the field evaporation rate of several transition metals. *Journal of Physics F: Metal Physics*, 8, 1349–1352.
- Tsong T.T. (1984)**
 Pulsed-laser-stimulated field-ion emission from metal and semiconductor surfaces – A time-of-flight study of the formation of atomic, molecular, and cluster ions. *Physical Review B*, 30, 4946–4961.
- Valley J.W., Cavosie A.J., Ushikubo T., Reinhard D.A., Lawrence D.F., Larson D.J., Clifton P.H., Kelly T.F., Wilde S.A., Moser D.E. and Spicuzza M. J. (2014)**
 Hadean age for a post-magma-ocean zircon confirmed by atom-probe tomography. *Nature Geoscience*, 7, 219–223.
- Valley J.W., Reinhard D.A., Cavosie A.J., Ushikubo T., Lawrence D.F., Larson D.J., Kelly T.F., Snoeyenbos D.R. and Strickland A. (2015)**
 Nano- and micro-geochronology in Hadean and Archean zircons by atom-probe tomography and SIMS: New tools for old minerals. *American Mineralogist*, 100, 1355–1377.
- Van Landeghem H.P., Langelier B., Gault B., Panahi D., Korinek A., Purdy G.R. and Zurob H.S. (2017)**
 Investigation of solute/interphase interaction during ferrite growth. *Acta Materialia*, 124, 536–543.
- Vaumousse D., Cerezo A. and Warren P.J. (2003)**
 A procedure for quantification of precipitate microstructures from three-dimensional atom probe data. *Ultramicroscopy*, 95, 215–221.
- Veblen D.R., Banfield J.F., Guthrie G.D., Heaney P.J., Ilton E.S., Livi K.J. and Smelik E.A. (1993)**
 High-resolution and analytical transmission electron microscopy of mineral disorder and reactions. *Science*, 260, 1465–1472.
- Verberne R., Saxey D.W., Reddy S.M., Rickard W.D.A., Fougerouse D. and Clark C. (2019)**
 Analysis of natural rutile (TiO_2) by laser-assisted atom probe tomography. *Microscopy and Microanalysis*, 25, 539–546.
- Vurpillot F., Bostel A. and Blavette D. (2000a)**
 Trajectory overlaps and local magnification in three-dimensional atom probe. *Applied Physics Letters*, 76, 3127–3129.

references

- Vurpillot F., Bostel A., Cadel E. and Blavette D. (2000b)**
The spatial resolution of 3D atom probe in the investigation of single-phase materials. *Ultramicroscopy*, 84, 213–224.
- Vurpillot F., Larson D. and Cerezo A. (2004)**
Improvement of multilayer analyses with a three-dimensional atom probe. *Surface and Interface Analysis*, 36, 552–558.
- Vurpillot F., Houard J., Vella A. and Deconihout B. (2009)**
Thermal response of a field emitter subjected to ultra-fast laser illumination. *Journal of Physics D: Applied Physics*, 42, 125502.
- Vurpillot F., Gault B., Geiser B.P. and Larson D.J. (2013)**
Reconstructing atom probe data: A review. *Ultramicroscopy*, 132, 19–30.
- Vurpillot F., Hatzoglou C., Radiguet B., Da Costa G., Delaroche F. and Danoix F. (2019)**
Enhancing element identification by expectation-maximization method in atom probe tomography. *Microscopy and Microanalysis*, 25, 367–377.
- Wallace N.D., Ceguerra A.V., Breen A.J. and Ringer S.P. (2018)**
On the retrieval of crystallographic information from atom probe microscopy data via signal mapping from the detector coordinate space. *Ultramicroscopy*, 189, 65–75.
- Watanabe T. (1985)**
Structural effects on grain boundary segregation, hardening and fracture. *Journal de Physique Colloques*, 46, C4-555–C4-566.
- Watanabe T., Murakami T. and Karashima S. (1978)**
Misorientation dependence of grain-boundary segregation. *Scripta Metallurgica*, 12, 361–365.
- Waugh A.R., Boyes E.D. and Southon M.J. (1976)**
Investigations of field evaporation with a field-desorption microscope. *Surface Science*, 61, 109–142.
- Waugh A., Payne S., Worrall G. and Smith G. (1984)**
In situ ion milling of field ion specimens using a liquid metal ion source. *Le Journal de Physique Colloques*, 45, C9-207–C9-209.
- Weber J., Barthel J., Brandt F., Klinkenberg M., Breuer U., Kruth M. and Bosbach D. (2016)**
Nano-structural features of barite crystals observed by electron microscopy and atom probe tomography. *Chemical Geology*, 424, 51–59.
- White L.F., Darling J.R., Moser D.E., Reinhard D.A., Prosa T.J., Bullen D., Olson D., Larson D.J., Lawrence D. and Martin I. (2017)**
Atomic-scale age resolution of planetary events. *Nature Communications*, 8, 1–6.
- White L.F., Darling J.R., Moser D.E., Cayron C., Barker I., Dunlop J. and Tait K.T. (2018a)**
Baddeleyite as a widespread and sensitive indicator of meteorite bombardment in planetary crusts. *Geology*, 46, 719–722.
- White L.F., Darling J.R., Moser D.E., Reinhard D.A., Dunlop Jr., Larson D.J., Lawrence D. and Martin I. (2018b)**
Complex nanostructures in shocked, annealed, and metamorphosed baddeleyite defined by atom probe tomography. In: Moser D.E., Corfu F., Darling J.R., Reddy S.M. and Tait K. (eds), *Microstructural geochronology: Planetary records down to atom scale*. Wiley (Hoboken, NJ, USA), 351–367.
- White L.F., Kizovski T.V., Tait K.T., Langelier B., Gordon L.M., Harlov D. and Norberg N. (2018c)**
Nanoscale chemical characterisation of phase separation, solid state transformation, and recrystallization in feldspar and maskelynite using atom probe tomography. *Contributions to Mineralogy and Petrology*, 173, 283.
- White L.F., Moser D.E., Tait K.T., Langlier B., Barker I. and Darling J.R. (2019)**
Crystallization and impact history of a meteoritic sample of early lunar crust (NWA 3163) refined by atom probe geochronology. *Geoscience Frontiers*, 10, 1841–1848.
- Whitehouse M.J., Kusiak M.A., Wirth R. and Kumar G.R.R. (2017)**
Metallic Pb nanospheres in ultra-high temperature metamorphosed zircon from southern India. *Mineralogy and Petrology*, 46, 1–8.
- Wu J. and Buseck P.R. (2013)**
Carbon storage at defect sites in mantle mineral analogues. *Nature Geoscience*, 6, 875–878.
- Wu Y.-F., Fougerousse D., Evans K., Reddy S.M., Saxe D.W., Guagliardo P. and Li J.-W. (2019)**
Gold, arsenic, and copper zoning in pyrite: A record of fluid chemistry and growth kinetics. *Geology*, 47, 641–644.
- Xiang Y., Chity V., Liddicoat P., Felfer P., Caimey J., Ringer S. and Kruse N. (2013)**
Long-chain terminal alcohols through catalytic CO hydrogenation. *Journal of the American Chemical Society*, 135, 7114–7117.
- Yang Q., Joyce D.E., Saranu S., Hughes G.M., Varambhia A., Moody M.P. and Bagot P.A.J. (2016)**
A combined approach for deposition and characterization of atomically engineered catalyst nanoparticles. *Catalysis, Structure and Reactivity*, 1, 125–131.
- Zelenty J., Dahl A., Hyde J., Smith G. and Moody M.P. (2017)**
Detecting clusters in atom probe data with Gaussian mixture models. *Microscopy and Microanalysis*, 23, 269–278.
- Zhang F. and Wright K. (2012)**
Lithium defects and diffusivity in forsterite. *Geochimica et Cosmochimica Acta*, 91, 32–39.



references

- Zhang F, Walker A.M., Wright K. and Gale J.D. (2010)**
Defects and dislocations in MgO: Atomic scale models of impurity segregation and fast pipe diffusion. *Journal of Materials Chemistry*, 20, 10445.

Supporting information

The following supporting information may be found in the online version of this article:

Appendix S1. List of published APT studies in the geoscience field.

This material is available from <http://onlinelibrary.wiley.com/doi/10.1111/ggr.12313/abstract> (this link will take you to the article abstract).